Max-Planck-Institut
für Meteorologie

REPORT No. 146

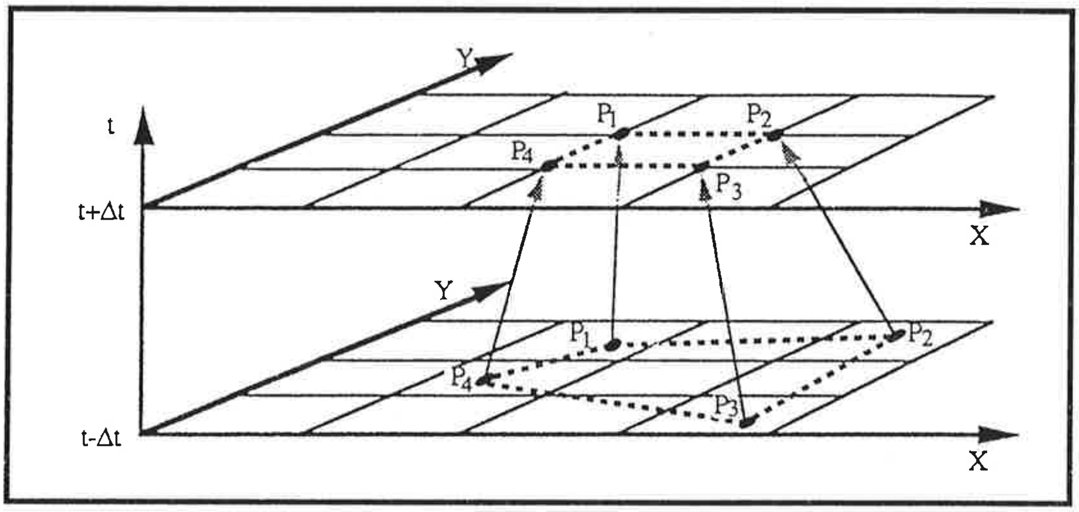

MPI WORKSHOP
ON
SEMI-LAGRANGIAN METHODS
Hamburg, 8 - 9 October 1992

edited by
BENNERT MACHENHAUER

HAMBURG, September 1994

AUTHORS:

Bennert Machenhauer	Max-Planck-Institut für Meteorologie Hamburg, Germany

MAX-PLANCK-INSTITUT
FÜR METEOROLOGIE
BUNDESSTRASSE 55
D-20146 HAMBURG
F.R. GERMANY

Tel.:	+49 - (0)40 - 411 73 - 0
Telefax:	+49 - (0)40 - 411 73 - 298
E-Mail:	<name>@dkrz.d400.de

ISSN 0937 – 1060

MPI Workshop
on
Semi-Lagrangian Methods

Hamburg, 8-9 October 1992

edited by

Bennert Machenhauer

Hamburg, September 1994

CONTENTS

Introduction 1

List of Participants 4

Conclusions 5

Papers presented

Harold Ritchie, CMC:
Examples of Semi-Lagrangian Advection Alternatives. 7

Clive Temperton, ECMWF:
Recent and future developments of the ECMWF semi-Lagrangian scheme. 35

David L. Williamson, NCAR:
A Semi-Lagrangian Version of the NCAR CCM2 and Examples of Climate Simulations. 51

Bennert Machenhauer, MPI:
A Note on a Mass-, Energy- and Entrophy Conserving Semi-Lagrangian and Explicit Integration Scheme for the Primitive Meteorological Equations. 73

Introduction

The accuracy of atmospheric numerical models has steadily improved with increases in resolution. This has been the case for the relatively high resolution weather prediction modes as well as for the lower resolution climate models. Consequently any new technique that offers increased efficiency of numerical models without loss of accuracy is of considerable interest for both applications. One such technique is a semi-Lagrangian treatment of advection which offers a potential economical advantage by eleminating the normal advective Courant-Friedrichs-Lewy (CLF) time-step restriction. In principle, the time-step in a semi-Lagrangian model can be chosen based on accuracy considerations.

The semi-Lagrangian advection offers additional advantages beyond the longer time-step. It gives minimal phase error, minimizes computational dispersion, can handle sharp discontinues and furthermore desirable properties such as monotonicity or, more generally, shape preservation may easily be incorporated.

A disadvantage is that the smallest scales resolved may be damped more by semi-Lagrangian methods than by some Eulerian methods.However, this seems not to be a serious issue as it can be counteracted by a reduction or elimination of horizontal diffusion. A more serious disadvantage of semi-Lagrangian schemes to date is that they do not formally conserve integral invariants as total mass and total energy. This may not be a problem in weather forecasting applications. For long simulations in climate applications, however, lack of conservation could have serious consequences. The total mass, for instance, could drift enough in long simulations that the mean surface pressure error might begin to seriously affect the simulation. Conservation of total mass may be obtained by a "mass-fixer" which after each time-step set the area avaraged surface pressure equal to the initial value. This prevents a drift of the mean surface pressure, but the loss or gain of total mass is compensated by adding or removing abitrarily the same amount of mass everywhere instead of at the correct geographical positions. How serious the non-conservation of mass may affect a long term integration in unclear. However, it might be caused by errors which are locally large and systematic in specific types of pressure patterns, in which case it might significanctly affect the internal dynamics of a model even when a drift in the mean pressure is prevented by a mass-fixer.

Currently semi-Lagrangian advection approximations are beeing incorporated into many numerical weather prediction models and at two centres, the European Centre for Medium-Range Weather Forecasts (ECMWF) and the Canadian Meteorological Center (CMC), semi-

Lagrangian global spectral models have already been used operationally for some time. The increased efficiency of semi-Lagrangian models has allowed both centers to increase their operational spatial resolution. At ECMWF, for instance, their global spectral model is now run at a T213/L31 resolution. Here the semi-Lagrangian model version is permitting a 15 minute time-step which is a fivefold increase in time-step relative to that required in an Eulerian model with similar resolution. A resulting efficiency improvement of about a factor 4 has been obtained.

These developments in numerical weather prediction had been followed with interest here at MPI. The aim of the present workshop was to get up-to-date informations on the state of development and to initiate investigations of the fisability of introducing the semi-Lagrangian advection also in the global spectral model, ECHAM, used for climate simulations at MPI.

It had been decided already that, for the sake of incrased accuracy, the shape preserving semi-Lagrangian advection, developed at the National Center for Atmospheric Research (NCAR) by Williamson and Rasch, should be implemented for the advection of water and chemical constituents in a new version of the model, ECHAM4, which were currently under development. The question was whether a complete change including also the incorporation of semi-Lagrangian advection for the remaining variables should be made in a future version of the climate model. It was realized that the gain in efficiency from incorporating semi-Lagrangian advections in a low resolution climate model may be less dramatic due to restrictions of the time-steps over which physical parameterizations may be used without loss of accuracy.

To discuss these issues a representative from each of the three centres CMC, ECMWF and NCAR was invited to participate in the workshop.

The three scientists invited were

Harold Ritchie, CMC,
Clive Temperton, ECMWF, and
Dave Williamson, NCAR.

They had been the key persons in the development of the semi-Lagrangian model versions at there respective centres. Beside beeing the central person in the development of the semi-Lagrangian model at CMC Harold Ritchie had contributed actively also to the development of the ECMWF model.

The ECMWF and CMC models are rather similar in design. The main differences are between these two models and the semi-Lagrangian version of the NCAR Community Climate Model (CCM2). As mentioned above one area of concern with the semi-Lagrangian approach is the lake of a priori conservation of integral invariants. In the NCAR model special case has been taken in retaining a consistency between the terms involved in the conversion between kinetic and potential energy as well as a consistency between the descrete continuity equation and the vertical motions influencing the energy conversion. The NCAR models were developed for use in climate simulations and included "fixers" to guarantee conservation of the mass of dry air and, in the absence of sources and sinks, the mass of water vapor.

Papers were presented by the three invited guests and by Bennert Machenhauser, MPI. In the latter paper an alternative semi-Lagrangian model design were layed out for discussion. The basic idea behind the design was an application of a so called cell-integrated semi-Lagrangian approach to Lagrangian forms derived from the complete set of primitive equations. The model design presented would ensure exact conservation of mass, total energy, enstrophy and angular momentum.

List of Participants

Klaus Arpe, MPI

Lennart Bengtsson, MPI

Bennert Machenhauer, MPI

Harold Ritchie, CMC, Canadian Meteorological Center,
Recherche en Prevision Numerique, Douval, Québec, Canada

Ulrich Schlese, DKRZ

Clive Temperton, ECMWF, European Centre for Medium Range Forecasts,
Reading, Berkshire, U.K.

David Williamson, NCAR, National Center for Atmospheric Research,
Boulder, Colorado, U.S.A.

and observers from

MPI, Max-Planck-Institut für Meteorologie,
Hamburg, Germany

DKRZ, Deutsches Klimarechenzentrum, Hamburg, Germany.

Conclusions of discussions

Following the presentations on the first day of the workshop a round-table discussion were held on the second day with the participants (explecitely) mentioned in the list above.

It was concluded that the operational semi-Lagrangian models developed at CMC and ECMWF seemed to work satisfactory in weather forecast mode. Control Eulerian forecasts with a short time-step and semi-Lagrangian forecasts with relatively long time-steps had been found to give almost equivalent accuracy. So far they had not been tested in climate mode, i.e. with lower resolution in very long term integrations. The semi-Lagrangian version of the CCM2 had been developed at NCAR for applications in climate research, but so far it had been tested only in relatively short term integrations.

It was decided to initiate coordinated experiments with the semi-Lagrangian schemes currently available at the three centres in order to test the suitability for the use in climate simulations. Each center should perform two five year integrations, an Eulerian control integration and a semi-Lagrangian integration, with similar resolution and sea-surface temperature (SST). CMC would run its model at resolution T63/L20, NCAR would run the CCM2 at T42/L18 and ECMWF would run at T63/L19. Annual-cycle climatological SST's and sea-ice distributions (AMIP) should be used and mass conservation would be (approximately) enforced by fixing the horizontal mean of ln p_S (p_S beeing the surface pressure). The results obtained from the ECMWF experiments should be analysed at MPI.

The cell-integrated semi-Lagrangian scheme proposed by Machenhauer were found intriguing and it was recommended that this work should be continued as intended with tests of the scheme at first in a shallow water model. A coorporation might be established with Rene Laprice and his student André Plante at the University of Quebec in Montreal who independently had developed and tested cell-integrated semi-Lagrangian schemes for horizontal advection of a passive scalar.

Examples of Semi-Lagrangian Advection Alternatives

Harold Ritchie

Recherche en Prévision Numérique
Atmospheric Environment Service
Dorval, Québec, Canada H9P 1J3

Introduction

By way of introduction and to set the stage for the following presentattions, here we start by reviewing the steps that we have followed in applying the semi-Lagrangian advection scheme to spectral models. In particular, examples of some advection alternatives will be highlighted, and we will conclude with a discussion of a cell-integrated transport scheme which is being examined by Laprise and Plante at L'Université du Québec à Montréal for possible use in climate models, and which may be relevant for the conserving semi-Lagrangian formulations being developed here at the Max Planck Institute.

The efficiency advantage of the semi-Lagrangian semi-implicit scheme was demonstrated a decade ago by André Robert (1981, 1982) in the context of grid point models of the shallow water equations. Since that time considerable work has been done in applying the method in baroclinic models, and several centres are now using it in operational weather forecasting models. The first step for spectral models was to examine the semi-Lagrangian treatment of advection on the gaussian calculation grid used in such models (Ritchie, 1987), which addressed the geometric and linear stability questions. The next step was to combine the semi-Lagrangian approach with the semi-implicit scheme to get a stable treatment of both Rossby and gravity waves in a spectral model of the shallow water equations (Ritchie, 1988). The extension to baroclinic models was then examined through an application to a multilevel spectral primitive equations model, where several issues related to vertical discretizations were addressed (Ritchie, 1991). Following further optimization, semi-Lagrangian semi-implicit spectral models have now been implemented at the Canadian Meteorological Centre and ECMWF. Work is currently in progress to use lower resolution versions of these models in dynamic extended range forecasting and in climate simulations.

Semi-Lagrangian AdvectioEn on a Gaussian Grid

Here we review the characteristics of two types of semi-Lagrangian advection that were applied to this problem of solid body rotation (Ritchie, 1987) . In this and subsequent sections the figure numbering is not necessarily consecutive, as the numbers refer to the figures as published in the corresponding articles. A schematic diagram showing the experiment configuration is shown in Fig. 1. We consider rotation with constant angular velocity about an axis passing through the center of the earth and a point P' on the earth's surface. To facilitate the interpretation of the results we introduce a stereographic plane which is tangent to the earth's surface at P'. Since the motion corresponds to solid body rotation about P', when viewed in this plane the advected field should simply rotate around P' without any distortion. NP is the projection in the stereographic plane of the north pole of the gaussian grid, EQ is the projection of the equatorial point E, and the X-axis of the stereographic (X,Y) plane is also indicated. The analytic solution is centred over EQ initially and its center passes over NP after half a revolution. The initial field is chosen to be a "Gaussian hill" function which has a peak value of 100 units at its center and decays towards zero with a gaussian profile with a length scale of L, which is approximately the diameter of the contour whose value is 10 percent of the peak value. The angular velocity is chosen to correspond to one rotation in 20 days, which gives a typical synoptic scale advecting velocity of 16.4 m/s through points E and N shown in Fig.1. A stereographic map of an analytic solution with L=2500 km after one rotation is shown in Fig.5.

An Eulerian spectral model was used to solve the solid body rotation problem. The spectral representation used triangular truncation with a maximum wavenumber N = 42, requiring 128 gridpoints in the longitudinal direction and 64 gridpoints in the latitudinal direction to avoid quadratic aliasing. The Courant-Friedrichs-Lewy (CFL) stability limit for this configuration restricts the time step to 1.82 h. For convenience, the time step for the Eulerian spectral model integrations was chosen to be 1.5 h. The Eulerian model numerical solution corresponding to Fig.5 is shown in Fig.6 and the error (analytic-numerical) field is shown in Fig.7. We note that the dispersion associated with Eulerian model time truncation error has caused a noticeable distortion in the numerical solution, resulting in a downstream wake in the error pattern. Here the maximum absolute error value is in excess of 25 units.

Semi-Lagrangian schemes using high-order interpolation have much smaller dispersion errors than Eulerian schemes. This can be illustrated by an interpolating semi-

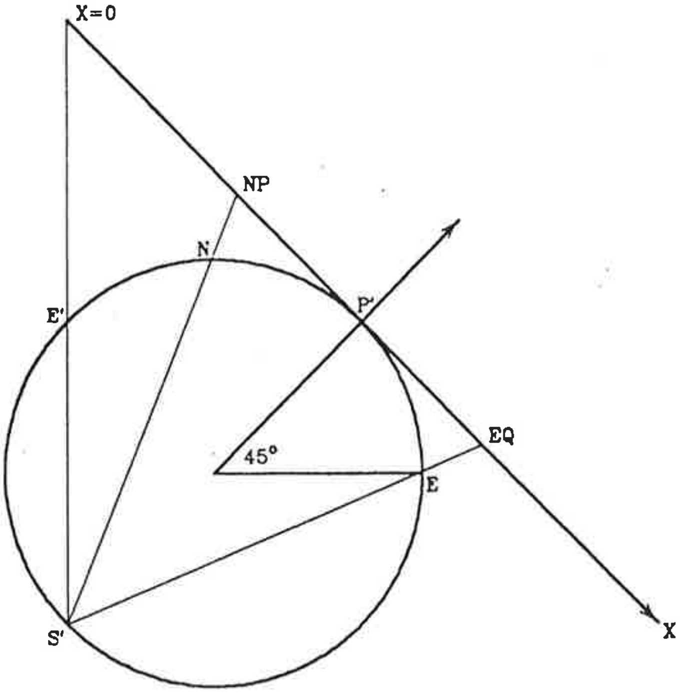

FIG. 1. Schematic diagram showing the experiment configuration. Labelled points are described in the text.

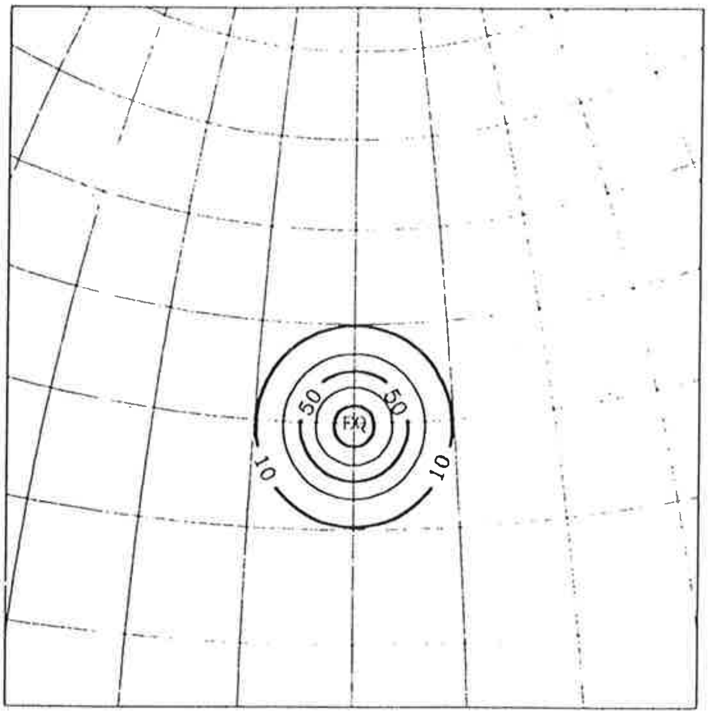

FIG. 5. Analytic solution at 480 h. L = 2500 km. Latitude and longitude lines are drawn every 10 deg. Contour interval 20 units.

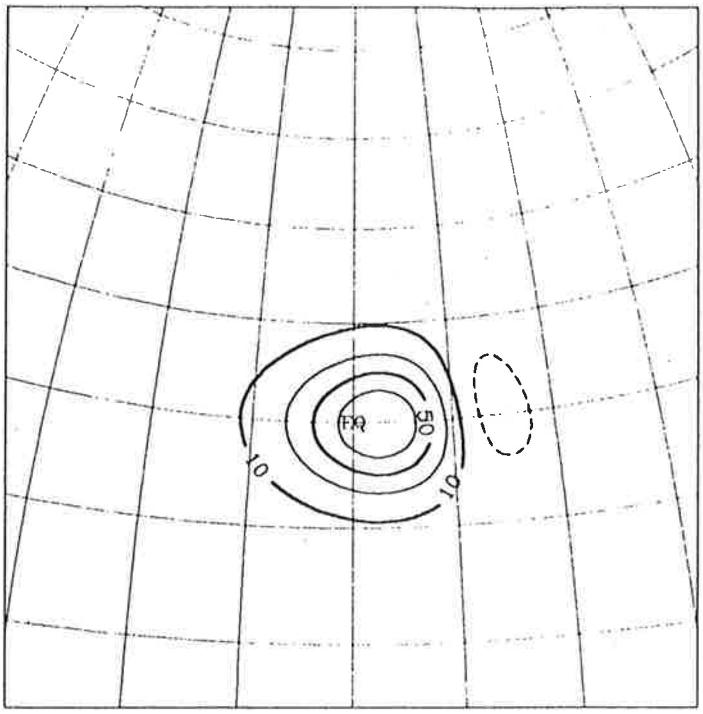

FIG. 6. Numerical solution at 480 h produced by the Eulerian spectral model. L = 2500 km. Contour interval 20 units.

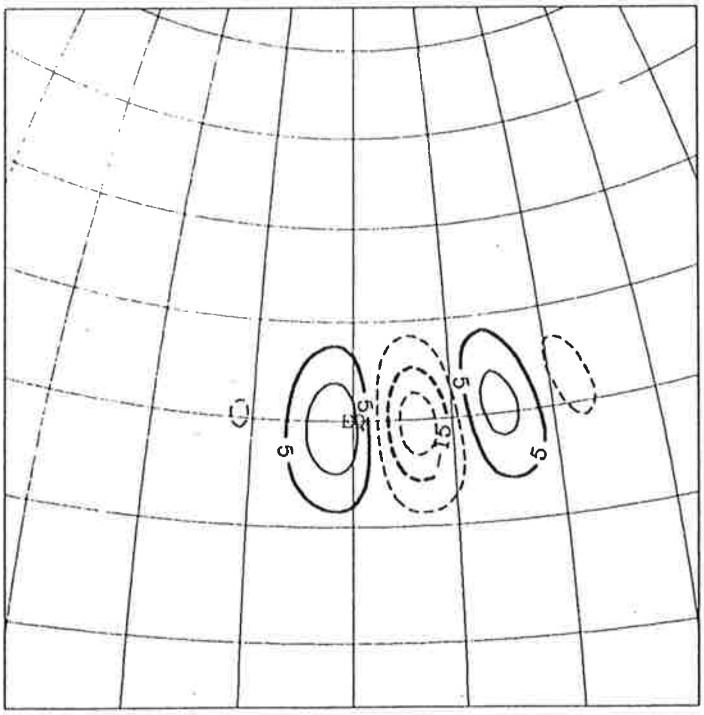

FIG. 7. Error in Eulerian spectral solution at 480 h. L = 2500 km. Dashed contours indicate negative values. Contour interval 10 units.

Lagrangian model solution of the solid body rotation problem. The model grid and parameters were the same as those used for the Eulerian spectral model except that the time step was six hours, which is four times that used by the Eulerian spectral model and violates the CFL stability limit by a factor of roughly 3.3. The numerical solution is shown in Fig.9, and the error field is presented in Fig.10. As indicated by the concentric shape of the error pattern, the semi-Lagrangian scheme gives a much more accurate treatment of the phase speed of the solution. Also, the maximum value of the error is about 16 units, which is much less than for the corresponding Eulerian field (Fig.7). However, the error pattern also shows clear evidence of damping due to the spreading out of the field as a result of interpolation errors.

There is another version of the semi-Lagrangian scheme which does not require interpolation in order to pick off the upstream values of the field being advected. This scheme does not suffer from significant damping errors, but retains the attractive stability property. The numerical solution produced using a model with this scheme is shown in Fig.11 and the error field in Fig.12. The model grid and truncation were the same as those used for the the Eulerian spectral model, and the time step was 6 hours as in the interpolating semi-Lagrangian model. The maximum absolute error value in Fig.12 is just over 2.5 units, which is much less than the corresponding error fields (Figs.7 and 10) for the other two models. Although the 10 unit contour in Fig.11 indicates some slight distortion due to the phase speed error, comparing to Fig.6 and Fig.7 shows that the phase error for this length scale is much less than with the Eulerian model. Also, in Fig.12 there is no evidence of the concentric error pattern associated with damping as in the corresponding interpolating semi-Lagrangian integration (Fig.10).

In order to provide a more systematic and quantitative intercomparison, all three models were run with initial fields having length scales L = 10000 km, 5000 km, and 2500 km. The grid and model parameters were the same as already outlined. The errors at various times were calculated by by comparing with the analytic solution and, as a measure of the accuracy in each case, the integral of the absolute value of these errors was expressed as a percent of the integral of the analytic solution. Table 1 contains the percentage errors for each case at 120, 240, 360 and 480 h, which corresponds to one full rotation of the analytic solution. It is seen that all three models perform very well for L = 10000 km, with the noninterpolating semi-Lagrangian version being slightly poorer than the other two. For this length scale, the field is well resolved by all models, so there is very little dispersion or damping error. As the length scale is reduced, there is a marked deterioration in the

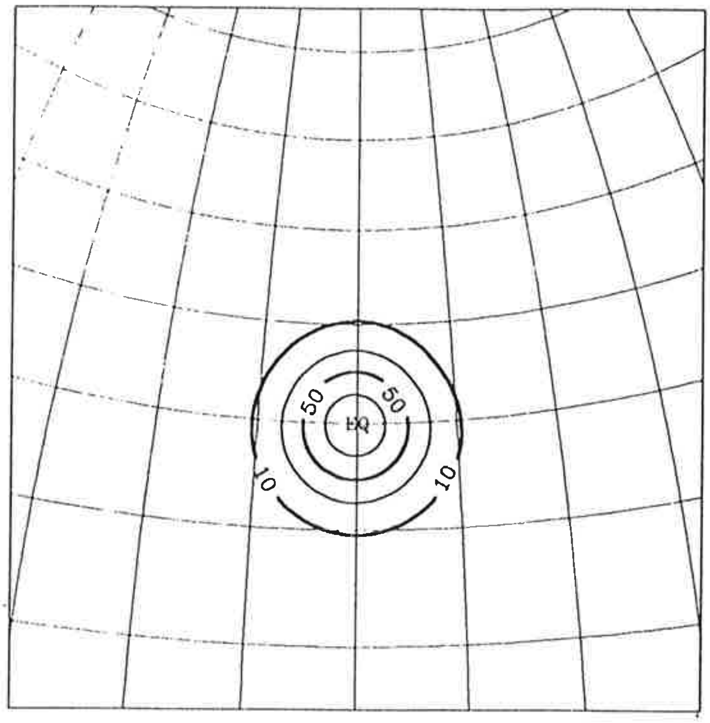

FIG. 9. As in Fig. 6 except for interpolating semi-Lagrangian model.

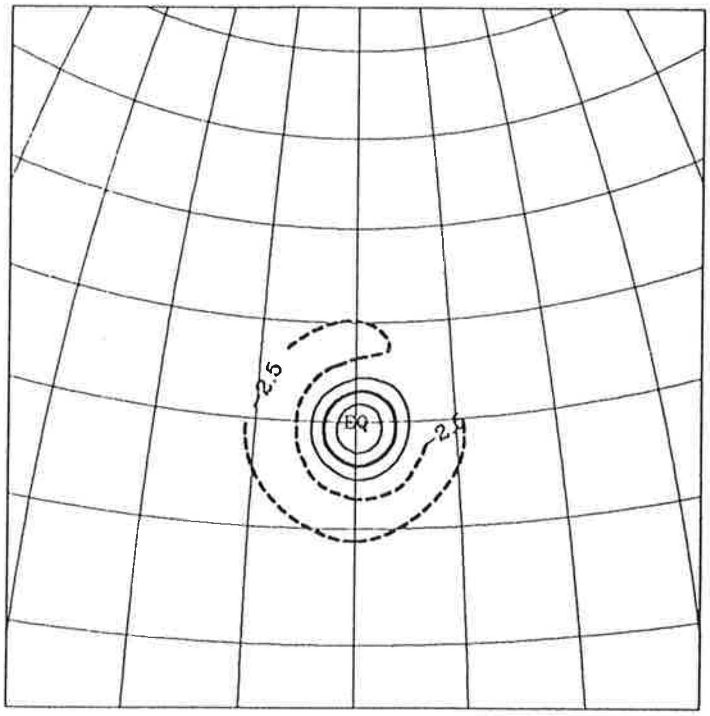

FIG. 10. As in Fig. 7 except for interpolating semi-Lagrangian model and contour interval 5 units.

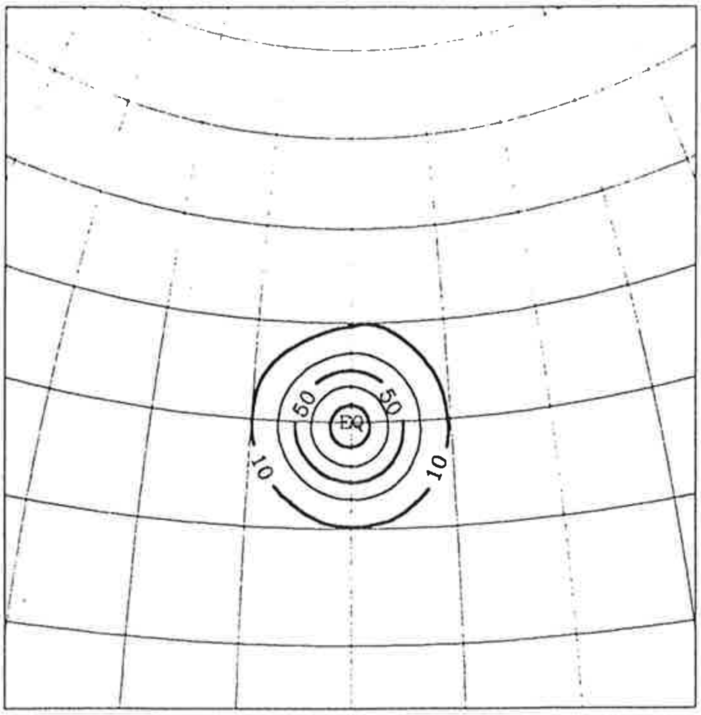

FIG. 11. As in Fig. 6 except for noninterpolating semi-Lagrangian model.

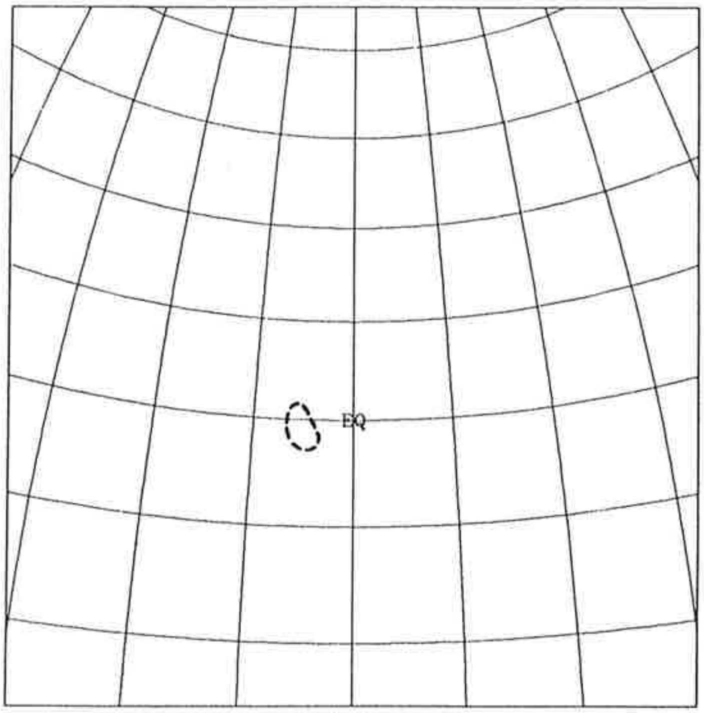

FIG. 12. As in Fig. 7 except for noninterpolating semi-Lagrangian model and contour interval 5 units.

performance of the Eulerian model due to the increased dispersion as discussed earlier. The performance of the interpolating semi-Lagrangian model deteriorates less, altough the damping becomes noticeable for the short scales. At short scales, the noninterpolating semi-Lagrangian model gives the best overall performance because it has less dispersion than the Eulerian model and less damping than the interpolating semi-Lagrangian model.

This demonstrates that the semi-Lagrangian scheme can be stably and accurately applied to treat advection on the Gaussian grid with time steps that far exceed the CFL limit for the Eulerian spectral model. The interpolating and the noninterpolating versions both compare favourably with the Eulerian one in terms of accuracy, and the noninterpolating scheme seems to have some advantage for the treatment of short scales.

TABLE 1. Error results for the model intercomparison as explained in the text. EUL denotes the Eulerian spectral model (time step 1.5 h), ILS denotes the interpolating semi-Lagrangian model (time step 6 h), and NISL denotes the noninterpolating semi-Langrangian model (time step 6 h). The errors are expressed in percent.

		Prognosis (h)			
L (km)	Model	120	240	360	480
10000	EUL	0.22	0.34	0.55	0.68
10000	ISL	0.18	0.35	0.52	0.70
10000	NISL	0.31	0.55	0.77	1.01
5000	EUL	1.55	2.73	4.24	5.48
5000	ISL	0.57	0.96	1.36	1.90
5000	NISL	0.62	1.05	1.31	1.67
2500	EUL	15.2	26.4	38.0	48.2
2500	ISL	6.31	8.02	10.6	15.2
2500	NISL	4.71	6.44	8.08	9.72

An Energy Conservation Example

An example of the energy conservation properties of the semi-implicit semi-Lagrangian schemes is found in the application of the semi-Lagrangian method to a spectral model of the shallow water equations. In order to examine this question, the interpolating and noninterpolating semi-Lagrangian models were run out to 20 days with a 60 min time step at resolutions of T63 (triangular 63-wave truncation) and T126. The interpolating model had no filters, while the noninterpolating one had a Robert time filter with a weak coefficient of 0.04 at T63 and 0.02 at T126 (using the definition as given in the analysis by Asselin 1972). The evolutions of the potential energy per unit mass (P), the kinetic energy per unit mass (K), and the total energy (T = P + K) are presented in Fig.10 for the T63 runs and Fig.11 for the T126 runs. The energies for each run are expressed as a percentage of the initial total energy for the run. Here the solid curves are for the noninterpolating model and the long dashed curves are for the interpolating one. As an indication of the energy conservation behaviour that is considered to be acceptable in typical medium range forecasts, the Eulerian model was run at a resolution of T106 with a time step of 12 min, and a fourth order spectral diffusion with a coefficient of 10**15 m**4/s was applied to the vorticity, divergence, and perturbation geopotential. The evolutions of P, K and T for this model are given by the short dashed curves in Figs. 10 and 11. At all resolutions, all models have very similar evolutions of potential energy and the models appear to be evolving towards a state of equipartition of kinetic and potential energy. For the T106 Eulerian run, the loss in total energy after 20 days is about 3%. At the lower resolution (T63, Fig.10) the decay of kinetic energy for the interpolating model is a little excessive, resulting in a loss of about 5% in total energy, while the noninterpolating model conserves total energy to within about 1%. At the higher resolution (T126, Fig.11), the effect of damping in the interpolating scheme is much smaller and both semi-Lagrangian models conserve total energy to within about 1%. Note that the two seim-Lagrangian models are almost indistinguishable (the solid and long dashed curves almost superimpose) in this figure, and both give better energy conservation than the T106 Eulerian model (short dashed curve). All these runs have good mass conservation characteristics, conserving mean perturbation geopotential to within half a percent.

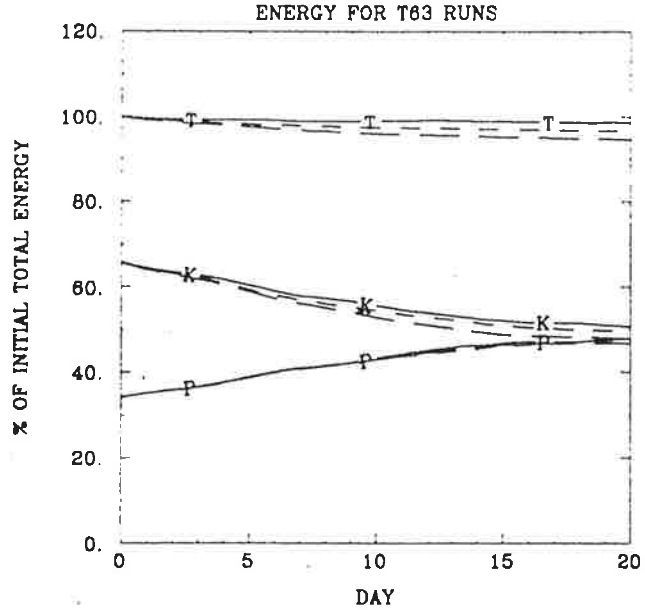

FIG. 10. Evolution of potential (*P*), kinetic (*K*), and total (*T*) energy in 20 day T63 integrations as discussed in text. Solid curves are for the noninterpolating semi-Lagrangian model, and long dashed curves are for the interpolating one. Short dashed curves give evolution for T106 Eulerian model with diffusion and are included to indicate behavior in typical medium range forecasts. Energies are expressed as a percentage of the initial total energy for the run.

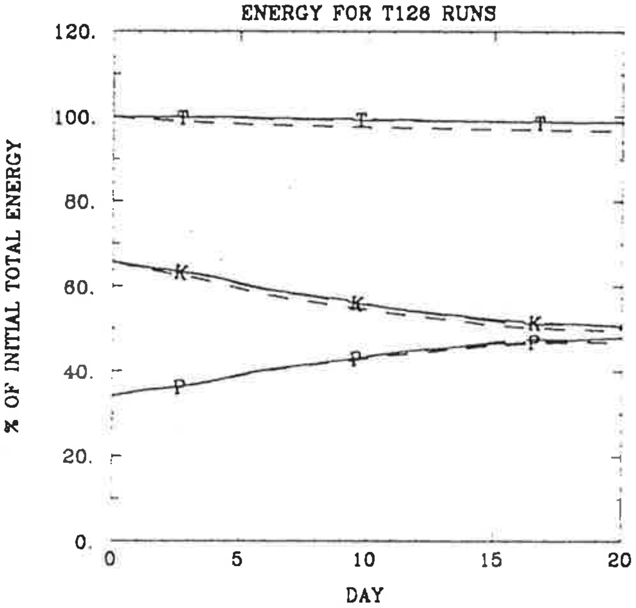

FIG. 11. As in Fig. 10 except for T126 integrations.

Example from a Multilevel Spectral Model

These semi-Lagrangian advection alternatives also proved to be relevant in applying the semi-Lagrangian semi-implicit method to a multilevel spectral primitive equations model. This can be illustrated by intercomparison tests that were performed during the course of this work.

The integrations started from a FGGE analysis valid at 12 UTC 12 February 1979. Nonlinear normal mode initialization was used, and in subsequent intercomparisons involving semi-Lagrangian models with large time-steps, it was found that initialization was important for good agreement between models, particularly during the first two days. Hemispheric integrations were performed with a triangular 79-wave truncation and 20 equally spaced sigma levels ranging from 0.05 at the top to 1.0 at the surface. As in Daley et al. (1976), the physical processes included Cressman's (1960) drag formulation in the lowest layer, a moist convective adjustment based on the principles of Manabe et al. (1965), and orographic effects. Vertical momentum diffusion was included in the top layer. A Robert time filter (with a coefficient of 0.1 using the definition given in the analysis by Asselin 1972) and a sixth order horizontal diffusion with a coefficient of 10**26 were applied.

The first step in applying the semi-Lagrangian method to the starting model was to convert it from a vorticity-divergence formulation (QDEUL) to a vector momentum equation formulation (UVEUL). In terms of the horizontal discretization, these two models are algebraically equivalent. However, they differ somewhat in terms of their vertical discretization. The two versions were integrated using a time-step of 12 min which respects the CFL limit. The changes in vertical discretization cause some differences which warraant quantitative evaluation. This is presented in Fig.4, which shows the evolution of the root-mean-square (r.m.s.) differences between the two runs. The results are in metres and are presented for 10 equally spaced pressure levels, varying from 100 mb at the top to 1000 mb at the bottom of the figure, and at 12-hour intervals, from 0 hours at the left to 5 days at the right of the figure. The differences are greatest at the top and descend gradually during the integrations, reaching values of around 10 m at mid-atmospheric levels after 5 days.

The next step was to convert the Eulerian formulation to one that uses the interpolating semi-Lagrangian approach in the horizontal, while retaining the Eulerian treatment of the vertical advection. In order to test the stability and accuracy of this 2DISL model, the time step was increased to 20 min and the 120 hour forecast was performed. The

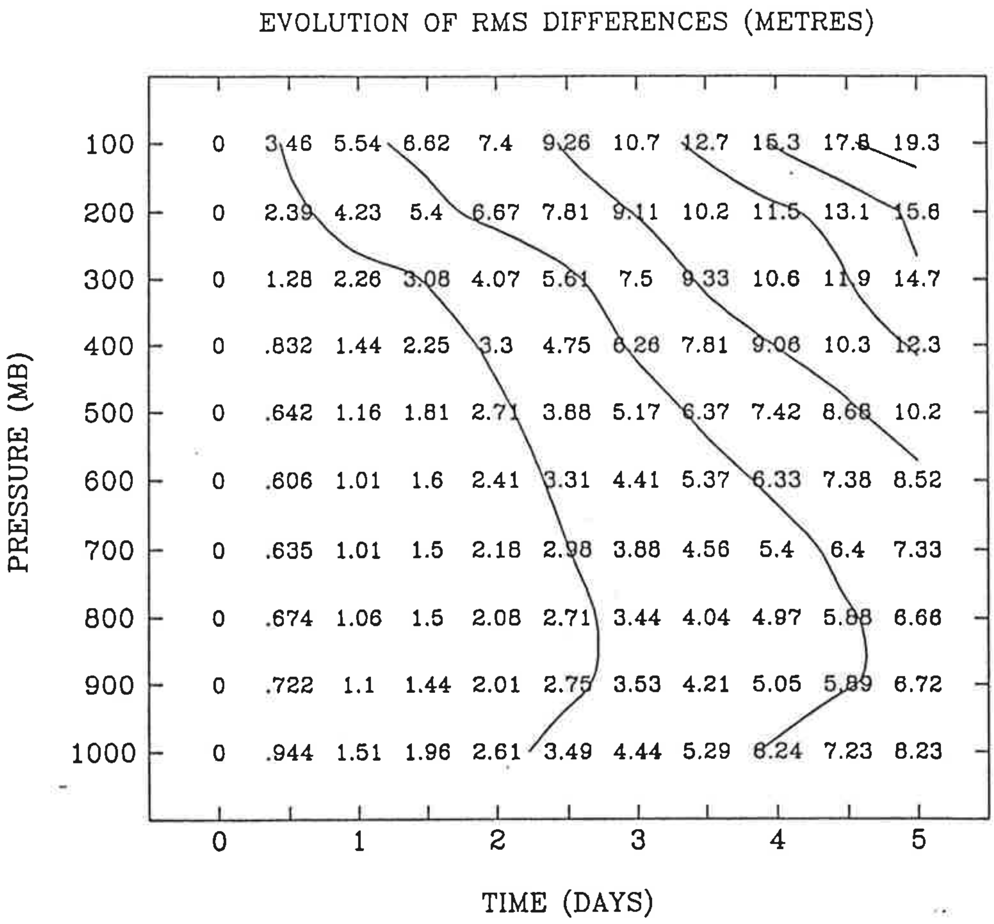

100	0	3.46	5.54	6.62	7.4	9.26	10.7	12.7	15.3	17.8	19.3
200	0	2.39	4.23	5.4	6.67	7.81	9.11	10.2	11.5	13.1	15.6
300	0	1.28	2.26	3.08	4.07	5.61	7.5	9.33	10.6	11.9	14.7
400	0	.832	1.44	2.25	3.3	4.75	6.26	7.81	9.06	10.3	12.3
500	0	.642	1.16	1.81	2.71	3.88	5.17	6.37	7.42	8.68	10.2
600	0	.606	1.01	1.6	2.41	3.31	4.41	5.37	6.33	7.38	8.52
700	0	.635	1.01	1.5	2.18	2.98	3.88	4.56	5.4	6.4	7.33
800	0	.674	1.06	1.5	2.08	2.71	3.44	4.04	4.97	5.88	6.66
900	0	.722	1.1	1.44	2.01	2.75	3.53	4.21	5.05	5.89	6.72
1000	0	.944	1.51	1.96	2.61	3.49	4.44	5.29	6.24	7.23	8.23

Fig. 4 Evolution of rms differences between QDEUL and UVEUL models with 12 min timesteps. Results are in metres and are presented for 10 equally spaced pressure levels, varying from 100 mb at the top to 1000 mb at the bottom of the figure, and at 12 hour intervals, from 0 at the left to 5 days at the right of the figure. Contour interval 3 metres.

evolution of the r.m.s. differences compared with the UVEUL model is shown in Fig.6, with values in the 10-15 m range in the mid atmosphere at 120 hours.

In addition to the CFL limit associated with the horizontal advection, there is also one associated with vertical advection. An attempt was made to increase the time step to 30 min with the 2DISL model, but the integration failed, apparently because of a violation of the vertical CFL criterion. This illustrates the fact that, in order to avoid the vertical CFL limit in models that have high vertical resolution to support a sophisticated boundary layer physical parameterization, it is necessary to use fully 3-dimensional semi-Lagrangian treatments (3DISL). The 120 hour forecast was repeated with the 3DISL scheme using a 20 min time step, and the evolution of the r.m.s. differences with respect to the UVEUL model is presented in Fig.7. The most striking feature here is the large differences that develop in the upper atmosphere early in the integration and then spread downwards, contaminating the whole domain. A closer examination of the model outputs suggested that this is a consequence of excessive vertical smoothing of the fields in the vicinity of the tropopause, where all of the model fields change abruptly in the vertical. In order to clearly identify the problem as originating from the vertical interpolation of the tropopause, a test was performed with a 2-1/2-dimensional semi-Lagrangian (2-1/2DISL) version that uses the 3DISL scheme around the tropopause (i.e. for sigma = 0.20, 0.25, 0.30, 0.35) and the 2DISL scheme elsewhere. The 120 hour forecast was repeated with this 2-1/2DISL model using a 20 min time step, and the evolution of the r.m.s. differences with respect to the 2DISL model with a 20 min time step is shown in Fig.8. The results show that, at least for the Lagrange cubic interpolator and the resolution used here, vertical interpolation of the fields around the tropopause introduces a large difference that spreads upwards and downwards during the integration.

As we saw earlier, one way of avoiding the excessive damping arising from interpolating rapidly varying fields is to modify the semi-Lagrangian scheme to use the noninterpolating approach. It was decided to apply this approach to the vertical advection, while retaining the 2DISL treatment in the horizontal. The resulting method is referred to as noninterpolating semi-Lagrangian in the vertical (NISLV). In order to test the stability and accuracy of this NISLV model, the time step was increased to 40 min and the 120 hour forecast was performed. The evolution of the r.m.s. differences with respect to the UVEUL run in Fig.10 shows that at each level the difference grows roughly linearly in time, and reaches mid-atmospheric levels of about 15 m after 5 days, confirming that the NISLV model produces stable and accurate results with a time step that far exceeds the CFL stability limit

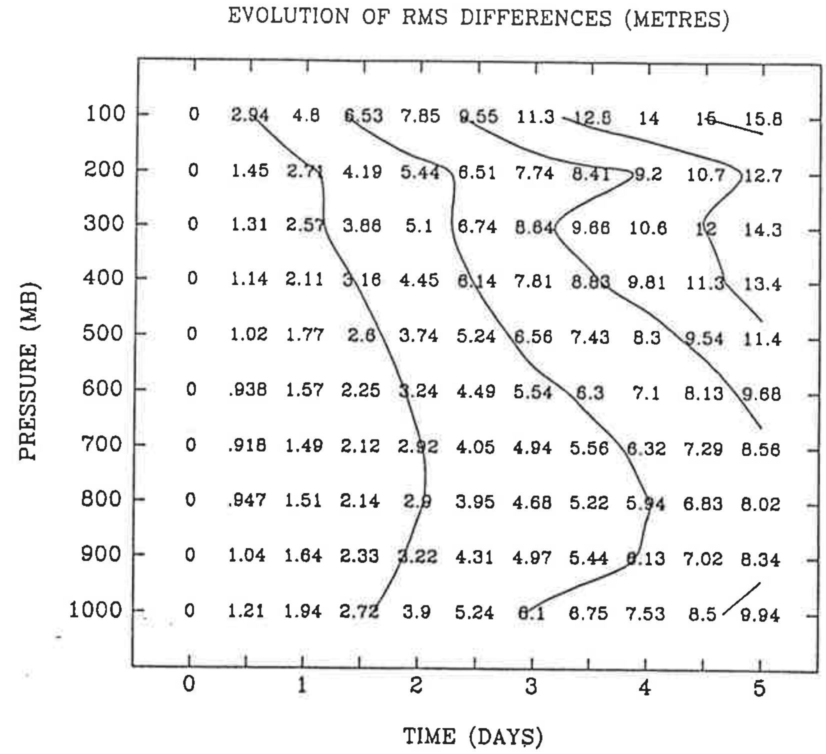
EVOLUTION OF RMS DIFFERENCES (METRES)

Fig. 6 As in Fig. 4 except for 2 DISL model with 20 min timestep versus UVEUL model with 12 min timestep.

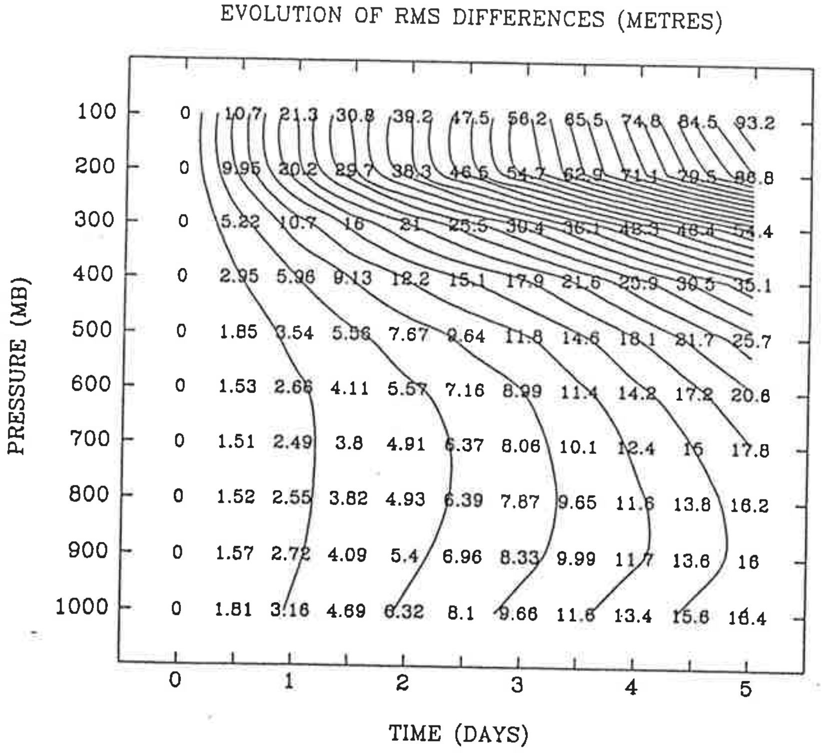
EVOLUTION OF RMS DIFFERENCES (METRES)

Fig. 7 As in Fig. 4 except for 3 DISL model with 20 min timestep versus UVEUL model with 12 min timestep.

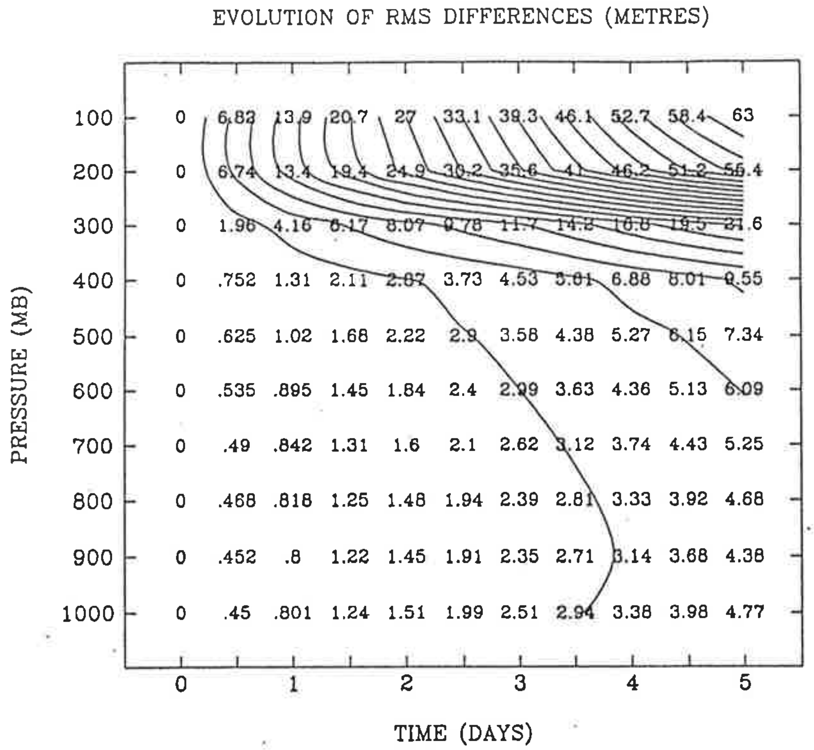

Fig. 8 As in Fig. 4 except for 2 1/2 DISL model with 20 min timestep versus 2 DISL model with 20 min timestep.

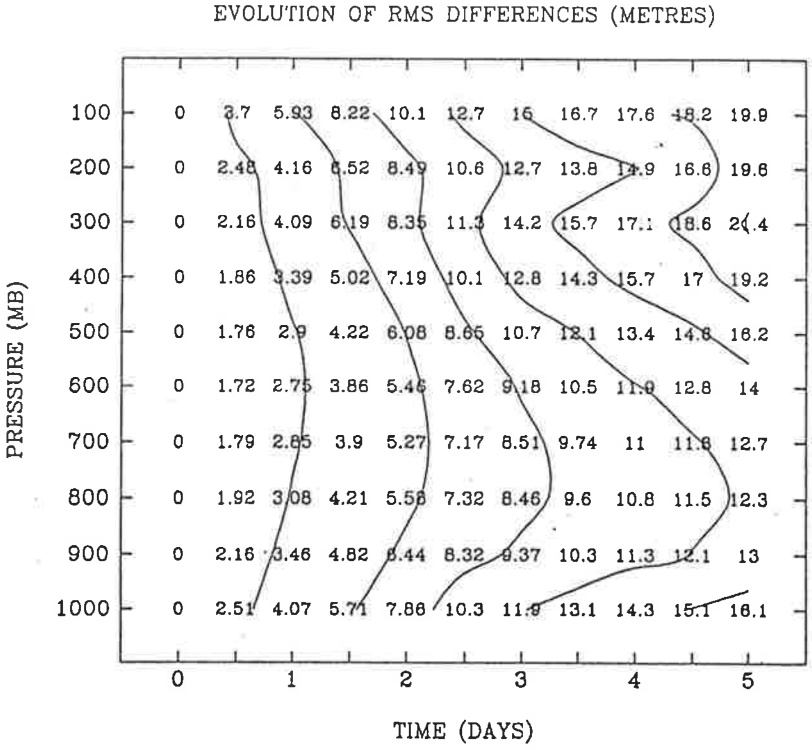

Fig. 10 As in Fig. 4 except for NISLV model with 40 min timestep versus UVEUL model with 12 min timestep.

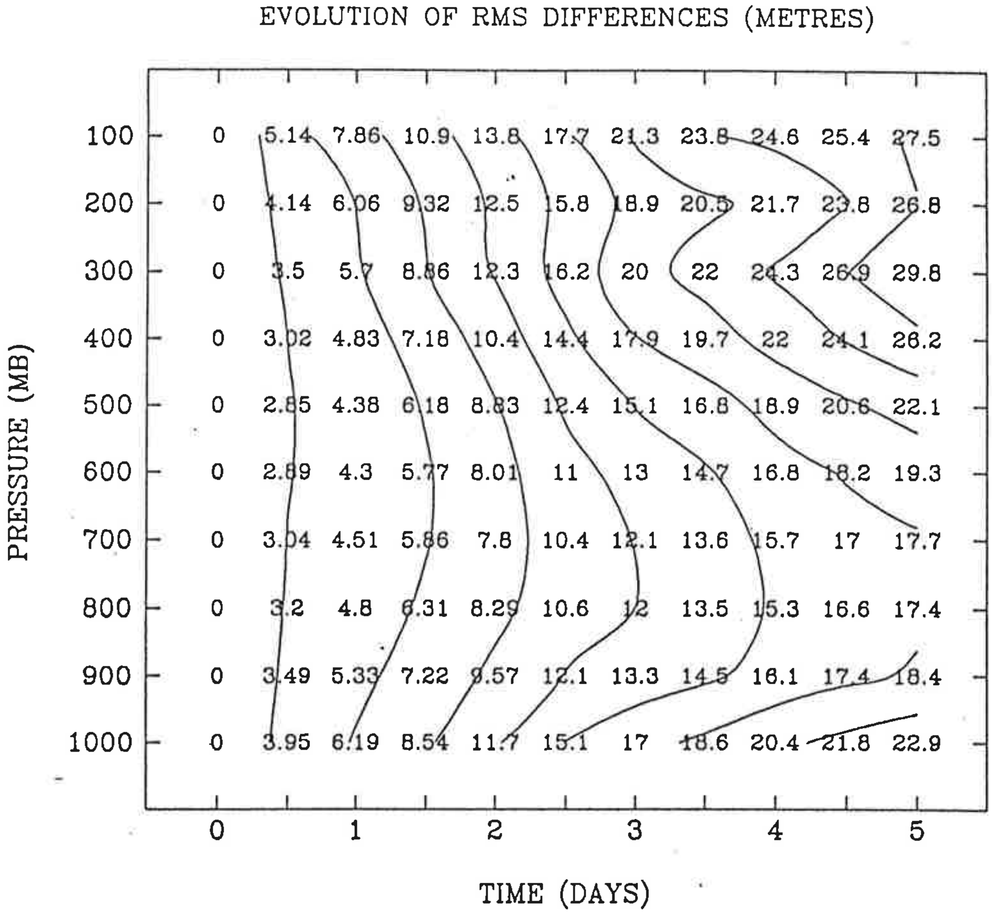

PRESSURE (MB)	0		1		2		3		4		5
100	0	5.14	7.86	10.9	13.8	17.7	21.3	23.8	24.6	25.4	27.5
200	0	4.14	6.06	9.32	12.5	15.8	18.9	20.5	21.7	23.8	26.8
300	0	3.5	5.7	8.86	12.3	16.2	20	22	24.3	26.9	29.8
400	0	3.02	4.83	7.18	10.4	14.4	17.9	19.7	22	24.1	26.2
500	0	2.85	4.38	6.18	8.83	12.4	15.1	16.8	18.9	20.6	22.1
600	0	2.89	4.3	5.77	8.01	11	13	14.7	16.8	18.2	19.3
700	0	3.04	4.51	5.86	7.8	10.4	12.1	13.6	15.7	17	17.7
800	0	3.2	4.8	6.31	8.29	10.6	12	13.5	15.3	16.6	17.4
900	0	3.49	5.33	7.22	9.57	12.1	13.3	14.5	16.1	17.4	18.4
1000	0	3.95	6.19	8.54	11.7	15.1	17	18.6	20.4	21.8	22.9

Fig. 12 As in Fig. 4 except for NISLV model with 60 min timestep versus UVEUL model with 12 min timestep.

for the corresponding Eulerian model. The time step was further increased to 60 min, producing r.m.s. differences with respect to the UVEUL model shown in Fig.12. The model remains stable, but the r.m.s. differences indicate a marginal accuracy at this time step, with mid-atmospheric differences of about 20 m after 5 days.

Transport by Cell-Integrated Semi-Lagrangian Schemes (SLIC)

The advection alternatives that we have considered so far use simple Lagrange cubic interpolators. It has been illustrated that the associated interpolating semi-Lagrangian formulation has some difficulty in handling features with sharp gradients relative to the model resolution. This has impacts for the conservation properties of the models, which are of some concern, especially in the context of long term integrations at relatively low resolution, such as climate simulations. For this reason, tests have been performed with other types of interpolators which suffer less from some of these deficiencies (e.g., Williamson and Rasch, 1989). Work is currently in progress to develop perfectly conserving semi-Lagrangian transport schemes, and to incorporate them in perfectly conserving model formulations. In this section we will consider one such scheme which might be appropriate for the conserving model formulation being examined here at the Max Planck Institute. This material is taken from a masters thesis being prepared by André Plante (1992) under the supervision of René Laprise at l'Université du Québec à Montréal. Their permission and cooperation are gratefully acknowledged.

The conventional starting point for semi-Lagrangian formulations is to express the model equations in Lagrangian or total derivative form. For the cell-integrated semi-Lagrangian scheme the equations are first recast in a conservative or flux form, which is then volume integrated and simplified using Leibniz' and Gauss' theorem to give the total derivative of a volume integral. The surface (henceforth referred to as the "membrane") bounding the volume element moves in time. The position of the membrane is tracked using the classical semi-Lagrangian trajectory calculation algorithm. For the transport equation, perfect conservation is imposed by ensuring that the total mass within the membranes is constant as the volume elements move from one time step to the next. Two versions of the scheme are examined. In the upstream version, the volume element corresponds to a grid volume at forecast time and the membrane is traced backwards over one time step (see Fig.3.2 for a 2-D illustration); in the downstream version the volume element corresponds to a grid volume at the previous time step, and the membrane is projected forward over one time

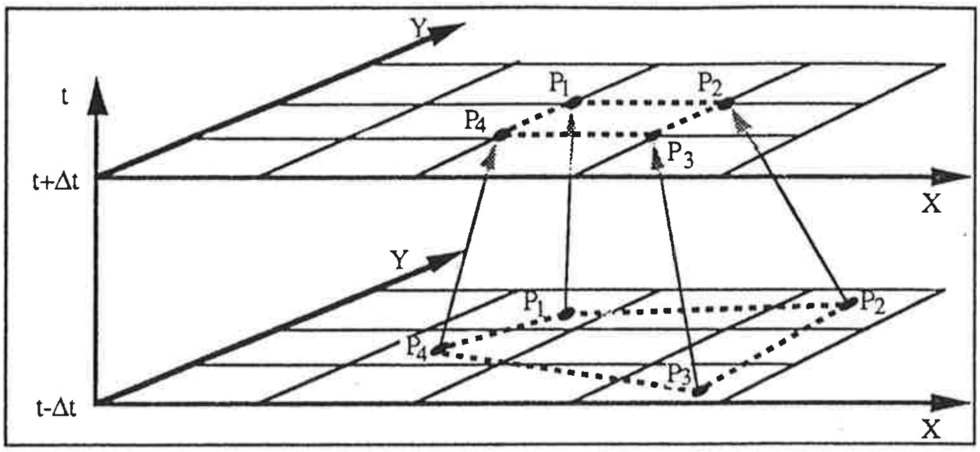

Figure 3.2. Grille de calcul du SLIC amont à t-Δt (grille du bas) et t+Δt (grille du haut). Le rectangle tireté sur la grille du haut représente la tuile i,j. Le tétragone tireté sur la grille du bas illustre la surface d'amont de la tuile i,j sur laquelle il faut intégrer la distribution de la densité pour obtenir la valeur au point de grille i,j à t+Δt. Les points P_1 à P_4 définissent la surface d'amont.

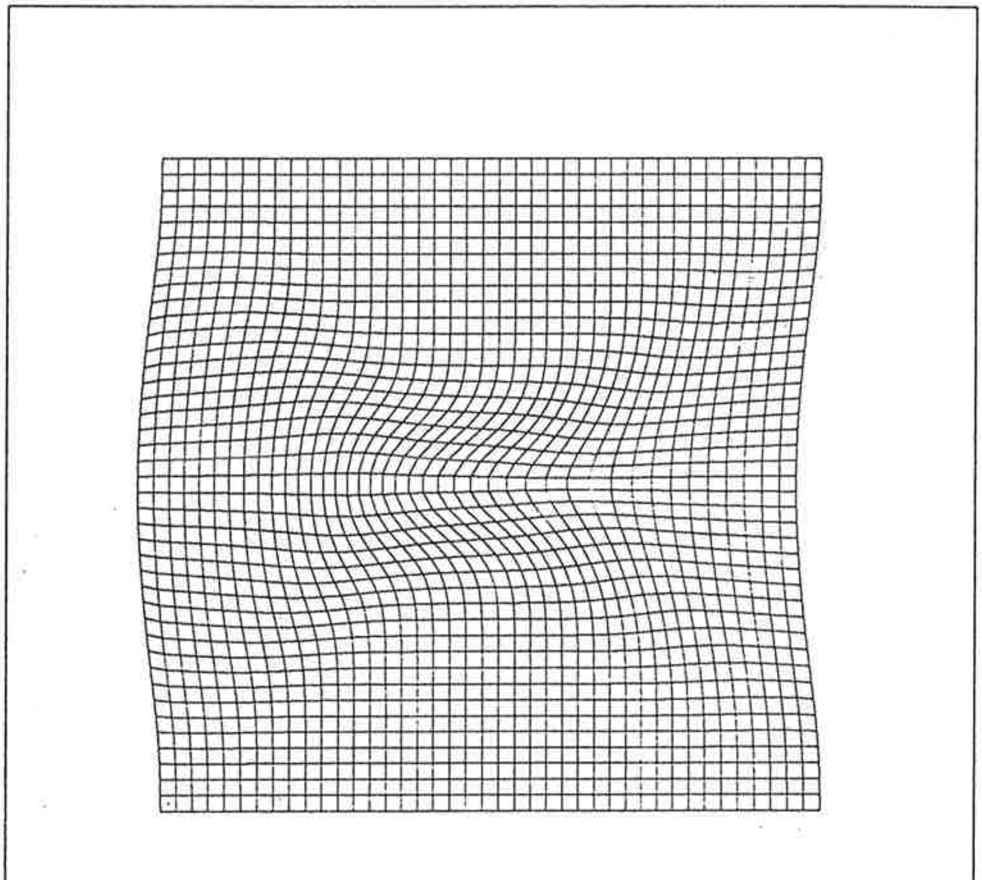

Figure 3.10. Surfaces d'amont obtenues avec l'écoulement de type courant jet.

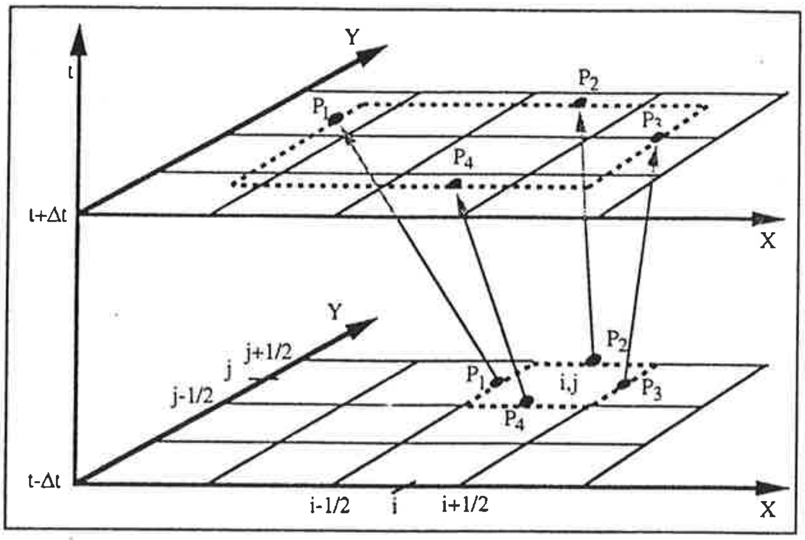

Figure 3.14. La cellule $(i,j)_{t-\Delta t}$ et sa surface d'aval [surface d'aval (i,j) =cellule mobile (i,j) à $t+\Delta t$] sont représentées par les rectangles tiretés sur la grille de calcul à $t-\Delta t$ et $t+\Delta t$ respectivement. Les points P_1 à P_4 définissent la cellule mobile (i,j). Les flèches montrent les trajectoires numériques empruntées par ces points. Les axes et les grilles de calcul sont les mêmes que ceux décrits à la figure 3.2.

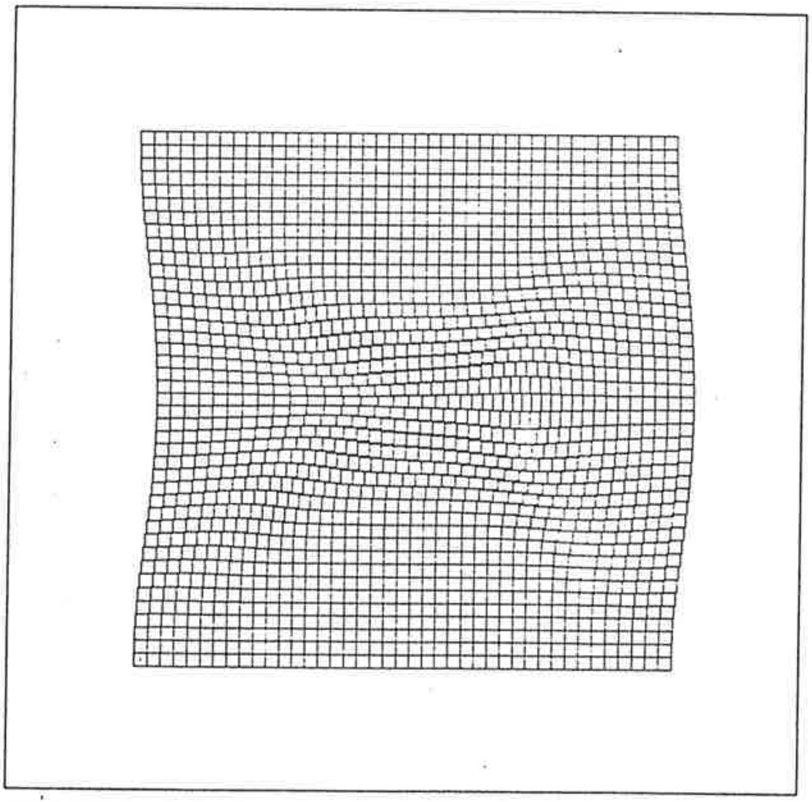

Figure 3.16. Illustration des surfaces aval pour le test du courant jet.Toutes les surfaces sont rectangulaires. Notez le chevauchement et les trous entre les surfaces. Pour une illustration des vents qui ont produit ces surfaces, voir la figure 3.9.

step (see Fig.3.14 for a 2-D illustration). For the two-dimensional problem, the upstream scheme is equivalent to Rancic's (1992) piecewise biparabolic scheme.

In order to test the these schemes, two-dimensional transport problems were solved. The initial mass distribution is shown in Fig.3.8 and the streamfunction corresponding to the transporting "jet" flow is shown in Fig.3.9. The configuration of the upstream membranes for the upstream version is shown in Fig.3.10, and the configuration of the downstream membranes for the downstream version is shown in Fig.3.16. The evolution of the change (in percent) in mass over 80 time steps is shown in Fig.3.13. The solid curve is for the traditional interpolating semi-Lagrangian approach and shows a change of about 2% during the integration. The dotted curve is for the upstream SLIC scheme and confirms that the scheme does indeed conserve the mass. A similar test for the downstream SLIC scheme confirms its mass conservation. In other assessments it is found that, overall, the upstream SLIC scheme performs as well as the interpolating semi-Lagrangian method, conserves mass, and costs about 2-3 times as much. The downstream SLIC scheme is found to be slightly more dispersive, but only costs about 1.5 times as much as the interpolating semi-Lagrangian version. The overhead of the downstream version is smaller because its tracking scheme is simpler than that for the upstream version.

However, there is a problem that is inherent in such mass-flux schemes, but which is not present in the classical semi-Lagrangian approach. This problem is referred to as "fictitious convergence", and appears to be due to the fact that the **area** is not conserved for individual cells, implying that the integrated cell mass is not constant for individual cells which borrow from or lend to neighbours in order to conserve mass overall. This can be illustrated by starting with a constant initial density and using the advecting wind shown in Fig.5.3. The resulting density field after one time step with the upstream SLIC scheme is shown in Fig.5.6.a, and the associated upstream cells are shown in Fig.5.6.b. The corresponding fields for the downstream SLIC scheme are shown in Fig.5.11. Note that the fictitious convergence has generated a 1% density fluctuation for the upstream version, and a 10% density fluctuation for the downstream version. Despite the rather alarming fluctuations produced for this particular flow, in experiments performed with other flows that are thought to be more representative of those found in climate models (Fig.5.13), the two SLIC simulations are found to be competitive with the classical approach and, in addition, provide a perfect conservation of mass (Fig.5.14).

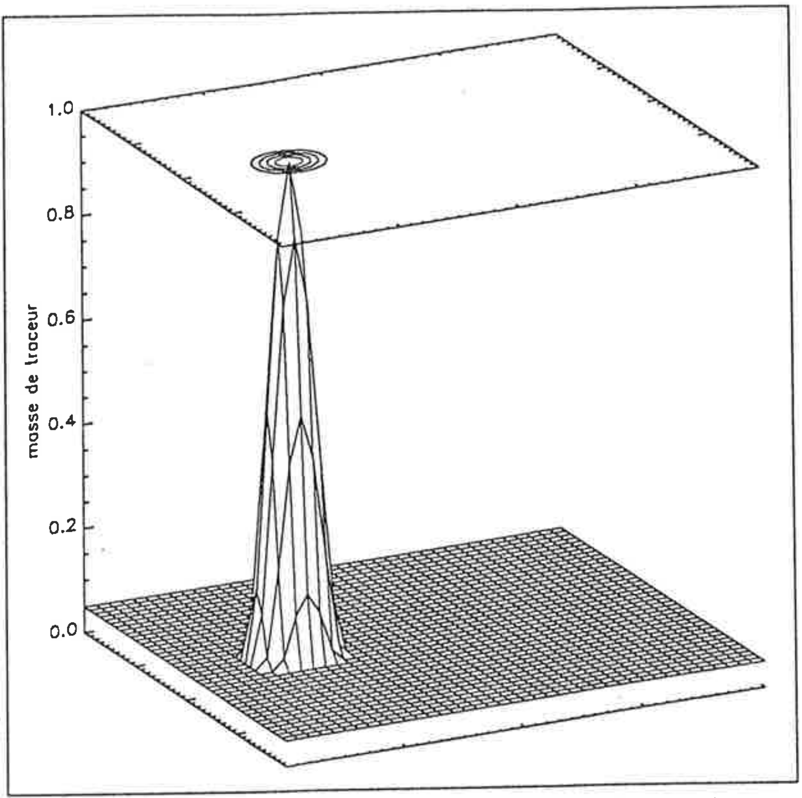

Figure 3.8. Distribution initiale de la masse du traceur pour le test du courant jet.

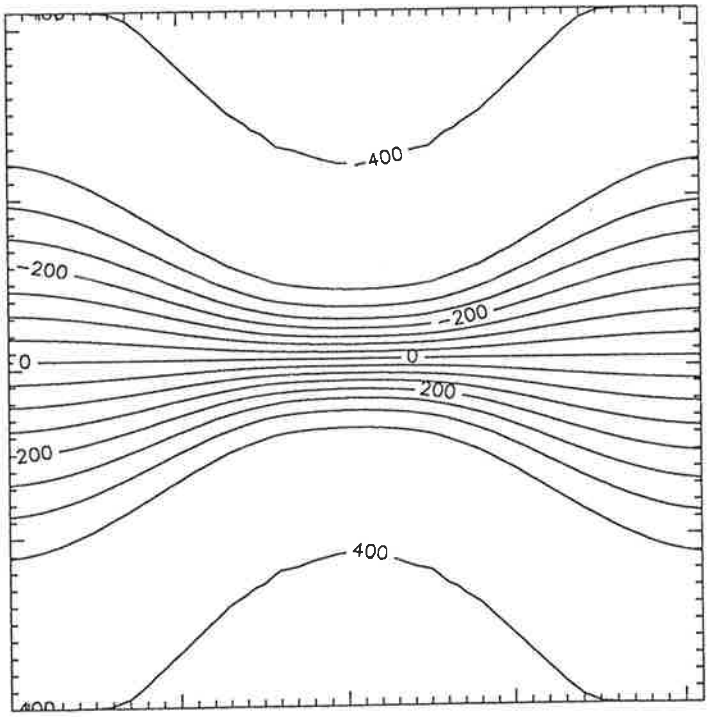

Figure 3.9. Fonction de courant utilisée pour calculer les vents pour le test du jet. Cette fonction de courant est obtenue avec des fonctions trigonométriques que l'on a lissées selon x et y.

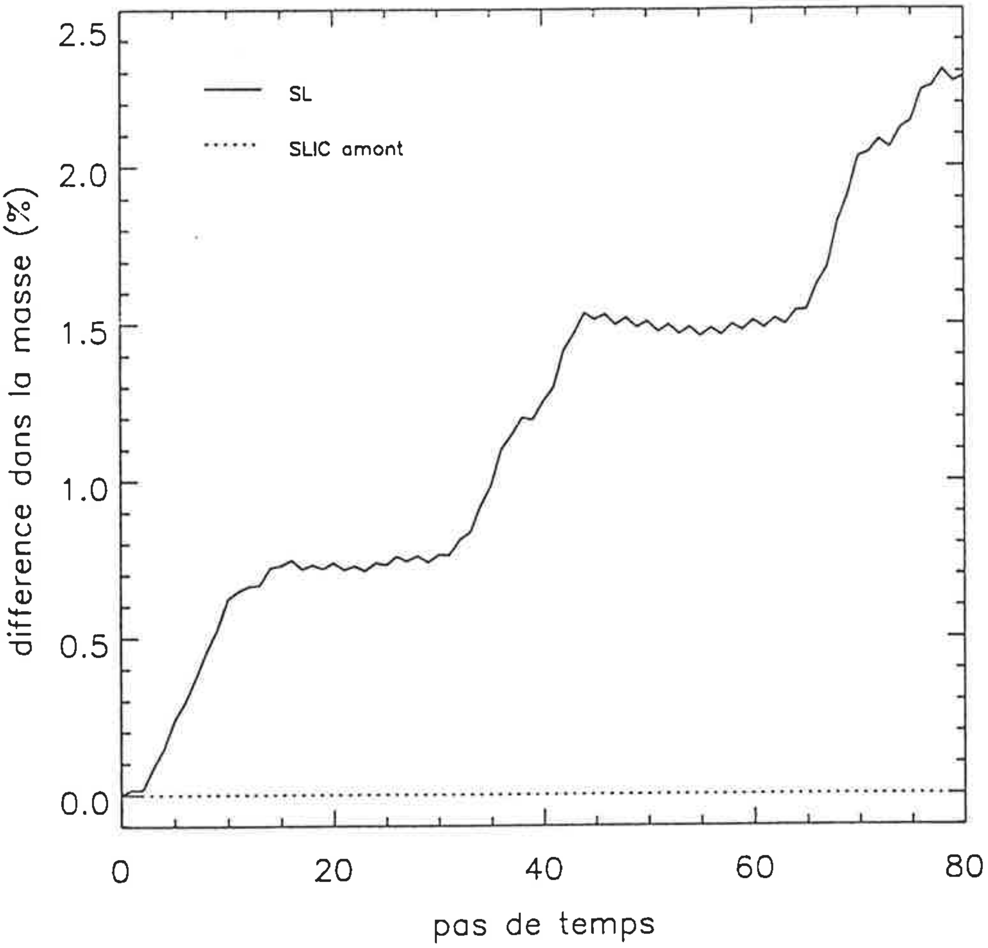

Figure 3.13. Bilan de masse des schémas SLIC amont et SL pour le test du courant jet. L'ordonnée présente la différence en pourcentage entre la masse à un pas de temps donné et la masse initiale, l'abcisse est l'axe temporel.

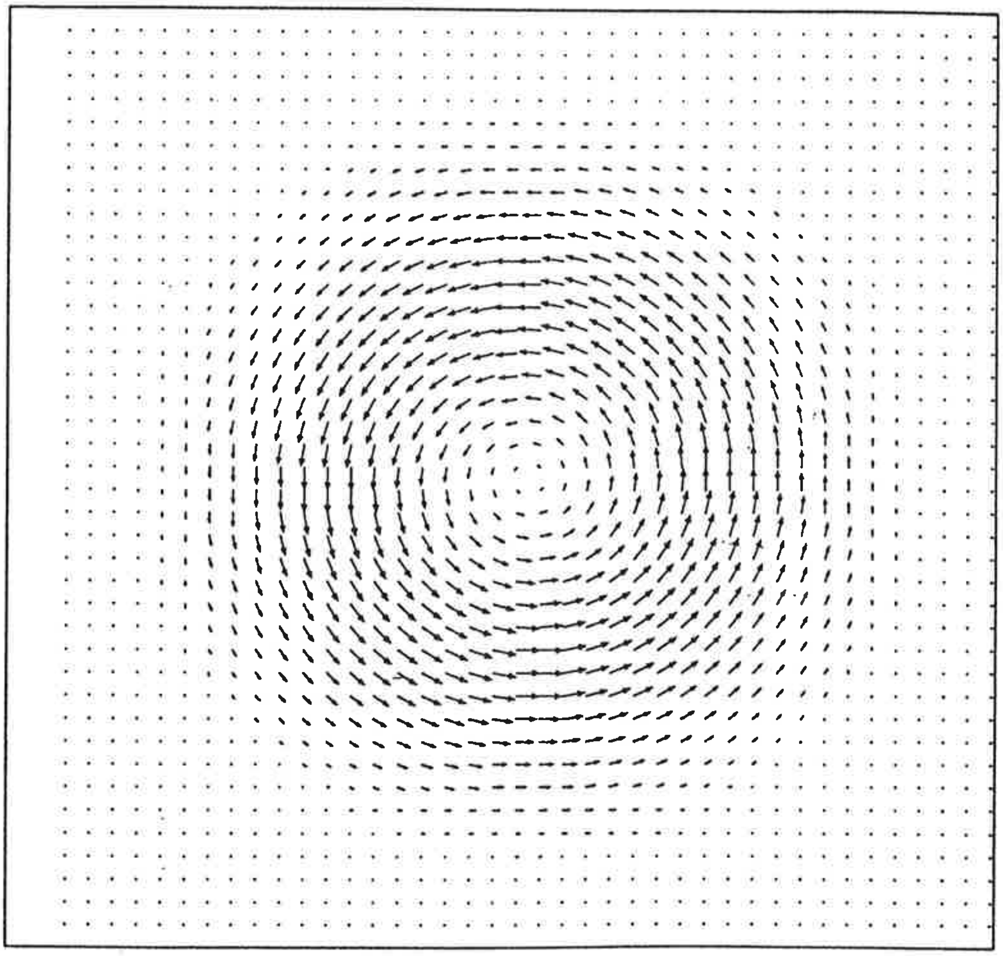

Figure 5.3. Vents produits à partir de la fonction de courant présentée à la figure 5.2; ces vents ont été interpolés linéairement au point de grille de la masse pour fin de présentation seulement.

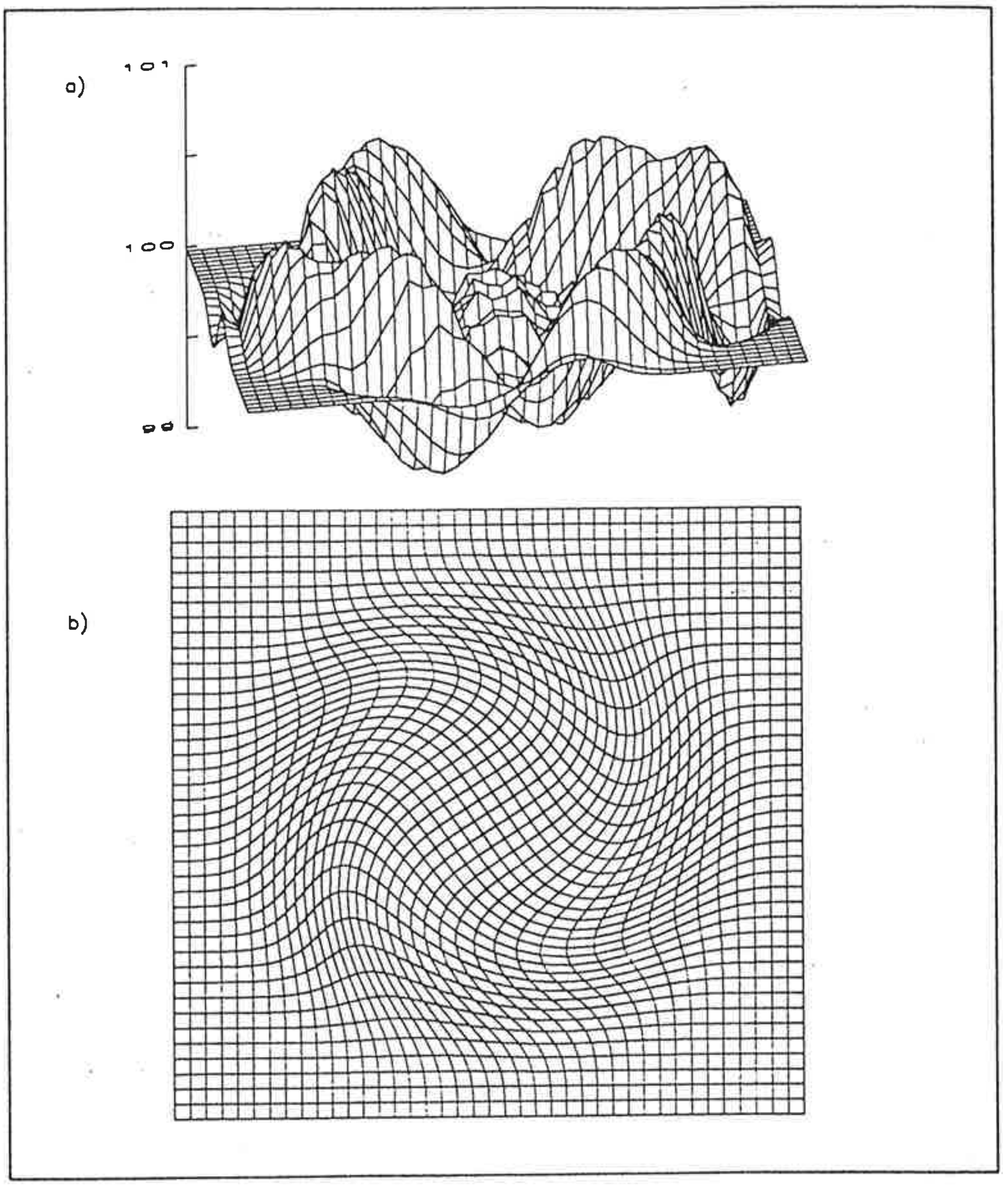

Figure 5.6. La partie a) de la figure montre le champ de masse obtenu avec le schéma SLIC amont pour le troisième cas du test de la rotation solide après 1 pas de temps (nombre de Courant=3,0 et nombre de Lipschitz=0,6). La partie b) montre les surfaces d'amont qui ont servi à faire le calcul.

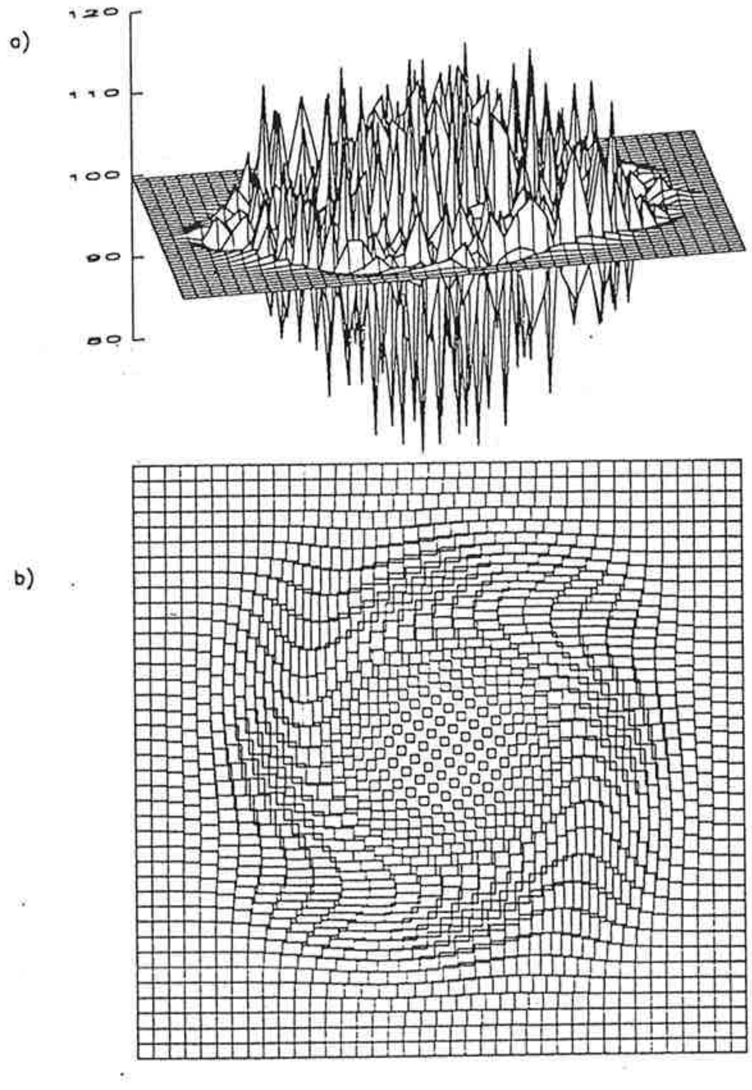

Figure 5.11. La partie a) de la figure montre le champ de masse obtenu avec le schéma SLIC aval pour le troisième cas du test de la rotation solide après 1 pas de temps (nombre de Courant=3,0 et nombre de Lipschitz=0,6). La partie b) montre les surfaces d'amont qui ont servi à faire le calcul.

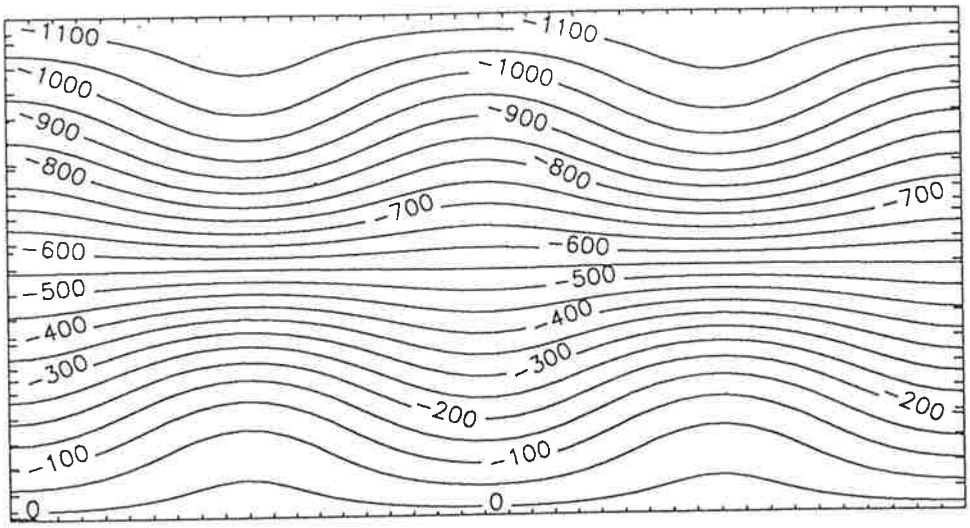

Figure 5.13. Fonction de courant utilisée pour générer des vents s'approchant d'un cas réel retrouvé dans un modèle climatique. Le domaine de calcul est rectangulaire (41 par 21 points de grille) et contient deux jets identiques ayant un nombre de Courant maximal d'environ 0,3.

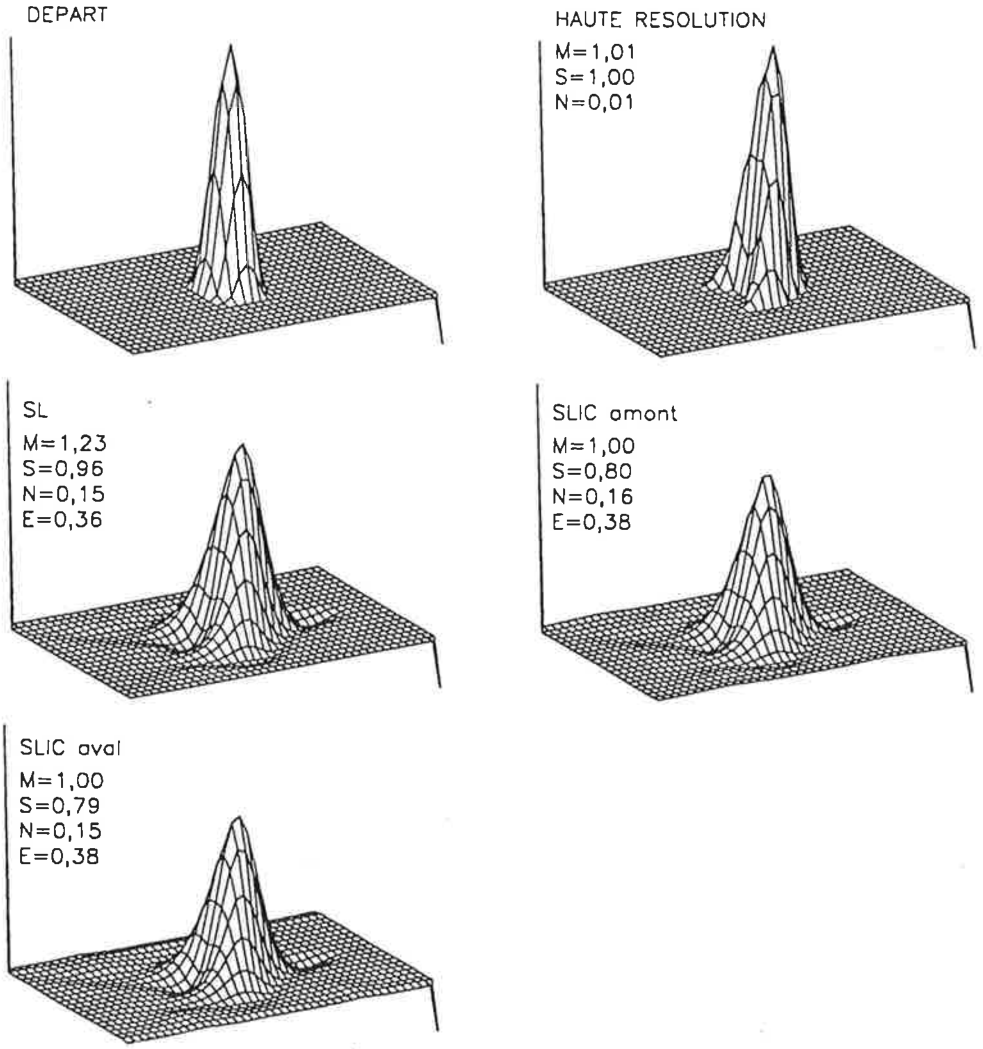

Figure 5.14. Le diagramme noté DÉPART illustre la distribution initiale de la masse dans le domaine: les points hors du pic sont à 50 unités de masse alors que la valeur maximale du pic est de 100 unités de masse. La valeur au point de grille à gauche en arrière plan (pour tous les diagrammes) à été ajustée à 100 unités avant d'afficher le champ dans le but de de faciliter la comparaison. La hauteur de ces traits est donc de 50 unités, soit la hauteur initiale du pic. Le trait à droite au premier plan a la même utilité et mesure -10 unités. Le diagramme noté HAUTE RÉSOLUTION présente le résultat du test à haute résolution alors que les autres diagrammes présentent les résultats obtenus par les modèles dont le nom est inscrit en haut à gauche de chaque diagramme. Les mesures d'erreur M,S,N et E définies par les relations (5.4) à (5.8) sont données pour chaque schémas.

References

Asselin, R., 1972: Frequency filter for time interaions. *Mon. Wea. Rev.*, **100**, 487-490.

Cressman, G.P., 1960: Improved terrain effects in barotropic forecasts. *Mon. Wea. Rev.*, **88**,327-342.

Daley, R., C. Girard, J. Henderson and I. Simmonds, 1976: Short term forecasting with a multi-level spectral primitive equations model. *Atmosphere*, **14**, 98-134.

Manabe, S., J. Smagorinsky and R.F. Strickler, 1965: Simulated climatology of a general circulation model with a hydrologic clcye, *Mon. Wea. Rev.*, **93**, 769-798.

Plante, A., 1992: Transport de substances par schémas numérique semi-lagrangiens intégrés par cellule. M.Sc. thesis (preliminary version), Department of Physics, L'Université du Québec à Montréal, 109pp.

Rancic, M., 1992: Semi-Lagrangian piecewise biparabolic scheme for two-dimensional horizontal advection of a passive scalar. *Mon. Wea. Rev.*, **120**, 1394-1406.

Ritchie, H., 1987: Semi-Lagrangian advection on a Gaussian grid. *Mon. Wea. Rev.*, **115**, 608-619.

Ritchie, H., 1988: Application of the semi-Lagrangian method to a spectral model of the shallow water equations. *Mon. Wea. Rev.*, **116**, 1587-1598.

Ritchie, H., 1991: Application of the semi-Lagrangian method to a multilevel spectral primitive-equations model. *Q.J.R. Meteorol. Soc.*, **117**, 91-106.

Robert, A., 1981: A stable numerical integration scheme for the primitive meteorological equations. *Atmos. Ocean*, **19**, 35-46.

Robert, A., 1982: A semi-Lagrangian and semi-implicit numerical integration scheme for the primitive meteorological equations. *J. Meteor. Soc. Japan*, **60**, 319-325.

Williamson, D.L., and P.J. Rasch, 1989: Two-dimensional semi-Lagrangian transport with shape-preserving interpolation. *Mon. Wea. Rev.*, **117**, 102-129.

Recent and future developments of the ECMWF semi-Lagrangian scheme

Clive Temperton

European Centre for Medium-Range Weather Forecasts
Shinfield Park, Reading, Berkshire, U.K.

1. Introduction

The accuracy of medium-range forecasts has steadily improved with increases in resolution. Consequently, in its four-year plan for the period 1989-1992, ECMWF proposed development of a high-resolution version of its forecast model. A target resolution of a spectral representation with a triangular truncation of 213 waves in the horizontal and 31 levels in the vertical (T213/L31) was set, entailing a doubling of the horizontal resolution and an approximate doubling of the vertical resolution in the troposphere compared to the T106/L19 configuration that was operational at the time (Simmons et al., 1989). In view of the anticipated computer resources, it was clear that major efficiency gains would be necessary in order to achieve this objective. These gains have been provided by the introduction of the semi-Lagrangian treatment of advection permitting about a fourfold increase in the length of the timestep, the use of a reduced Gaussian grid (Hortal and Simmons, 1991) giving a further advantage of about 25%, the introduction of economies in the Legendre transforms (Temperton, 1991), and improvements to the model's basic architecture.

2. Semi-Lagrangian formulation

The general form of the model equations is

$$\frac{dX}{dt} = R \tag{2.1}$$

where

$$\frac{dX}{dt} = \frac{\partial X}{\partial t} + \underset{\sim}{V}_H . \nabla X + \dot{\eta} \frac{\partial X}{\partial \eta} ,$$

$\underset{\sim}{V}_H$ is the horizontal wind and η is the ECMWF hybrid vertical coordinate (Simmons and

Burridge, 1981). A three-time-level semi-Lagrangian treatment of (2.1) is obtained by finding the approximate trajectory, over the time interval $[t-\Delta t,\ t+\Delta t]$, of a particle which arrives at each gridpoint $\underset{\sim}{x}$ at time $(t+\Delta t)$. The trajectories are found as in Ritchie (1988, 1991). Equation (2.1) is then approximated by

$$\frac{X^{+}-X^{-}}{2\Delta t} = R^{0} \tag{2.2}$$

where the subscripts $+, 0, -$ respectively denote evaluation at the arrival point $(\underset{\sim}{x},\ t+\Delta t)$, the mid-point of the trajectory $(\underset{\sim}{x}-\underset{\sim}{\alpha},\ t)$, and the departure point $(\underset{\sim}{x}-2\underset{\sim}{\alpha},\ t-\Delta t)$. Since the mid-point and the departure point will not in general coincide with model gridpoints, X^{-} and R^{0} must be determined by interpolation.

It is more economical (and sometimes gives better results) to evaluate the right-hand side of (2.2) as

$$R^{0} = \frac{1}{2}\left[R(\underset{\sim}{x}-2\underset{\sim}{\alpha},\ t) + R(\underset{\sim}{x},\ t)\right] \tag{2.3}$$

since only a single interpolation [of the combined field $X(t-\Delta t)+\Delta t R(t)$ at the point $(\underset{\sim}{x}-2\underset{\sim}{\alpha})$] is then required in order to determine X^{+}.

The right-hand sides of the time-discretized model equations also contain semi-implicit correction terms, which in the Eulerian model took the form

$$\Delta_{tt}X = (X^{+} - 2X^{0} + X^{-})$$

where the superscripts refer to time-levels, and to a single common gridpoint. In the semi-Lagrangian version of the model, the semi-implicit correction terms take the form

$$\Delta_{tt}X = (X(\underset{\sim}{x},\ t+\Delta t) - X(\underset{\sim}{x},\ t)) + (X(\underset{\sim}{x}-2\underset{\sim}{\alpha},\ t-\Delta t) - X(\underset{\sim}{x}-2\underset{\sim}{\alpha},\ t)) \tag{2.4}$$

and again the terms to be evaluated at the departure point $(\underset{\sim}{x}-2\underset{\sim}{\alpha})$ can be added to other right-hand side terms before interpolation. Notice that the evaluation of $\Delta_{tt}X$, and both ways of evaluating R^{0}, are all centered in space and time.

An alternative form, referred to as "non-interpolating in the vertical" (Ritchie, 1991), replaces (2.1) by

$$\frac{d_{H}X}{dt} + \dot{\eta}^{*}\frac{\partial X}{\partial \eta} = R - \dot{\eta}\frac{\partial X}{\partial \eta} + \dot{\eta}^{*}\frac{\partial X}{\partial \eta} \tag{2.5}$$

where

$$\frac{d_H X}{dt} = \frac{\partial X}{\partial t} + \underset{\sim}{v}_H \cdot \nabla X$$

and $\dot{\eta}^*$ is a modified vertical velocity such that the resulting departure point lies exactly on a model level. The left-hand side of (2.5) is then discretized in the same way as that of (2.1); since the modified departure point is defined to be on a model level, evaluation of quantities there requires only horizontal interpolation.

Following Ritchie (1988, 1991), the momentum equations are integrated in *vector* form to avoid an instability of the metric term near the poles. Ignoring the horizontal diffusion (which is handled later, in spectral space), the semi-Lagrangian discretization is

$$\begin{aligned}\frac{\underset{\sim}{V}_H^+ - \underset{\sim}{V}_H^-}{2\Delta t} &+ [\; f\underset{\sim}{k} \times \underset{\sim}{v}_H + \nabla\phi + R_d T_v \nabla \ln p \;]^0 \\ &= P_{\underset{\sim}{v}} - \frac{1}{2}\Delta_{tt}\nabla[\underline{\gamma} T + R_d T_r \ln p_s]\end{aligned} \tag{2.6}$$

where $\underline{\gamma}$ is a linearization of the hydrostatic matrix and T_r is the reference temperature for the semi-implicit scheme.

The thermodynamic and moisture equations become

$$\frac{T^+ - T^-}{2\Delta t} - [\frac{\kappa T_v \omega}{(1+(\delta-1)q)p}]^0 = P_T - \frac{1}{2}\Delta_{tt}(\underline{\tau} D) \tag{2.7}$$

where $\underline{\tau}$ is another matrix of the semi-implicit scheme (the details are in Simmons and Burridge, 1981), and

$$\frac{q^+ - q^-}{2\Delta t} = P_q \; . \tag{2.8}$$

The terms $P_{\underset{\sim}{v}}$, P_T, P_q in (2.6)-(2.8) represent the contributions of the physical parameterizations, which are evaluated at the arrival gridpoint. In (2.6)-(2.8) the semi-Lagrangian discretization has been expressed in its "fully interpolating" form corresponding to (2.1)-(2.2).

The vertically discretized continuity equation may be written

$$\Delta B_k \frac{d}{dt}(\ln p_s) - \Delta B_k [\frac{\partial(\ln p_s)}{\partial t} + \underset{\sim}{v}_k \cdot \nabla \ln p_s] = 0 \tag{2.9}$$

where

$$\frac{\partial}{\partial t}(\ln p_s) = -\sum_{k=1}^{NLEV} [\frac{1}{p_s} D_k \Delta p_k + (\underset{\sim}{v}_k \cdot \nabla \ln p_s)\Delta B_k] \; .$$

Integrating in the vertical and including the semi-implicit correction terms, the semi-Lagrangian discretization of (2.9) becomes

$$(\ln p_s)^+ = \sum_{k=1}^{NLEV} \Delta B_k [(\ln p_s)^- + 2\Delta t (\frac{\partial(\ln p_s)}{\partial t} + \underset{\sim}{v}_k . \nabla \ln p_s)^0$$

$$- \frac{\Delta t}{p_s^r} \Delta_{tt} (\sum_{j=1}^{NLEV} (\Delta p_j^r D_j))] \;. \qquad (2.10)$$

It is important to bear in mind that each contribution to the sum on the right-hand side of (2.10) involves a different trajectory.

In practice it was found sufficiently accurate to use linear interpolation for the trajectory calculations and for "right-hand-side" terms evaluated at the mid-point of the trajectory, but essential to use cubic interpolation (or at least an economical approximation to it) for terms evaluated at the departure points. After some experimentation, it was decided to compute the right-hand side terms of the momentum equations by averaging along the trajectory as in (2.3), but to evaluate the right-hand side terms of the other equations at the mid-point of the trajectory.

3. Note on CPU time

The semi-Lagrangian version of the model can be run stably with timesteps several times longer than for the Eulerian formulation. At the same time, the computation per timestep is more expensive and it is important that the additional overhead remains modest. For the T213/L31 model using a 15-minute timestep, it was found that the "semi-Lagrangian" routines (trajectory calculations and interpolations) took 27% of the CPU time for the fully interpolating version of the scheme, and 20% of the CPU time for the "non-interpolating in the vertical" version. The "semi-Lagrangian overhead" is in fact slightly less than these figures suggest, since there is at the same time a reduction in the number of Legendre transforms required in comparison with the Eulerian formulation.

In the case of the "non-interpolating in the vertical" scheme, the semi-Lagrangian calculations have been optimized by making use of the observation that, in the course of a typical 10-day T213/L31 forecast with a 15-minute timestep, the "modified" departure point was at the same model level as the arrival point on 99.76% of occasions. Thus, the treatment of the vertical advection is in fact Eulerian almost everywhere. As a result, three-dimensional interpolations collapse to two-dimensional interpolations with an occasional local correction, while the additional terms in the "non-interpolating" scheme, which in principle require extra interpolations, need only be evaluated at a few points.

4. Results

The experiments reported on here were performed with a high resolution version of the ECMWF forecast model having a spectral representation in the horizontal with a triangular 213-wave truncation (T213), and 31 levels in the vertical. The baseline semi-Lagrangian version is the "vertically non-interpolating" scheme which has been used operationally at ECMWF since August 1992. In order to compare various formulations, sets of integrations consisting of 12 independent cases (starting from operational analyses on the 15th of each month during the first year following the implementation of the T213/L31 model on September 17, 1991) were performed.

The main motivation for using a semi-Lagrangian formulation is to permit the use of time steps that far exceed the Courant-Friedrichs-Lewy (CFL) stability criterion for the corresponding Eulerian model, thus enhancing the model efficiency, provided that the additional time truncation error does not significantly decrease the accuracy. Figure 1 shows the mean objective scores (averaged over the 12 cases) for the northern hemisphere, comparing the Eulerian version with a 3 minute timestep (solid) and the semi-Lagrangian version with a 15 minute timestep (dashed). Figure 2 shows the corresponding result for the southern hemisphere. It is seen that the accuracies are almost equivalent, particularly for forecasts whose skill exceeds the 60% threshhold. Thus, even at this high resolution, the semi-Lagrangian scheme is permitting a fivefold increase in timestep with no significant degradation in the quality of the forecasts. In section 3 it was seen that the overhead of the semi-Lagrangian scheme is approximately 20%, so the semi-Lagrangian version gives an efficiency improvement of about a factor of 4 relative to the Eulerian in this comparison.

The T213/L31 model was implemented operationally in September 1991 using the "fully interpolating" version of the semi-Lagrangian scheme. The higher resolution version immediately demonstrated clear improvements in the forecasts in the first few days of the 10-day forecast range. However, despite extensive parallel testing before implementation, during the subsequent months it was found that, relative to the former operational version, there was increased day-to-day variability in the forecasts in the medium-range. The levels of eddy kinetic energy were typically higher with this version, too. Following several studies to try to determine which aspects of the semi-Lagrangian formulation were responsible for this behaviour, attention focussed on the option of using the "vertically non-interpolating" scheme (Ritchie, 1991). This scheme was included quite early on in the Centre's semi-Lagrangian code, but was not fully validated during the development of the code because it was not expected to be necessary at the higher vertical resolution.

Tests of this option revealed a positive impact on objective measures of skill. This is evident in the anomaly correlations at 1000 hPa and 500 hPa for the northern hemisphere (Figures 3(a) and (b)), as well as in the corresponding root-mean-square height errors (Figures 3(c) and (d)). The improvement is even more striking in the results for the European region, as seen in Figure 4. Moreover, levels of eddy activity are generally lower (and more realistic) with this version than with the fully interpolating scheme.

Also, differences in zonal-mean temperature between semi-Lagrangian and Eulerian forecasts are substantially reduced at upper levels when the semi-Lagrangian scheme is changed to the vertically non-interpolating form. The reason for the different behaviour of the fully interpolating scheme is not entirely understood. Ritchie (1991) originally attributed it to an excessive smoothing in the fully interpolating version due to vertical interpolation through the tropopause where all the dynamic fields vary abruptly in the vertical. This was based on five-day experiments with a baroclinic model that included only very simple parameterizations. More recently Williamson and Olson (1993) have examined climate simulations using a semi-Lagrangian version of the NCAR CCM2 which includes sophisticated physical parameterizations, and have concluded that the fully interpolating version actually reduces deficiencies that the former Eulerian version had in the vicinity of the tropopause. These are points that warrant further investigation. In any case, the present results in terms of medium-range forecasts with a high resolution, fully parameterized forecast model indicate a clear advantage for the vertically non-interpolating semi-Lagrangian scheme. It was implemented operationally in August 1992 and the anticipated improvement was realized.

By virtue of its increased efficiency, incorporation of the semi-Lagrangian scheme was very important in enabling an increase in horizontal resolution from T106 to T213 in the operational ECMWF forecast model. It is of interest to document the impact of this increase in horizontal resolution for the set of 12 cases studied here. In Figure 5 we see the marked improvement in the objective scores (mean anomaly correlations and root-mean-square height errors at 1000 and 500 hPa) for the northern hemisphere. Figure 6 presents the corresponding results for the European region. In these tests the same 31 level configuration was used for both horizontal resolutions. It is seen that this increase in horizontal resolution indeed had a very significant positive impact which, in fact, is substantially greater than the impact of any of the other changes that have been presented in the previous figures.

Several additional sets of tests were performed to study the impact of some of the optimizations that have been incorporated in the operational semi-Lagrangian T213/L31 model. These optimizations leave the objective scores virtually unchanged, but produce worthwhile extra efficiency gains that help reduce the semi-Lagrangian overheads. In particular, it was confirmed that there is no significant degradation resulting from using linear rather than cubic interpolation, and only one iteration rather than two, in calculating the trajectories. Optimizations based on approximations to the spherical trigonometry are also used in the calculation of the departure points. The versions implemented correspond to those presented in section 2(b) of Ritchie and Beaudoin (1993), except that only the terms accurate to second order in the timestep are explicitly retained.

5. Summary and plans

Conversion of the ECMWF spectral model to semi-Lagrangian form was essential in enabling the operational implementation of the high-resolution (T213/L31) version. It was found that the semi-Lagrangian version with a 15-minute timestep gave an accuracy equivalent to that of an Eulerian version with a 3-minute timestep, giving an improvement of around a factor of 4 in efficiency. The "non-interpolating in the vertical" form of the semi-Lagrangian scheme was found to give better forecasts than the "fully interpolating" form, though the reasons for this are still not completely understood. Finally, it was confirmed that increasing the horizontal resolution from T106 to T213 has a significant positive impact on the forecasts.

Future plans for the model include the development of a version in which the moisture is treated entirely in gridpoint space (Williamson and Rasch, 1993), and the development of a two-time-level scheme (see for example McDonald and Haugen, 1993).

REFERENCES

Hortal, M., and A.J. Simmons, 1991: Use of reduced Gaussian grids in spectral models. *Mon. Wea. Rev.*, **119**, 1057-1074.

McDonald, A., and J.E. Haugen, 1993: A two time-level, three-dimensional semi-Lagrangian, semi-implicit, limited-area gridpoint model of the primitive equations. Part II: Extension to hybrid vertical coordinates. *Mon. Wea. Rev.*, **121**, 2077-2087.

Ritchie, H., 1988: Application of the semi-Lagrangian method to a spectral model of the shallow water equations. *Mon. Wea. Rev.*, **116**, 1587-1598.

Ritchie, H., 1991: Application of the semi-Lagrangian method to a multilevel spectral primitive-equations model. *Quart. J. Roy. Meteor. Soc.*, **117**, 91-106.

Ritchie, H., and C. Beaudoin, 1993: Optimization and sensitivity experiments with a baroclinic semi-Lagrangian spectral model. Submitted to *Mon. Wea. Rev.*

Simmons, A.J., and D.M. Burridge, 1981: An energy and angular momentum conserving vertical finite difference scheme and hybrid vertical coordinates. *Mon. Wea. Rev.*, **109**, 758-766.

Simmons, A.J., D.M. Burridge, M. Jarraud, C. Girard, and W. Wergen, 1989: The ECMWF medium-range prediction models: development of the numerical formulations and the impact of increased resolution. *Meteorol. Atmos. Phys.*, **40**, 28-60.

Temperton, C., 1991: On scalar and vector transform methods for global spectral models. *Mon. Wea. Rev.*, **119**, 1303-1307.

Williamson, D.L., and J.G. Olson, 1993: Climate simulations with a semi-Lagrangian version of the NCAR CCM2. Submitted to *Mon. Wea. Rev.*

Williamson, D.L., and P.J. Rasch, 1993: Water vapor transport in the NCAR CCM2. Submitted to *Tellus*.

FIGURE LEGENDS

Fig.1: Mean objective scores for the northern hemisphere comparing the Eulerian version with a 3 min timestep (solid) and the semi-Lagrangian version with a 15 min timestep (dashed):

- (a) anomaly correlation of 1000 hPa height
- (b) anomaly correlation of 500 hPa height
- (c) root-mean-square error of 1000 hPa height (metres)
- (d) root-mean-square error of 500 hPa height (metres).

Fig.2: As in Fig.1 except for southern hemisphere.

Fig.3: Mean objective scores for the northern hemisphere comparing the vertically non-interpolating (solid) and fully interpolating (dashed) semi-Lagrangian versions:

- (a) anomaly correlation of 1000 hPa height
- (b) anomaly correlation of 500 hPa height
- (c) root-mean-square error of 1000 hPa height (metres)
- (d) root-mean-square error of 500 hPa height (metres).

Fig.4: As in Fig.3 except for the European region.

Fig.5: Mean objective scores for the northern hemisphere comparing T213 horizontal resolution (solid) and T106 horizontal resolution (dashed):

- (a) anomaly correlation of 1000 hPa height
- (b) anomaly correlation of 500 hPa height
- (c) root-mean-square error of 1000 hPa height (metres)
- (d) root-mean-square error of 500 hPa height (metres).

Fig.6: As in Fig.5 except for the European region.

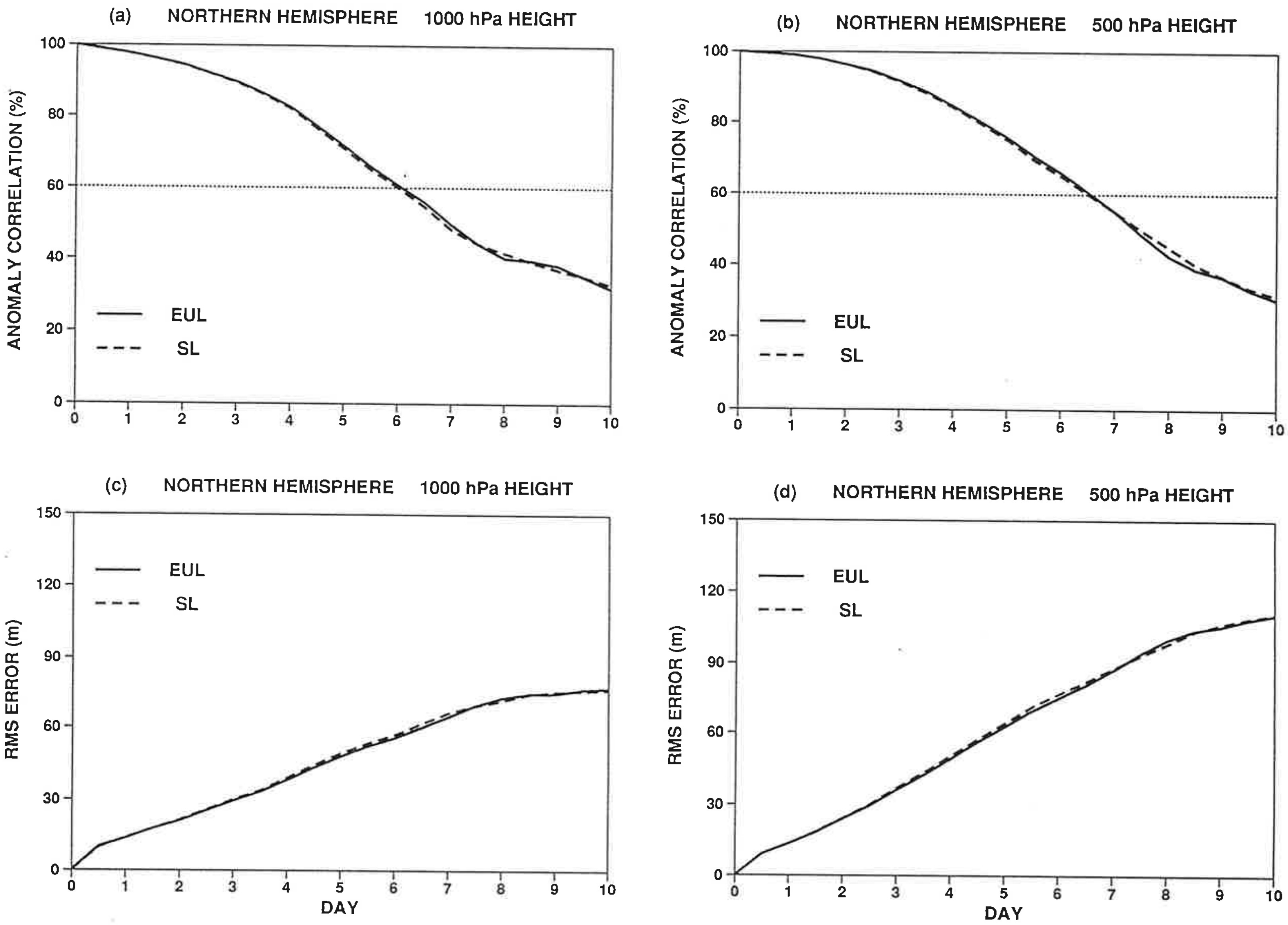
(a) NORTHERN HEMISPHERE 1000 hPa HEIGHT
(b) NORTHERN HEMISPHERE 500 hPa HEIGHT
(c) NORTHERN HEMISPHERE 1000 hPa HEIGHT
(d) NORTHERN HEMISPHERE 500 hPa HEIGHT
ANOMALY CORRELATION (%)
RMS ERROR (m)
DAY
EUL
SL
0
20
40
60
80
100
30
90
120
150
1
2
3
4
5
6
7
8
9
10

Figure 1

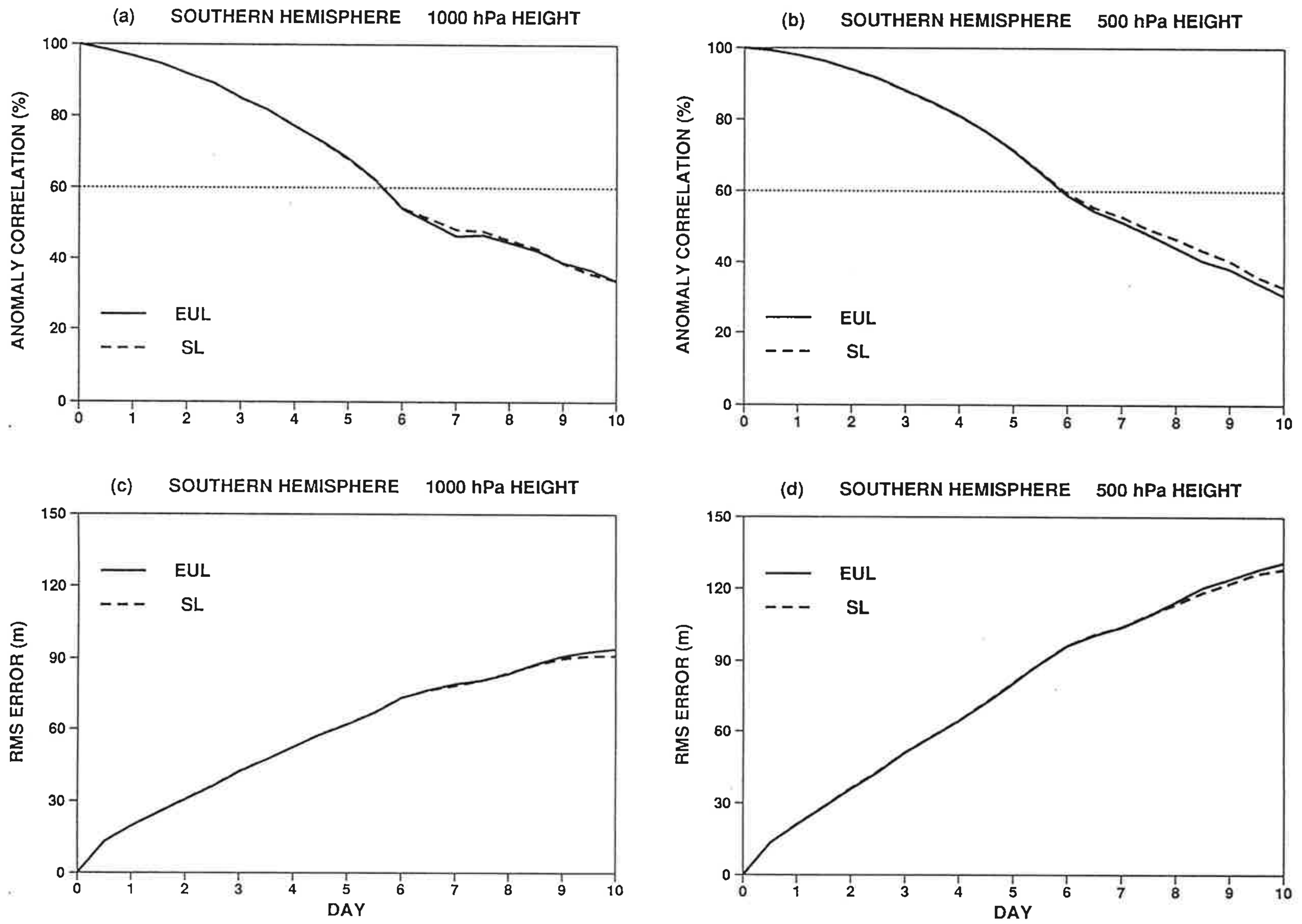
(a) SOUTHERN HEMISPHERE 1000 hPa HEIGHT
(b) SOUTHERN HEMISPHERE 500 hPa HEIGHT
(c) SOUTHERN HEMISPHERE 1000 hPa HEIGHT
(d) SOUTHERN HEMISPHERE 500 hPa HEIGHT
ANOMALY CORRELATION (%)
RMS ERROR (m)
DAY
EUL
SL
0
20
40
60
80
100
30
90
120
150
1
2
3
4
5
6
7
8
9
10

Figure 2

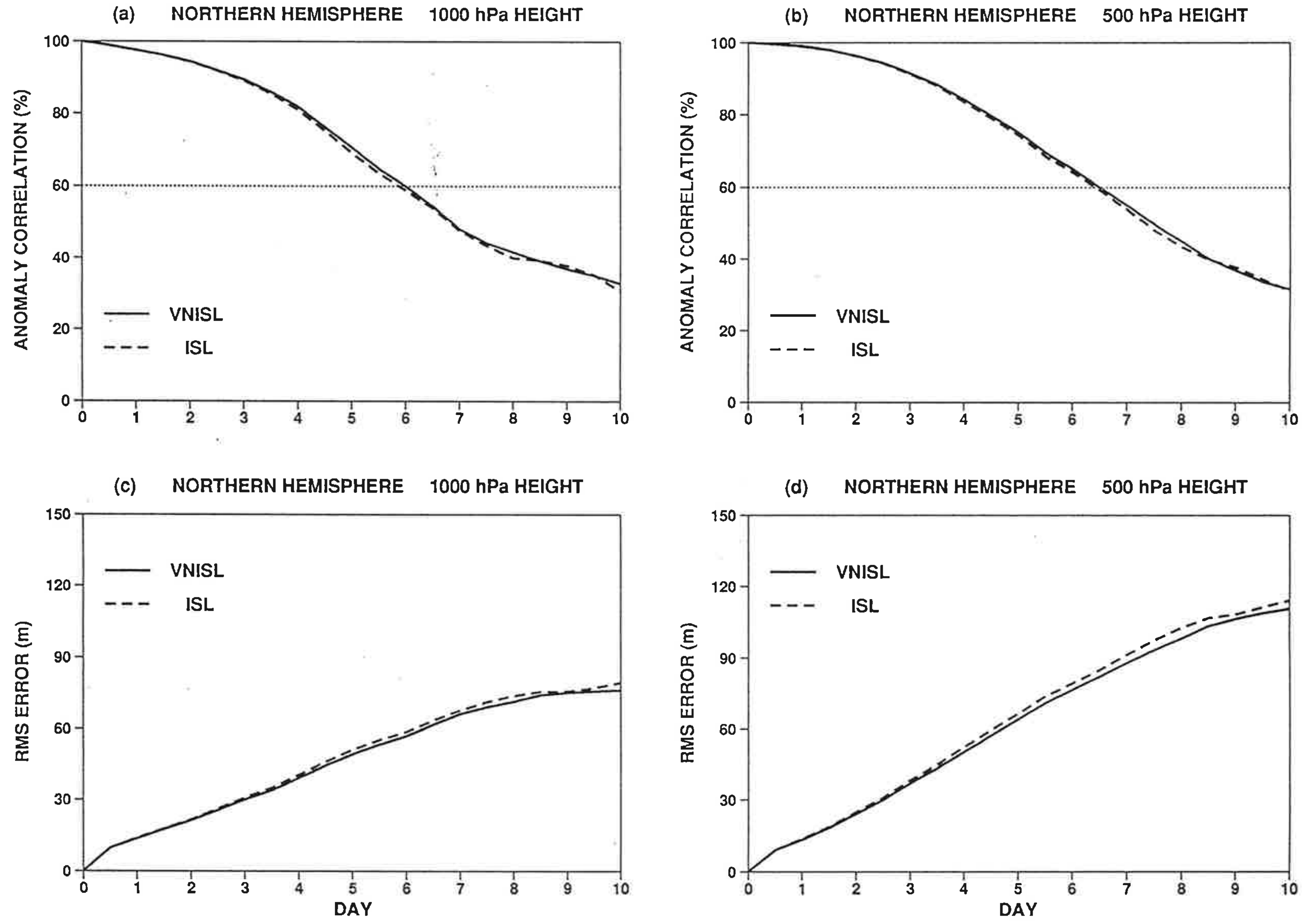
(a) NORTHERN HEMISPHERE 1000 hPa HEIGHT
ANOMALY CORRELATION (%)
100
80
60
40
20
0
VNISL
ISL
0
1
2
3
4
5
6
7
8
9
10
(b) NORTHERN HEMISPHERE 500 hPa HEIGHT
ANOMALY CORRELATION (%)
100
80
60
40
20
0
VNISL
ISL
0
1
2
3
4
5
6
7
8
9
10
(c) NORTHERN HEMISPHERE 1000 hPa HEIGHT
RMS ERROR (m)
150
120
90
60
30
0
VNISL
ISL
0
1
2
3
4
5
6
7
8
9
10
DAY
(d) NORTHERN HEMISPHERE 500 hPa HEIGHT
RMS ERROR (m)
150
120
90
60
30
0
VNISL
ISL
0
1
2
3
4
5
6
7
8
9
10
DAY

Figure 3

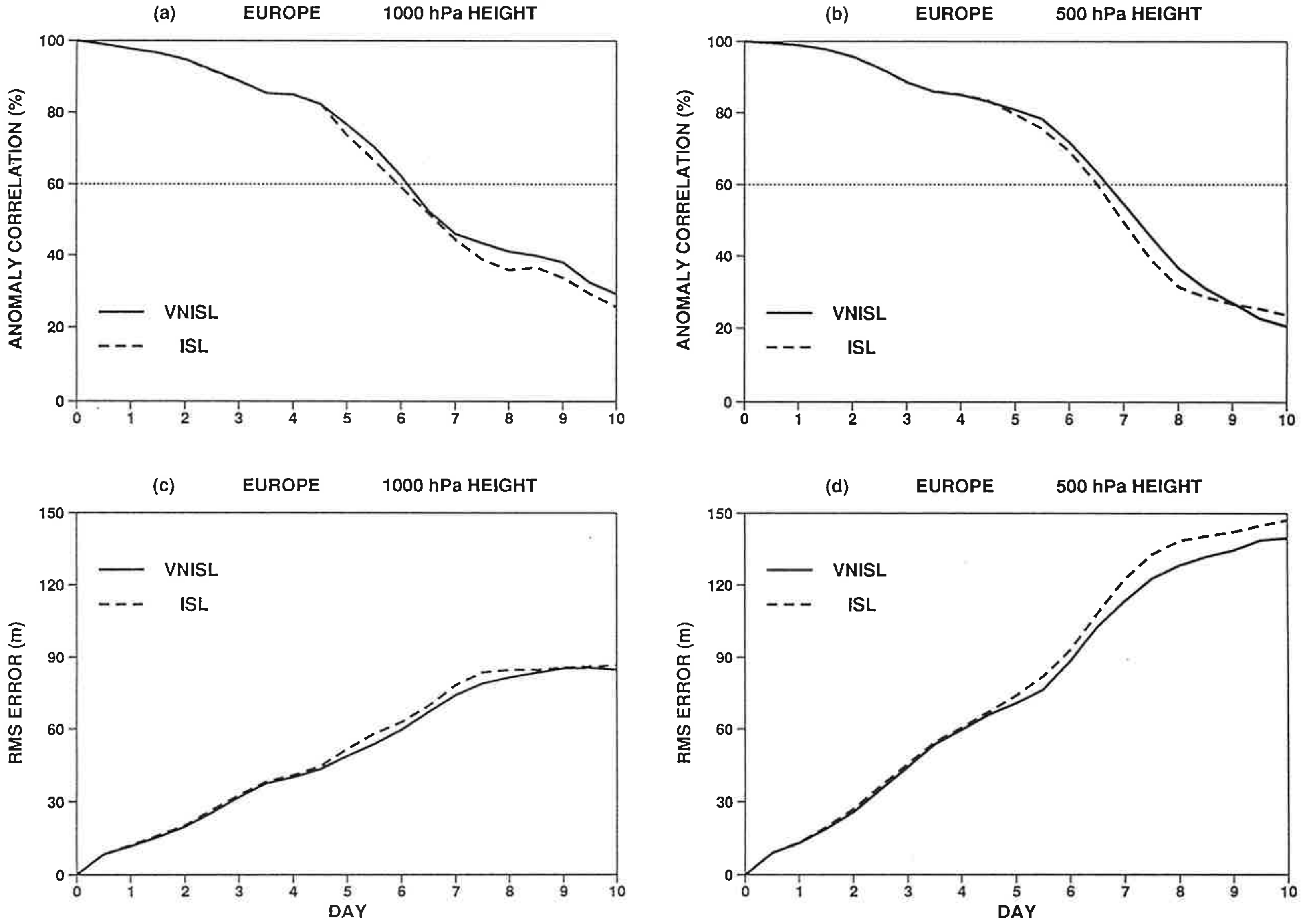
(a) EUROPE 1000 hPa HEIGHT
ANOMALY CORRELATION (%)
100
80
60
40
20
0
0 1 2 3 4 5 6 7 8 9 10
VNISL
ISL
(b) EUROPE 500 hPa HEIGHT
ANOMALY CORRELATION (%)
100
80
60
40
20
0
0 1 2 3 4 5 6 7 8 9 10
VNISL
ISL
(c) EUROPE 1000 hPa HEIGHT
RMS ERROR (m)
150
120
90
60
30
0
0 1 2 3 4 5 6 7 8 9 10
DAY
VNISL
ISL
(d) EUROPE 500 hPa HEIGHT
RMS ERROR (m)
150
120
90
60
30
0
0 1 2 3 4 5 6 7 8 9 10
DAY
VNISL
ISL

Figure 4

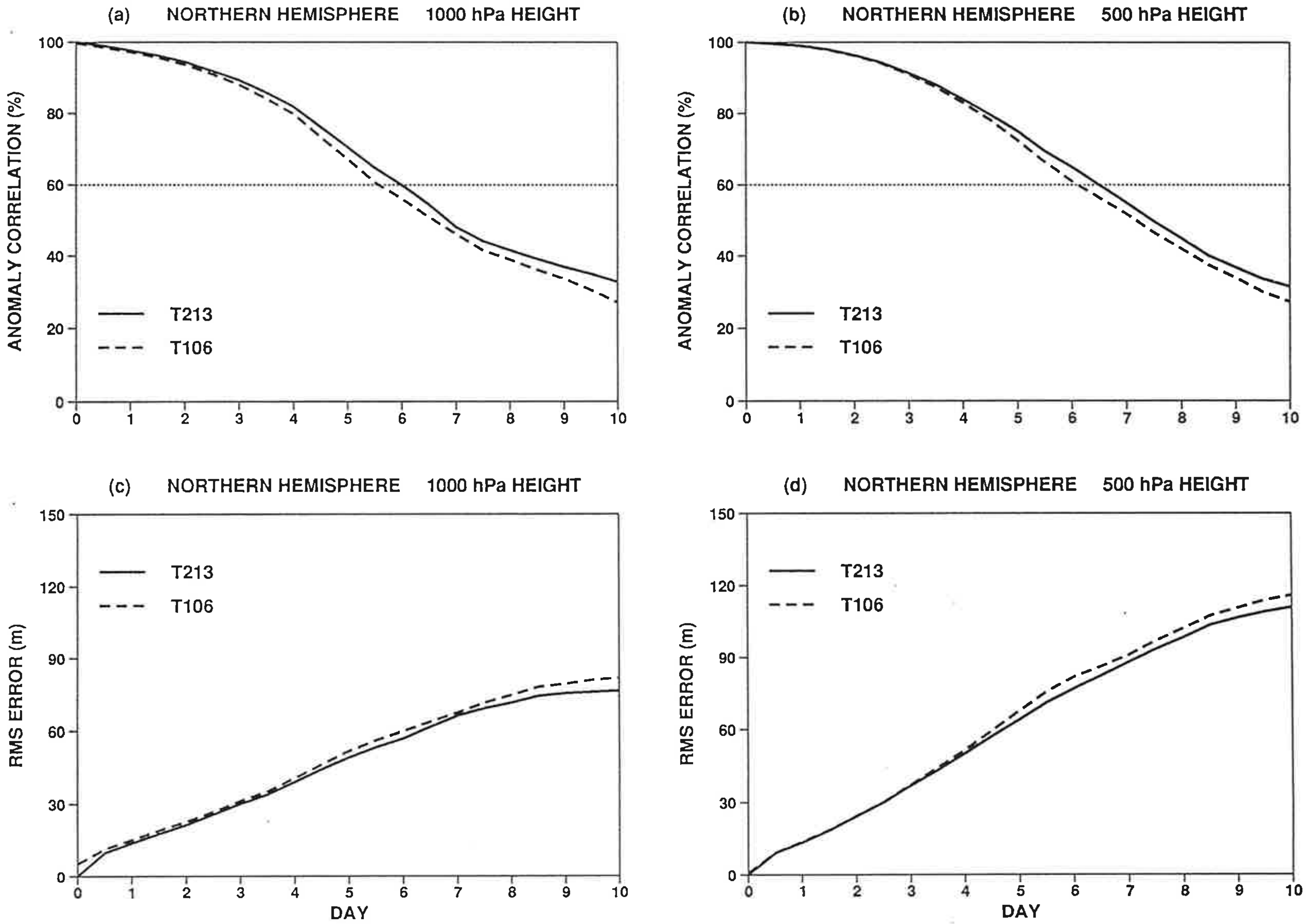
(a) NORTHERN HEMISPHERE 1000 hPa HEIGHT
(b) NORTHERN HEMISPHERE 500 hPa HEIGHT
(c) NORTHERN HEMISPHERE 1000 hPa HEIGHT
(d) NORTHERN HEMISPHERE 500 hPa HEIGHT
ANOMALY CORRELATION (%)
RMS ERROR (m)
DAY
0
20
40
60
80
100
30
90
120
150
1
2
3
4
5
6
7
8
9
10
T213
T106

Figure 5

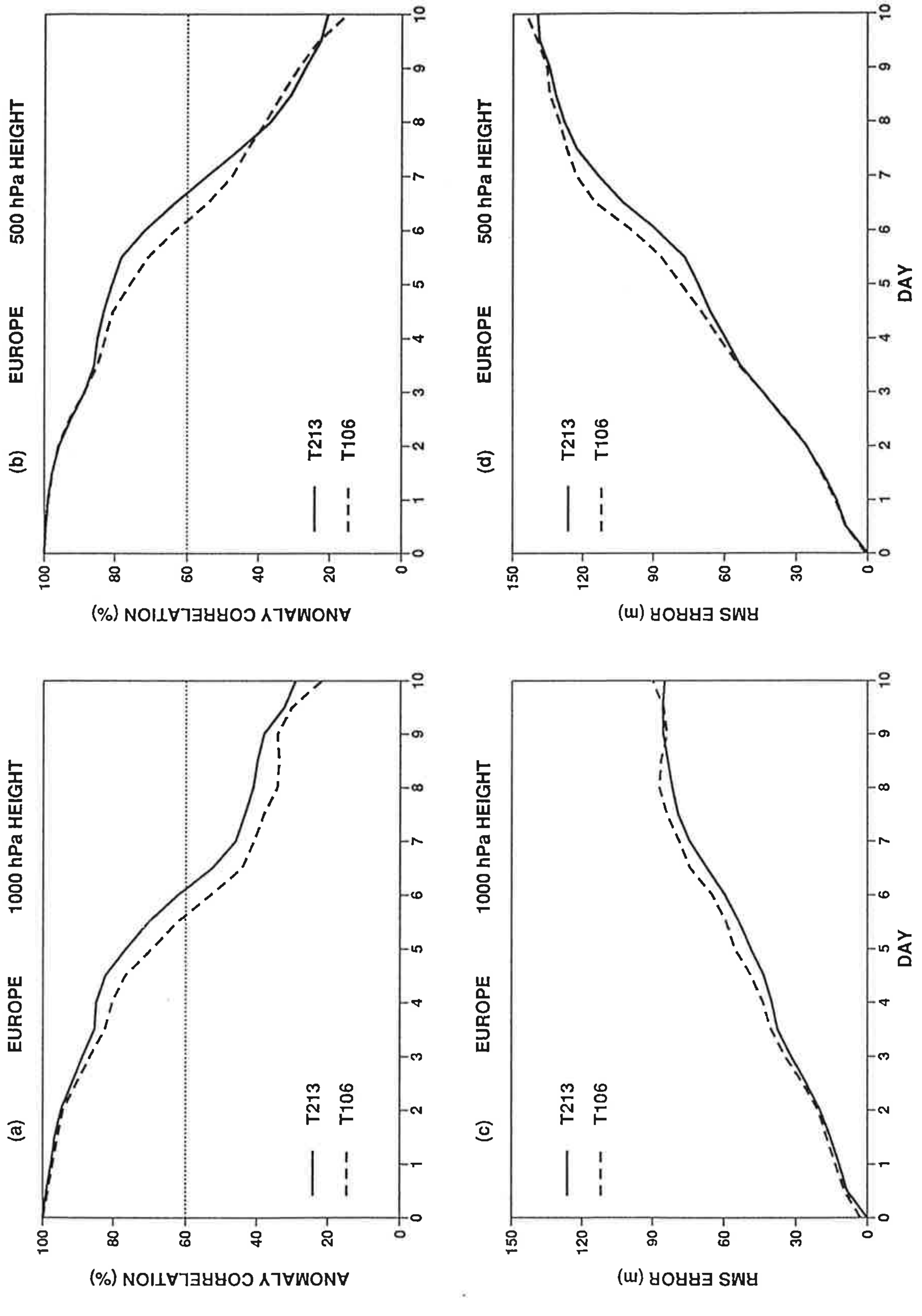
(a) EUROPE 1000 hPa HEIGHT
(b) EUROPE 500 hPa HEIGHT
(c) EUROPE 1000 hPa HEIGHT
(d) EUROPE 500 hPa HEIGHT
ANOMALY CORRELATION (%)
RMS ERROR (m)
DAY
T213
T106
0
20
40
60
80
100
30
90
120
150
1
2
3
4
5
6
7
8
9
10

Figure 6

A Semi-Lagrangian Version of the NCAR CCM2 and Examples of Climate Simulations

David L. Williamson

National Center for Atmospheric Research *

Boulder, CO 80307

Introduction

We have developed a semi-Lagrangian version of the Community Climate Model (CCM2) at NCAR. The design goal was to produce a semi-Langrangian version which differed from the Eulerian version only in the advection approximation. At the same time, consistency between the discrete continuity equation and the vertical velocity ω in the energy conversion term of the thermodynamic equation was desired, along with consistency between the conversion term and the pressure gradient term in the momentum equations. To achieve the former consistency, slight changes are required in the discrete approximations to the vertical integral in the ω approximation in the original Eulerian form of CCM2. To achieve the latter, the original hydrostatic approximation must then also be modified. The following discussion focuses on the continuity and thermodynamic equations. The momentum equation is not described. It is treated in the CCM2 version much the same as Ritchie (1990).

Continuity Equation

We adopt a hybrid vertical coordinate (η) defined by

$$p(\eta, p_s) = A(\eta)p_o + B(\eta)p_s \tag{1}$$

and consider first the continuity equation

---

* The National Center for Atmospheric Research is sponsored by the National Science Foundation.

$$\frac{\partial B}{\partial \eta}\left(\frac{\partial \ln p_s}{\partial t}+\mathbf{V}\cdot\nabla \ln p_s\right)=-\left(\frac{\partial p}{\partial \eta}\right)\frac{1}{p_s}\delta-\frac{1}{p_s}\frac{\partial}{\partial \eta}\left(\dot{\eta}\frac{\partial p}{\partial \eta}\right). \tag{2}$$

In Eulerian models this equation is generally applied in the form of integral equations for $\partial \ln p_s/\partial t$ and $\dot{\eta}$.

$$\frac{\partial \ln p_s}{\partial t}=-\int_{\eta_T}^{1}\frac{\partial B}{\partial \eta}\mathbf{V}\cdot\nabla \ln p_s d\eta-\int_{\eta_T}^{1}\frac{\partial p}{\partial \eta}\frac{1}{p_s}\delta d\eta \tag{3}$$

$$\frac{1}{p_s}\dot{\eta}\frac{\partial p}{\partial \eta}=-B(\eta)\frac{\partial \ln p_s}{\partial t}-\int_{\eta_T}^{\eta}\frac{\partial B}{\partial \eta}\mathbf{V}\cdot\nabla \ln p_s\, d\eta-\int_{\eta T}^{\eta}\frac{\partial p}{\partial \eta}\frac{1}{p_s}\delta\, d\eta \tag{4}$$

In the Eulerian CCM2, the integrals in (3) and (4) are approximated by discrete sums (Hack et al., 1992). In the formal development of Eulerian models, the integral forms (3) and (4) for the continuous equations are often derived first, then discrete approximations are applied. The same approximations, however, can often, as in the case of CCM2, be obtained by defining a discrete version of the continuity equation (2), then summing in the vertical. Or, stated another way, the discrete versions of (3) and (4) can be differenced to provide a discrete continuity equation.

The integral forms of the continuity equation (3) and (4) are not suitable for semi-Lagrangian development because the Lagrangian derivative is partially mixed in with the vertical integral. Thus we start with a discrete approximation to the original continuity equation (2). First, note that the left-hand-side includes horizontal advection only. Although it can be converted to a three dimensional advection operator since $\dot{\eta}\partial \ln p_s/\partial \eta = 0$, it is more convenient to treat it as horizontal advection only. In the traditional hybrid coordinate approach (Simmons and Strüfing, 1981), the coordinate functions B (and A) of (1) are defined only at discrete levels. Thus it is problematical to include terms such as ΔB in the vertical interpolations associated with a three-dimensional semi-Lagrangian operation.

The discrete semi-Lagrangian, semi-implicit continuity equation is

$$
\begin{aligned}
\Delta B_l \frac{(\ln p_{s_l})_A^{n+1} - (\ln p_{s_l})_{D_2}^{n-1}}{2\Delta t} &= -\frac{1}{2}\left\{ \left[\Delta_k \left(\frac{1}{p_s}\dot{\eta}\frac{\partial p}{\partial \eta}\right)_l\right]_A^{n+1} + \left[\Delta_k \left(\frac{1}{p_s}\dot{\eta}\frac{\partial p}{\partial \eta}\right)_l\right]_{D_2}^{n-1} \right\} \\
&\quad - \left(\frac{1}{p_s}\delta_l \Delta p_l\right)_{M_2}^n \\
&\quad - \left\{ \frac{1}{2}\left[\left(\frac{1}{p_s^r}\delta_l \Delta p_l^r\right)_A^{n+1} + \left(\frac{1}{p_s^r}\delta_l \Delta p_l^r\right)_{D_2}^{n-1}\right] - \left(\frac{1}{p_s^r}\delta_l \Delta p_l^r\right)_{M_2}^n \right\}
\end{aligned} \tag{5}
$$

where

$$
\Delta_k(\quad)_l = (\quad)_{l+\frac{1}{2}} - (\quad)_{l-\frac{1}{2}}
$$

denotes a vertical difference and A denotes the arrival point, D_2 the departure point from horizontal (2 dimensional) advection, M_2 the midpoint of that trajectory, and l denotes the vertical level. Equation (5) is similar to the σ system forms chosen by Ritchie (1991), McDonald and Haugen (1992), and Bates et al. (1992), although McDonald and Haugen (1992) and Bates et al. (1992) included some decentering to stabilize their two time level approach, and Ritchie (1991) adopted three-dimensional advection. The subtleties associated with the discrete η system mentioned above do not arise in the σ system. In addition, the divergence term is linear in the σ system, unlike the η system. Thus (5) includes divergence terms centered on the trajectory, which arise from the linearization for the semi-implicit approximations.

The surface pressure forecast equation is obtained by summing over all levels

$$
\begin{aligned}
(\ln p_s)_A^{n+1} &= \sum_{l=1}^{K} \Delta B_l (\ln p_{s_l})_{D_2}^{n-1} \\
&\quad - \Delta t \sum_{l=1}^{K} \left[\Delta_k \left(\frac{1}{p_s}\dot{\eta}\frac{\partial p}{\partial \eta}\right)_l\right]_{D_2}^{n-1} \\
&\quad - 2\Delta t \sum_{l=1}^{K} \left(\frac{1}{p_s}\delta_l \Delta p_l\right)_{M_2}^n \\
&\quad - 2\Delta t \sum_{l=1}^{K} \frac{1}{p_s^r}\left\{\frac{1}{2}\left[(\delta_l)_A^{n+1} + (\delta_l)_{D_2}^{n-1}\right] - (\delta_l)_{M_2}^n\right\}\Delta p_l^r
\end{aligned} \tag{6}
$$

The $(\ln p_s)^{n-1}$ term does not collapse to a single value as in the Eulerian case because the departure points are not necessarily aligned in the vertical, preventing the summation and departure point interpolations from commuting. The reference atmosphere terms p_s^r and Δp_l^r in the last (semi-implicit) sum do commute with the horizontal interpolation operators because they are a function of η only.

The equation for the vertical velocity is also obtained by summation of the continuity equation (5)

$$\begin{aligned}\left(\frac{1}{p_s}\dot{\eta}\frac{\partial p}{\partial \eta}\right)^{n+1}_{k+\frac{1}{2}} &= -\frac{1}{\Delta t}\left[B_{k+\frac{1}{2}}\left(\ln p_s\right)^{n+1}_{A} - \sum_{l=1}^{k}\Delta B_l \left(\ln p_{s_l}\right)^{n-1}_{D_2}\right] \\ &\quad - \sum_{l=1}^{k}\left[\Delta_k\left(\frac{1}{p_s}\dot{\eta}\frac{\partial p}{\partial \eta}\right)_l\right]^{n-1}_{D_2} - 2\sum_{l=1}^{k}\left(\frac{1}{p_s}\delta_l \Delta p_l\right)^{n}_{M_2} \\ &\quad - 2\sum_{l=1}^{k}\frac{1}{p_s^r}\left\{\frac{1}{2}\left[\left(\delta_l\right)^{n+1}_{A} + \left(\delta_l\right)^{n-1}_{D_2}\right] - \left(\delta_l\right)^{n}_{M_2}\right\}\Delta p_l^r\end{aligned} \tag{7}$$

We retain the semi-implicit structure of the continuity equation in the $\dot{\eta}$ equation. This is normally not done in Eulerian formulations although it could be. It provides greater discrete consistency while adding little to the complexity of the programming. McDonald and Haugen (1992) and Bates et al. (1992) adopt a similar equation for $\dot{\eta}$ (in their σ systems), but Ritchie (1991) uses an explicit approximation to the vertical integral form (4).

Thermodynamic Equation

The semi-implicit Eulerian thermodynamic equation in CCM2 from Hack, et al. (1992) is

$$\begin{aligned} \frac{T_k^{n+1} - T_k^{n-1}}{2\Delta t} + \mathbf{V}_k^n \cdot \nabla T_k^n + \dot{\eta}_k^n \left(\frac{\partial T}{\partial \eta}\right)_k^n = \frac{R(T_v)_k^n}{C_p^*} \left(\frac{\omega}{p}\right)_k^n \\ - \sum_{l=1}^{k} \frac{RT_k^r}{C_p} C_{kl}^r \left[\frac{1}{2}(\delta_l^{n+1} + \delta_l^{n-1}) - \delta_l^n\right] \Delta p_l^r \end{aligned} \tag{8}$$

The semi-implicit component (last sum on the right hand side) will be described shortly, but first we discuss the discrete approximations for ω.

The vertical velocity ω is related to $\ln p_s$ and $\dot{\eta}$ by

$$\frac{\omega}{p} = \frac{p_s}{p} \left[B(\eta)\left(\frac{\partial \ln p_s}{\partial t} + \mathbf{V} \cdot \nabla \ln p_s\right) + \frac{1}{p_s}\dot{\eta}\frac{\partial p}{\partial \eta}\right] \tag{9}$$

and by substitution of (4)

$$\frac{\omega}{p} = \frac{p_s}{p} \left[B(\eta)\mathbf{V} \cdot \nabla \ln p_s - \int_{\eta_T}^{\eta} \frac{\partial B}{\partial \eta} \mathbf{V} \cdot \nabla \ln p_s d\eta - \int_{\eta_T}^{\eta} \frac{\partial p}{\partial \eta} \frac{1}{p_s} \delta d\eta\right] \tag{10}$$

In the Eulerian CCM2, (10) is approximated in a general way by

$$\begin{aligned} \left(\frac{\omega}{p}\right)_k = \frac{B_k}{p_k} \mathbf{V}_k \cdot p_s \nabla \ln p_s \\ - \sum_{l=1}^{k} C_{kl} \left[\delta_l \Delta p_l + \mathbf{V}_l \cdot p_s \nabla \ln p_s \Delta B_l\right] \end{aligned} \tag{11}$$

The coefficients C_{kl} in the vertical sum are chosen to be energetically consistent with the pressure gradient in the momentum equations (Burridge and Haseler, 1977)

$$C_{kl} = \frac{H_{lk}}{\Delta p_k} \tag{12}$$

where H represents the coefficients in the vertical sum of the discrete hydrostatic equation

$$\Phi_k = \Phi_s + \mathrm{R}\sum_{l=k}^{K} \mathrm{H}_{kl}(p)\,\mathrm{T}_{v_l} \tag{13}$$

The relationship (12) ensures that in the discrete equations the conversion from potential to kinetic energy does not introduce a computational source or sink in the total energy.

In the Eulerian CCM2, the ω term on the right hand side of (8) is from (11) and the semi-implicit component (second term) includes the divergence component of (11) only, linearized about the reference atmosphere. Since the discrete form of ω was chosen independently of the continuity equation, it is not necessarily consistent, in the sense of (9), with the discrete continuity equation.

The discrete thermodynamic equation in the semi-Lagrangian version of CCM2 is

$$\begin{aligned}\frac{T_A^{n+1} - T_D^{n-1}}{2\Delta t} &= \left(\frac{RT_v}{C_p^*}\frac{\omega}{p}\right)_M^n \\ &\quad + \frac{RT^r}{C_p}\frac{p_s^r}{p^r}\left[B(\eta)\frac{d_2 \ln p_s}{dt} + \overline{\left(\frac{1}{p_s}\dot{\eta}\frac{\partial p}{\partial \eta}\right)}^t\right] \\ &\quad - \frac{RT^r}{C_p}\frac{p_s^r}{p^r}\left[\left(\frac{p}{p_s}\right)\left(\frac{\omega}{p}\right)\right]_M^n\end{aligned} \tag{14}$$

where

$$\frac{d_2 \ln p_s}{dt} = \frac{(\ln p_s)_A^{n+1} - (\ln p_s)_{D_2}^{n-1}}{2\Delta t} \tag{15}$$

and

$$\overline{(\quad)}^t = \frac{1}{2}[(\quad)_A^{n+1} + (\quad)_D^{n-1}] \tag{16}$$

This form is based on (9) for ω and both $d_2 \ln p_s/dt$ and $\dot{\eta}$ are treated in a semi-Lagrangian, semi-implicit fashion rather than just the semi-implicit divergence component in (8). However, care is needed to ensure that the explicit component of ω in (14) is also consistent with the continuity equation. This can be done by defining ω as an explicit vertical sum, which is consistent with the discrete continuity equation,

$$\left(\frac{\omega}{p}\right)_k = \frac{p_s}{p_k}\left\{ B_k \mathbf{V}_k \cdot \nabla \ln p_s - \sum_{l=1}^{k} \gamma_{kl} \left[\frac{1}{p_s} \delta_l \Delta p_l + \mathbf{V}_l \cdot \nabla \ln p_s \Delta B_l \right] \right\} \qquad (17)$$

and has the same form as (11) but not necessarily the same coefficients C_{kl}, or by defining it directly from $\dot{\eta}$ and δ by eliminating $d_2 \ln p_s / dt$ from (9)

$$\left(\frac{\omega}{p}\right)_k = \frac{p_s}{p_k}\left\{ \left(\frac{1}{p_s} \frac{\partial p}{\partial \eta} \dot{\eta} \right)_k - \frac{B_k}{\Delta B_k} \left[\frac{1}{p_s} \delta_k \Delta p_k + \Delta_k \left(\frac{1}{p_s} \dot{\eta} \frac{\partial p}{\partial \eta} \right)_k \right] \right\} \qquad (18)$$

Ritchie (1991) adopts a form similar to (14) for his σ system thermodynamic equation with the ω in the nonlinear term from an integral (17) form. McDonald and Haugen (1992) and Bates et al. (1992) both combine the (three dimensional) Lagrangian $\ln p_s$ derivative (with linear coefficient) with the Lagrangian temperature derivative to write a forecast equation for the combination. This seems to introduce an inconsistency in the way $\ln p_s$ is treated since it is 3-dimensional in the thermodynamic equation and 2-dimensional in the continuity equation. Both use the form (18) for the explicit ω component.

Modifications to CCM2 for consistency

As was mentioned in the introduction, the goal of this development was to obtain a semi-Lagrangian version of CCM2 that differed from the Eulerian version only in the advection approximations. In addition, we desire consistency between ω in the energy conversion term and the discrete continuity equation as well as the pressure gradient. Thus we first modify the Eulerian version to have this consistency and illustrate the effect that these changes have on the simulated climate.

In CCM2, the discrete hydrostatic equation (13) and the discrete form of the continuity equation integrals (3) and (4) were chosen first, independently of each other. The coefficients for the integral in ω (11) were chosen for energy consistency (12). Thus, the discrete ω is not derivable from the discrete $\partial \ln p_s / \partial t$ and $\dot{\eta}$ equations. This approach has been adopted in Eulerian models for some time (e.g. ECMWF, Burridge and Haseler, 1977; and CCM1, Williamson et al., 1987). Since energy consistency is desirable, one might ask, given the discrete ω equation, is there a consistent discrete continuity equation? The answer is no with the CCM2 form. Given the discrete ω, the inverse problem for $\dot{\eta}$ and $\partial \ln p_s / \partial t$ is singular, in part because of the vertically staggered grid.

One can solve the problem the other way around. Given the discrete continuity equation of CCM2, there is a discrete ω equation which is consistent with it. This is most easily found if the vertical level interfaces and mid-levels are related by

$$B_k = \frac{1}{2}\left(B_{k+\frac{1}{2}} + B_{k-\frac{1}{2}}\right) \tag{19}$$

and similarly for the As. This form, however, relinquishes a priori energy conservation associated with the conversion process. Results from this form, in which the mid-levels are defined from the interfaces by (19), are labeled MOD1 in the figures which follow. We also consider a second modification to the Eulerian CCM2 to regain energy conservation. As above, the continuity equation is chosen first and the ω equation is chosen to be consistent with it. Then the hydrostatic matrix (13) is chosen to be consistent with ω by inverting (12) for H_{kl}. Results from simulations with this form are labeled MOD2 in the figures. Results are presented from two versions since the original grid levels of CCM2 do not satisfy (19). In the first, the mid layers are redefined from the interfaces to satisfy (19). This has the shortcoming that levels at which the atmospheric state is defined are changed. In the second version, the layer interfaces are redefined from the mid-levels to satisfy

$$B_{k-\frac{1}{2}} = 2B_k - B_{k+\frac{1}{2}} \tag{20}$$

working up from the surface.

Figure 1 presents the January average, zonal average temperature from CCM2 and differences (MOD-CCM2) of the modified versions with CCM2. The contour interval is 5.0K for the temperature and 0.5K for the differences. Poleward of 30° latitude the differences are within the natural variability of one January from another and cannot be considered significant. The differences in the structure at and above the tropopause are likely to be significant as are the differences in the mid and upper tropical troposphere in the two panels on the left. Nevertheless, these differences are small compared to the differences made when the physical parameterizations are changed and/or tuned.

Conservation Aspects

The semi-Lagrangian method as applied today, with interpolation for pointwise values, is not a priori conservative. Our earlier experience with water vapor illustrated that a "fixer" to ensure conservation was convenient, especially since it had no significant interaction with the physical parameterizations and did not affect the overall simulation (Rasch and Williamson, 1991; Williamson and Rasch, 1992). Without the "fixer", the parameterized sources and sinks compensated for the "computational" water vapor source so that all fields remained reasonable. That may not be the case for atmospheric mass since the model contains no parameterized physical sources and sinks. The mass could drift enough in long simulations that the mean pressure error could begin to seriously affect the simulation. Therefore, in the CCM2 (Eulerian and semi-Lagrangian versions), we apply fixers to guarantee conservation of both the dry mass of the atmosphere and the water vapor of the atmosphere.

The discrete conservation relations for the dry mass and water vapor are

$$\int_2 p_s^{n+1} - \int_3 q^{n+1}\Delta p^{n+1} = \int_2 p_s^{n-1} - \int_3 q^{n-1}\Delta p^{n-1} = \mathbf{P} \tag{21}$$

$$\int_3 q^{n+1}\Delta p^{n+1} = \int_3 \left(q^{n-1} + S\right)\Delta p^{n-1} \tag{22}$$

where, since p is given by (1), Δp is given by

$$\Delta p = \Delta A p_o + \Delta B p_s \tag{23}$$

and S includes the water vapor sources and sinks this time step. The horizontal integral $\int_2$ denotes the normal Gaussian quadrature approximation of spectral models and the three dimensional integral $\int_3$ includes a vertical sum over the grid as well. (The mass weighting is taken care of by the Δp already included in the equations.) We choose to modify the masses in the following way:

$$p_s^{n+1}(\lambda,\phi) = M p_s^+(\lambda,\phi) \tag{24}$$

$$q^{n+1}(\lambda,\phi,\eta) = q^+ + \alpha q^+ \left| q^+ - \left(q^{n-1} + S\right) \right|^{\beta} \tag{25}$$

where the superscript + denotes the provisional values following the application of the numerical approximations and β is chosen to be 3/2. The form (24) is chosen so that $\nabla \ln p_s$ is not changed. The gradient is the important dynamical quantity and it is undesirable to change it for arbitrary reasons. The form (25) is chosen so that the changes to the water vapor are small in the regions where the water vapor itself is small and where the advection made a small change to the water vapor. Substitution of (24) and (25) into (21) and (22) yields

$$M = \left[\mathbf{P} + \int_3 \left(q^{n-1} + S\right) \Delta p^{n-1} \right] \Big/ \int_2 p_s^+ \tag{26}$$

$$\alpha = \frac{\int_3 \left(q^{n-1} + S\right) \Delta p^{n-1} - \int_3 q^+ \Delta p^{n+1}}{\int_3 q^+ \left| q^+ - \left(q^{n-1} + S\right) \right|^{\beta} \Delta p^{n+1}} \tag{27}$$

Table 1 presents the average and standard deviation of the absolute value of the dry mass correction from several T42, 18 level simulations. The statistics are calculated for January from simulations starting September 1 and are in units of Pa per time step. "CCM2" denotes the MOD2 Eulerian version described above, with the interfaces defined by (20). "CCM2 FORM" denotes its semi-Lagrangian variant and "ECMWF Form" denotes a model based on my interpretation of the approximations to the continuity equation and conversion term in the ECMWF semi-Lagrangian model, but with the levels as in CCM2 and the H and C matrices as in the original CCM2 rather than as defined in the ECMWF model. Thus, this is, in fact, very different from the ECMWF model itself and the label is adopted for convenience only. The characteristics of simulations with the ECMWF model may be very different from those reported here. All experiments were run with a 20 minute time step to ensure the physical parameterizations were unaffected in any primary way.

Table 1

$|\Delta \text{Mass}|$ $(Pa/\Delta t)$

CCM2	ECMWF FORM	CCM2 FORM
.006±.004	.08±.04	.15 ± .09

Energy conservation is also important for climate models. We currently make no correction to the total energy as it is observed to be conserved in the model to an adequate degree. The conserved quantity is the integral of

$$\mathrm{TE} = \frac{1}{g}\left[C_p^* T + \Phi_s + \frac{1}{2}\left(u^2 + v^2\right)\right] \tag{28}$$

If we denote the temperature source/sink as Q^n and the momentum as (F_u^n, F_v^n), then the residual (non conserved) energy over a time step is

$$\begin{aligned} \mathrm{R} = \int_3 \Big\{ & \mathrm{TE}^{n+1}\Delta p^{n+1} - \mathrm{TE}^{n-1}\Delta p^{n-1} \\ & - 2\Delta t \frac{C_p^*}{g}(Q)^n \Delta p^n - 2\Delta t \frac{1}{g}\left(uF_u^n + vF_v^n\right)\Delta p^n \Big\} \end{aligned} \tag{29}$$

Table 2 summarizes the January statistics for the three experiments described above in Table 1. The values are the average and standard deviation of the absolute value of the residual over a time step converted to units of W/m^2. As can be seen, the semi-Lagrangian versions conserve better than the Eulerian does.

Table 2

$|\frac{\Delta \mathrm{TE}}{\Delta t}| \qquad (W/m^2)$

CCM2	ECMWF FORM	CCM2 FORM
.98±.13	.36±.13	.24 ± .11

Comparison of semi-Lagrangian and Eulerian simulations

Figure 2 shows differences in the January average, zonal average temperature for semi-Lagrangian simulations minus Eulerian. The contour interval is 1.0K. All simulations in this section use a 20 minute time step so that the physical parameterizations are unaffected. The time step is a fundamental aspect of some of the physical parameterizations, and changing it can make differences in the behavior of those parameterizations. Semi-Lagrangian simulations with longer time steps will be discussed in the next section. The top row of Figure 2 has differences with the Eulerian version labeled MOD2 described above, and the bottom row has differences with the original unmodified Eulerian CCM2. The left column has differences from the semi-Lagrangian version of CCM2 and the right column has differences from the ECMWF form of approximations. Both of these semi-Lagrangian versions are described more clearly in the previous section. All averages in Figure 2 are for a single month.

Most of the differences poleward of 30° cannot be said to be significant. To illustrate the natural variability, Figure 3 contains differences of four individual Januaries chosen from a 20 year control simulation with the Eulerian CCM2 from the 20 year average of that control simulation. The contour interval is 0.5K. Note that the contour intervals in Figures 2 and 3 are chosen to allow a meaningful visual impression or comparison between the two figures. Recall, Figure 2 shows differences of a single January with a single January, while Figure 3 shows differences of a single January with the 20 year average January, thus a ratio of 2 to 1 for the contour interval is reasonable.

Referring back to Figure 2, the differences at and above the tropical tropopause are likely to be significant, with the semi-Lagrangian forms both being colder than the Eulerian. This difference is in the opposite sense than that which would be expected from smoothing introduced by the semi-Lagrangian vertical interpolations (Ritchie, 1991). It is likely to be attributable to the physical parameterizations (in particular, convection) working differently in response to a changed vertical advection. The other significant difference noticeable in Figure 2 is the colder upper tropical troposphere with the ECMWF form resulting in a slightly less stable tropical tropopause. In addition, the colder southern hemisphere mid-latitude troposphere (40S) is probably significant. No differences of individual months with the 20 year average show such large differences. The differences chosen for Figure 3 are typical.

Figure 4 shows the difference in water vapor mixing ratio for semi-Lagrangian minus Eulerian simulations in the same format as Figure 2. The contour interval is 0.2g/kg. Figure 5 shows differences of individual Januaries with the 20 year ensemble average from the Eulerian CCM2 with a contour interval of 0.1g/kg. The variability between individual Januaries (Figure 5) is primarily vertically oriented and associated with movement of, and changes in the strength of, the Hadley cell from year to year. The differences between CCM2 form of semi-Lagrangian and Eulerian (left column, Figure 4) appear to be within the natural variability. The ECMWF form produces a drier troposphere equatorward of 40° latitude. The difference is probably significant, as it is of broader scale than that of the banded structure associated with movement of the Hadley cell. It is also consistent with the colder troposphere seen in Figure 2. Concerning the colder tropopause seen in Figure 2, we speculate that the semi-Lagrangian vertical advection, which is formally more accurate, transports more moisture and heat vertically in the lower troposphere, and as a result, the convection is slightly less active, producing differences further up. Whatever the actual cause, the differences in Figures 2 and 4 associated with the different numerical approximations are smaller than those encountered with different physical parameterizations or even with tuning a given parameterization. Semi-Lagrangian advection certainly seems to be a suitable basis for climate models.

Semi-Lagrangian simulations with different time steps

Figure 6 (top left panel) shows the difference in January average, zonal average temperature from a semi-Lagrangian simulation with 30 minute time step minus the one with a 20 minute time step discussed in the preceeding section. The contour interval in all panels of Figure 6 is 1.0K. The simulation with a 30 minute time step is warmer around and above the tropical tropopause. This difference is of opposite sign to that in the preceeding section. Figure 6 also shows differences from some other formulations of the semi-Lagrangian version. The treatment of the centered terms on the trajectory in the continuity and thermodynamic equations is somewhat arbitrary. The upper right panel shows the time step sensitivity in January averages to replacing the trajectory mid point terms $(\ )^n_M$ with spatial averages along the trajectory $\frac{1}{2}\,[(\ )^n_A + (\ )^n_D]$. This form is labeled "CENTERED". A slight variant which introduces some damping by weighting the value at the arrival point slightly more, $\frac{1}{2}\,[(1+\epsilon)\ (\ )^n_A + (1-\epsilon)\ (\ )^n_D]$, is labeled "OFF-CENTERED". This type of off-centering is adopted by McDonald and Haugen (1992) and Bates et al. (1992) to stabilize their two time level schemes (Gravel et al., 1992). The centered form shows the same sensitivity to time step as the original "CCM2 FORM". The sensitivity of the zonal average to the placement of the centered terms on the trajectory (bottom row of Figure 6) is rather minor. The simulations discussed in this section started January 1 and thus the January average does not represent a climatological balance. These differences should be considered as indicating a trend rather than the final climatology.

Conclusions

The semi-Lagrangian, semi-implicit formulation for atmospheric models is viable for climate simulation. Although the approach is not a priori mass and energy conservative, mass fixers can be applied to correct the deficiencies each time step with no detrimental effect on the simulations. We showed elsewhere (Rasch and Williamson, 1991; Williamson and Rasch, 1992) that the water vapor fixer appears to be cosmetic. The simulations described in the current paper indicate that the atmospheric mass fixer seems to be cosmetic as well, as the semi-Lagrangian simulations differ from Eulerian in only very minor ways. Energy, on the other hand, is conserved better in the semi-Lagrangian simulations than in the Eulerian.

The change from Eulerian to semi-Lagrangian advection has only a small effect on the simulated climate. Similarly, changing from a 20 to a 30 minute time step (in the T42 model) also has only a small effect. Both changes are smaller than the changes introduced by varying horizontal or vertical resolution, by introducing different physical parameterizations, or by "tuning" parameterizations in a given suite of parameterizations. Thus a suitable development strategy would be to choose the resolution, semi-Lagrangian approximations, and time step practical for the application model, then to retune the physical parmeterizations to yield the desired simulation.

Acknowledgements

I would like to thank Jerry Olson for developing the code for the semi-Lagrangian version of CCM2, Rüdiger Jakob and James Hack for comments on the original draft, and Janet Rodina for typing the manuscript. This work was partially supported by the DOE CHAMMP Program.

References

Burridge, D.M. and J. Haseler, 1977: A model for medium range weather forecasting-adiabatic formulation. ECMWF Tech. Rep. No. 4, 46pp.

Bates, J.R., S. Moorthi, and R.W. Higgins, 1992: A global multilevel atmospheric model using a vecto semi-Lagrangian finite difference scheme. Part I: Adiabatic formulation. *Mon. Wea. Rev.*, submitted.

Gravel, S., A. Staniforth, and J. Côté, 1992: A stability analysis of a family of baroclinic semi-Lagrangian forecast models. *Mon. Wea. Rev.*, submitted.

Hack, J.J., B.A. Boville, B.P. Briegleb, J.T. Kiehl, P.J. Rasch, and D.L. Williamson, 1992: A description of the NCAR Community Climate Model (CCM2). NCAR Tech. Note No. 382+STR, in preparation.

McDonald, A., and J. Haugen, 1992: A two-time-level, three-dimensional semi-Lagrangian, semi-implicit, limited-area grid point model of the primitive equations. *Mon. Wea. Rev.*, **120**, 2603-2621.

Rasch, P.J., and D.L. Williamson, 1991: The sensitivity of a General Circulation Model Climate to the Moisture Transport Formulation. *J. Geophys. Res.*, **96**, 13,123-13,137.

Simmons, A.J., and R. Strüfing, 1981: An energy and angular-momentum conserving finite-difference scheme, hybrid coorinates and medium-range weather prediction. ECMWF Tech. Rep. No. 28, 68pp.

Ritchie, H., 1990: Application of the semi-Lagrangian method to a multilevel spectral primitive-equations model. *Quart. J. Roy. Meteor. Soc.*, **117**, 91-106.

Williamson, D.L., J.T. Kiehl, V. Ramanathan, R.E. Dickinson, and J.J. Hack, 1987: Description of NCAR Community Climate Model (CCM1). NCAR Tech. Note No. 285+STR, pp.112.

Williamson, D.L., and P.J. Rasch, 1992: Water vapor transport in the NCAR CCM2. *Tellus*, submitted.

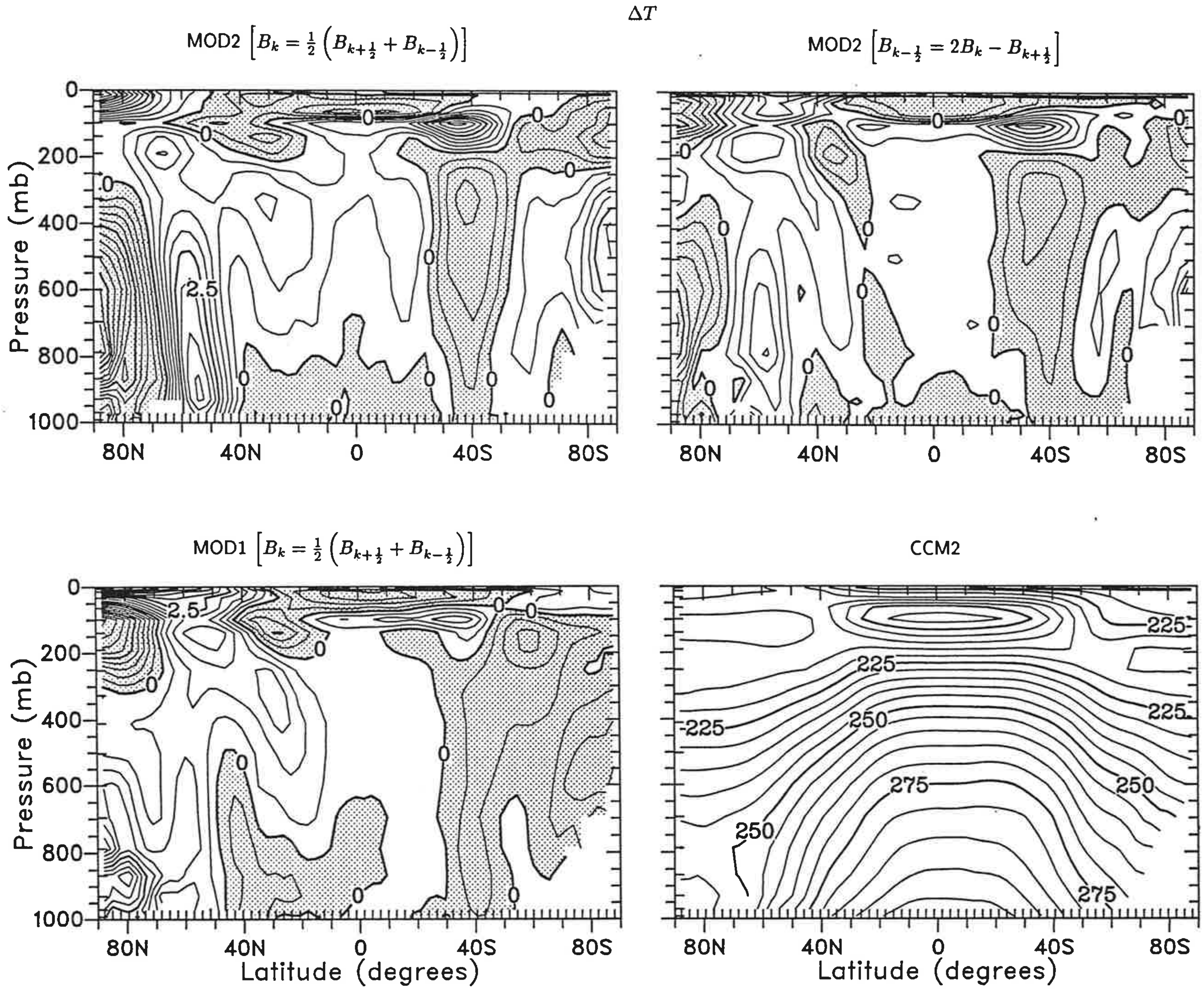

ΔT

MOD2 $\left[B_k = \frac{1}{2}\left(B_{k+\frac{1}{2}} + B_{k-\frac{1}{2}}\right)\right]$

MOD2 $\left[B_{k-\frac{1}{2}} = 2B_k - B_{k+\frac{1}{2}}\right]$

MOD1 $\left[B_k = \frac{1}{2}\left(B_{k+\frac{1}{2}} + B_{k-\frac{1}{2}}\right)\right]$

CCM2

Figure 1

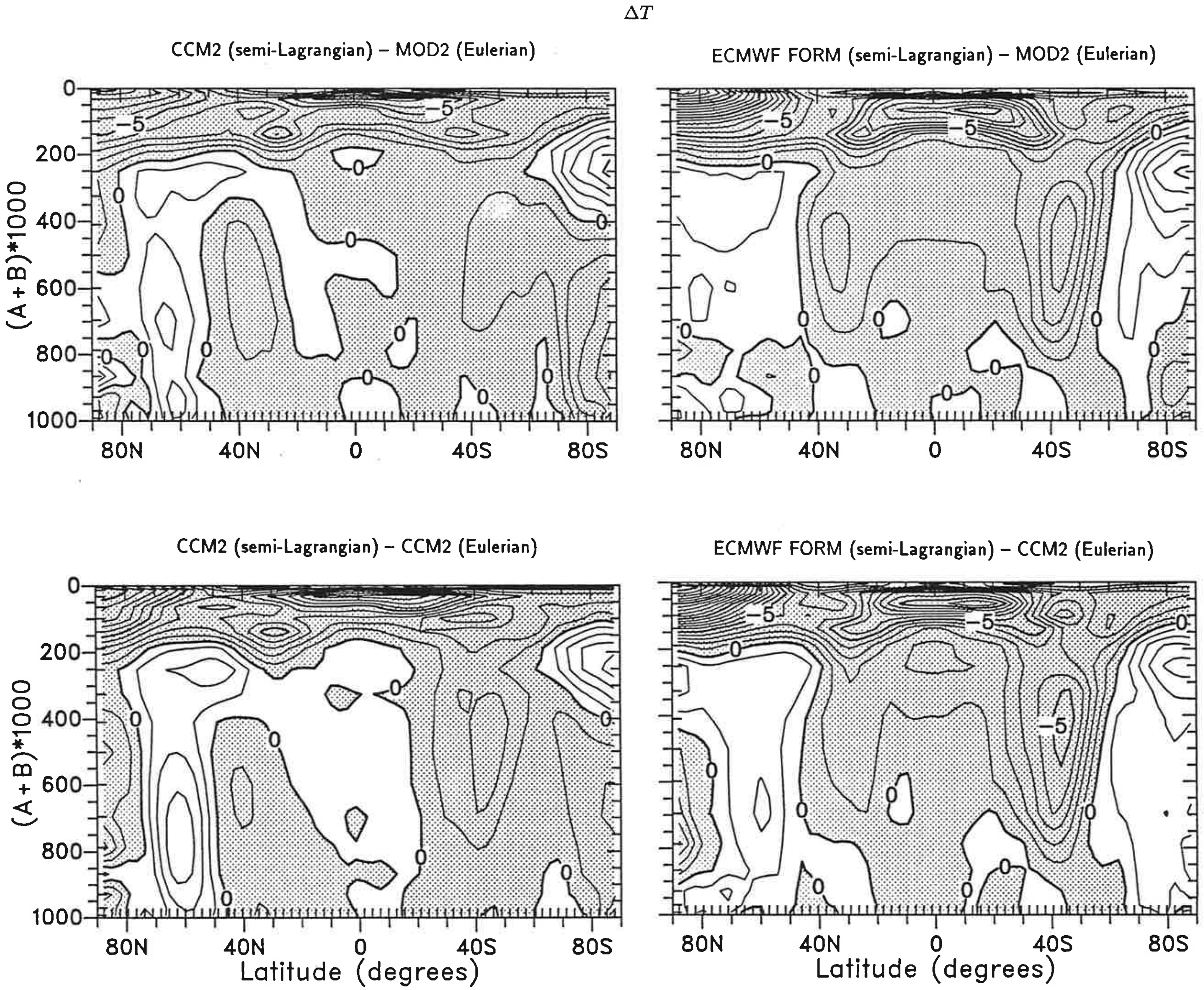
ΔT
CCM2 (semi-Lagrangian) – MOD2 (Eulerian)
ECMWF FORM (semi-Lagrangian) – MOD2 (Eulerian)
CCM2 (semi-Lagrangian) – CCM2 (Eulerian)
ECMWF FORM (semi-Lagrangian) – CCM2 (Eulerian)
(A+B)*1000
0
200
400
600
800
1000
80N
40N
0
40S
80S
Latitude (degrees)
-5
0

Figure 2

ΔT

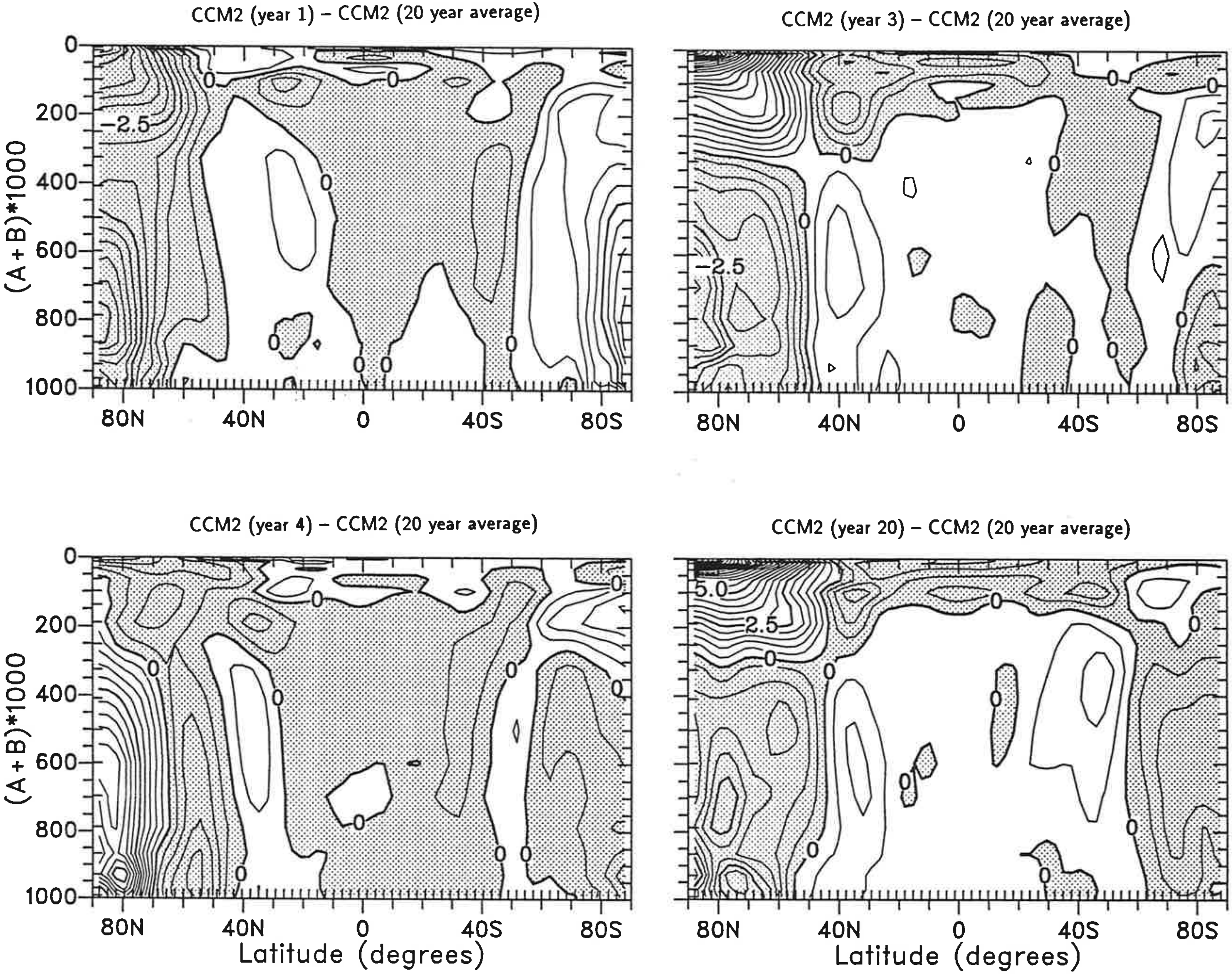

Figure 3

Δq

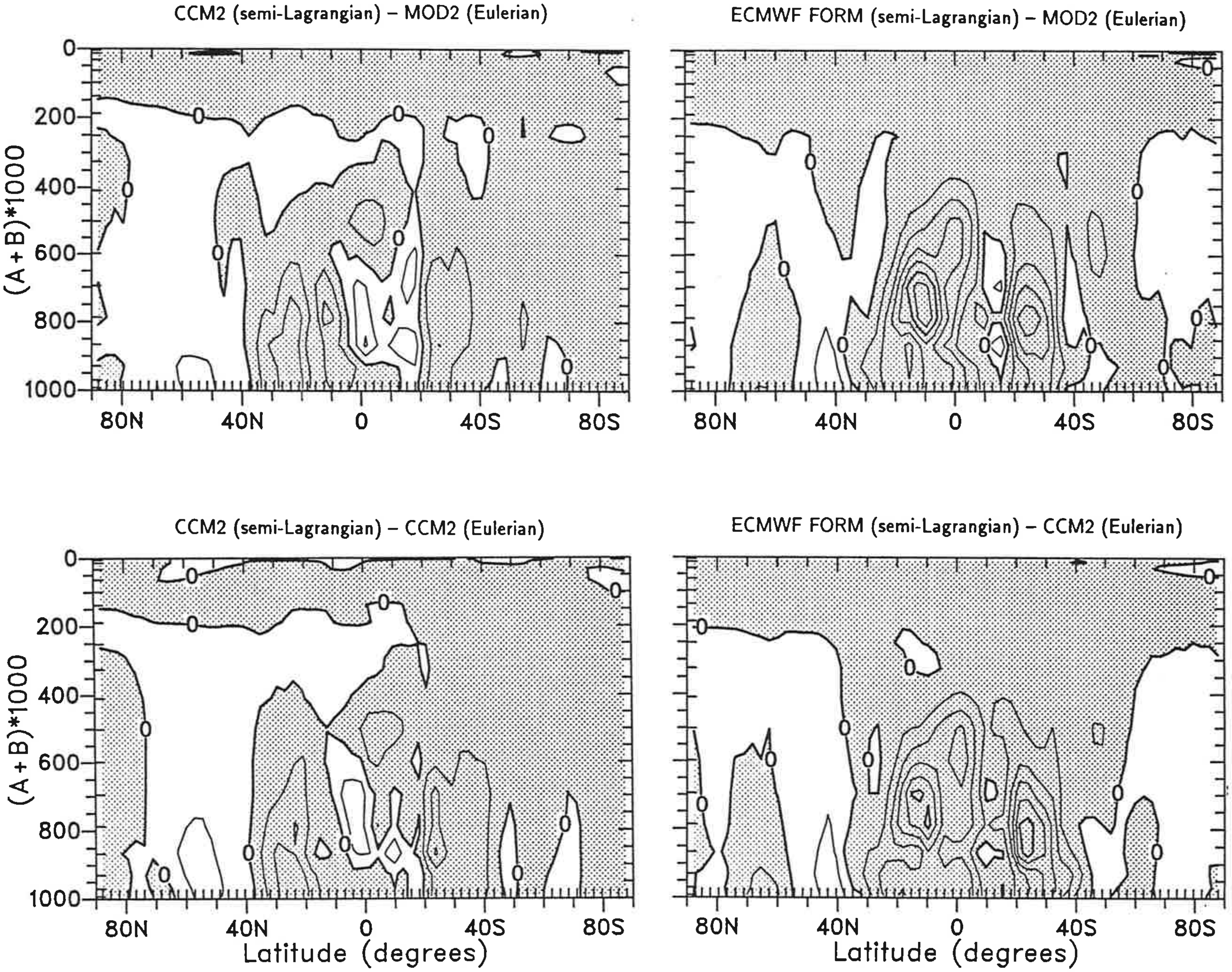

Figure 4

Δq

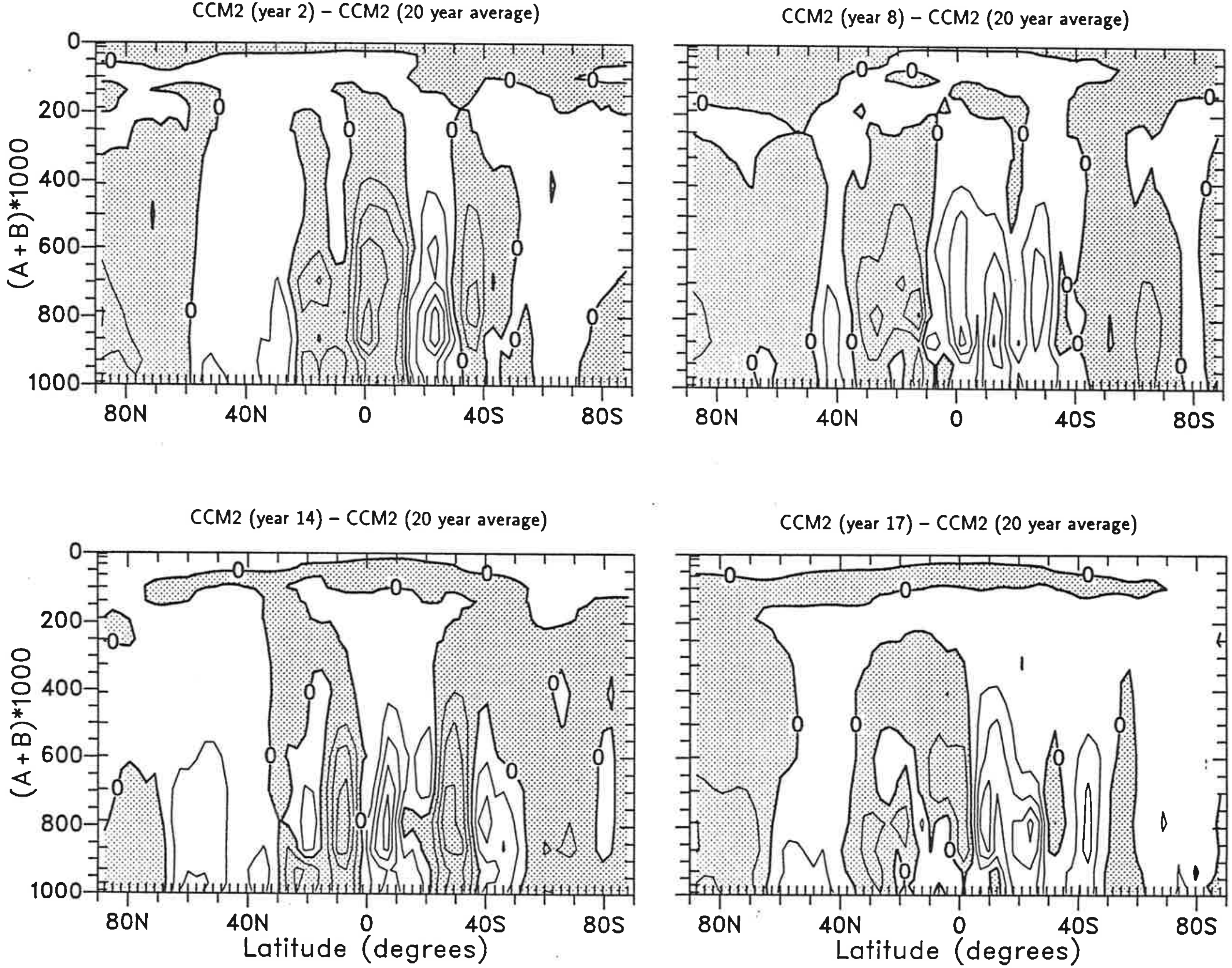

Figure 5

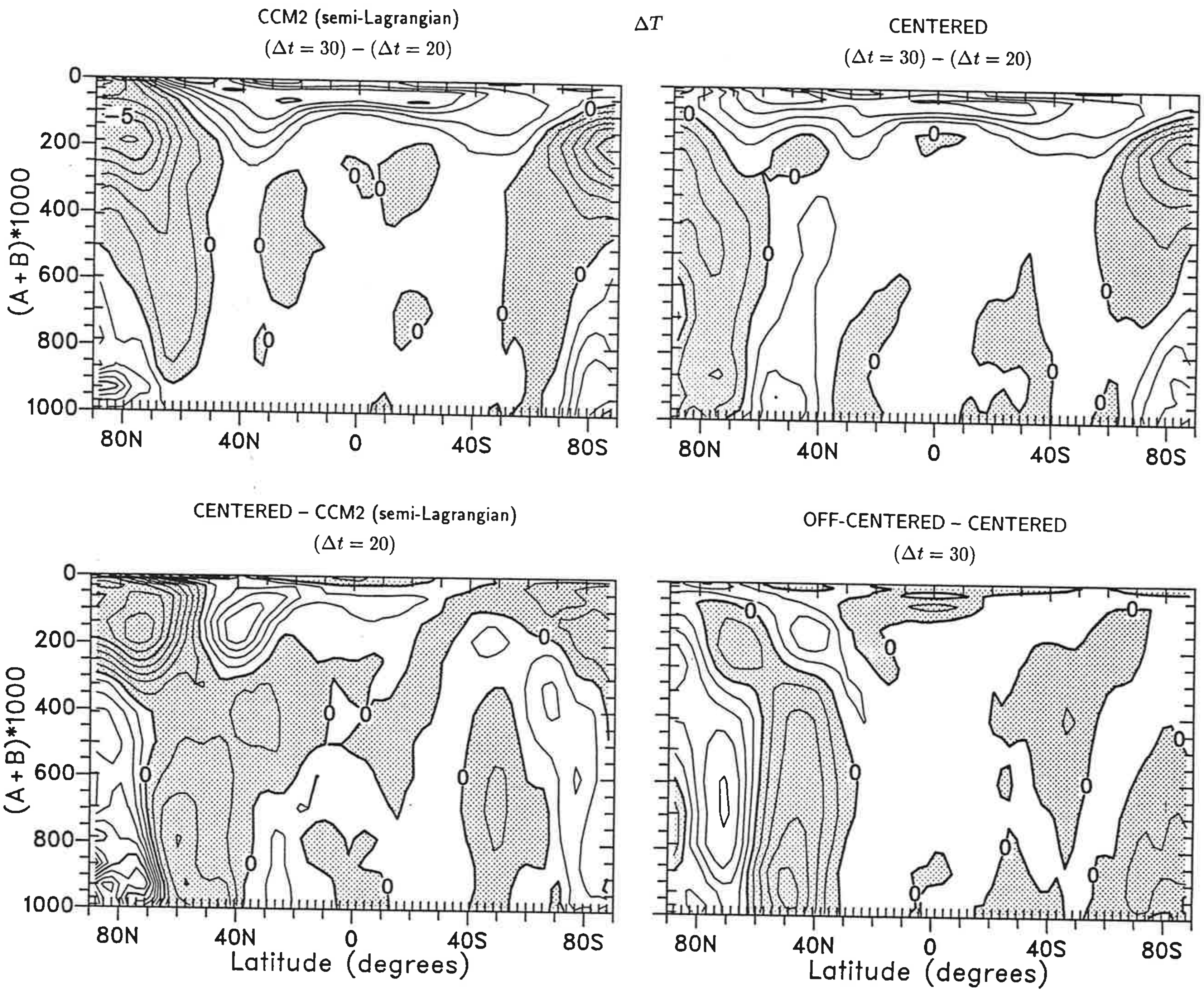

ΔT

CCM2 (semi-Lagrangian)
$(\Delta t = 30) - (\Delta t = 20)$

CENTERED
$(\Delta t = 30) - (\Delta t = 20)$

CENTERED – CCM2 (semi-Lagrangian)
$(\Delta t = 20)$

OFF-CENTERED – CENTERED
$(\Delta t = 30)$

Figure 6

A Note on

A MASS -, ENERGY- AND ENTROPHY CONSERVING SEMI-LAGRANGIAN AND EXPLICIT INTEGRATION SCHEME FOR THE PRIMITIVE METEOROLOGICAL EQUATIONS

Bennert Machenhauer

Max-Planck-Institute for Meteorology
Hamburg, Germany

Hamburg, October 1992

1. Introduction

For climate simulations especially mass and energy conservation are important properties of a numerical model. Eularian Semi-implicit spectral models as the former operational ECMWF model conserve these quantities relatively well. Concerning mass conservation we performed a 120 day test integration with this ECMWF model in T63 resolution. It resulted in a slight increase of mass corresponding to less than 1 hPa in the global mean surface pressure. A similar integration with the new ECMWF semi-Lagrangian Semi-implicit model resulted, however, in a systematic loss of mass corresponding to 4.5 hPa in 120 days. Two different "mass-fix" procedures were tried in semi-Lagrangian integrations. In these the global mean surface pressure $\overline{p_s}$ or $\overline{lnp_s}$ were corrected after each time step. As expected the changes in total mass over 120 day integrations were eliminated, or almost so, when these schemes were applied. Such corrections are insatisfactory, however, because mass which is added or subtracted in each time step is evenly distributed over the globe and not added or subtracted at the right geographical positions.

In the test integrations there were no signs of improvement when the mass-fix procedures were applied, except for the mass conservation. Assuming that the Eulerian integration is the most correct one we could have hoped that the differences between the integration results of the semi Lagrangian and the Eulerian model were reduced when the mass-fix procedures were applied in the former model. This was not the case in the present test integrations. The mass-fix procedures were found to introduce changes in the time mean fields, in particular in the fields of accumulated precipitation, which were as big as the differences between the Eulerian and the uncorrected semi-Lagrangian fields. At many locations the differences to the Eulerian results were increased by the mass-fix procedures. Thus the application of such simple correction schemes seems not to be the proper way to fix a non-conservation property of a model. Still mass-fix procedures are widely used also in long Eulerian integrations, at least at MPI, without any other justification than an improved mass conservation.

It seems desirable to develop models, especially semi-Lagrangian models, with improved conservation properties. If possible this should be achived without loss of "local" accuracy. In the present note a new three time level semi-Lagrangian PE model formulation is suggested which under certain conditions will give exact conservation of total mass, total entropy and total energy. This new formulation has not jet been tested in practice so the intention of this note is to invite comments prior to such tests.

The idea is to use as prognostic equations Lagrangian forms of the continuity equations, the thermodynamic equation and the energy equation. To complete the system of prognostic equations in addition a special component of the momentum equation is used to predict changes in the wind direction. These equations are formulated for the volumes of air that are being advected in the horizontal wind field at time t and are ending up after each time step in the model grid volumes.

Trajectories are computed from the corner points of each grid area, $2\Delta t$ back in time, using horizontal velocities at a certain model level at time level t. These trajectories and the continuity equation are used to define the air volumes at time $t-\Delta t$ and t that are ending up in the grid volumes at time $t+\Delta t$. An explicit leapfrog time extrapolation scheme applied to the continuity, thermodynamic and energy equations must be absolutely stable since the total mass, entropy and energy with the formulation chosen can not increase over a $2\Delta t$ time step. Also a leap frog time extrapolation of the wind direction equation is expected to be stable since the Coriolis and the pressure gradient force, determined by the continuity, thermodynamic and energy equations, are bounded. Consequentely it is difficult to imagine how gravity oscillations could create unstable oscillations in the wind direction. Should such oscillations never the less turn out to develop in practice then an implicit scheme might be chosen for the wind direction equation.

Before the proposed new formulation for a full 3-D model is outlined in Section 3 we shall in the following Section 2 consider in more details the corresponding 1-D and 2-D shallow water model formulations. This will simplify the presentation of the basic ideas and the procedures proposed to be used in the full 3-D scheme. Furthermore the 1-D and 2-D formulations should be used in the first test experiments which must be carried out before the detailes of the 3-D scheme can be formulated.

Since this is a “Note” only we do not define carefully all notations used as we hope the reader will know the standard notations used.

2. Shallow water equation models

2.1 The 1-D case:

The momentum and continuity equations are

$$\frac{\partial u}{\partial t} + u\frac{\partial u}{\partial x} + g\frac{\partial h}{\partial x} = 0 \tag{1}$$

$$\frac{\partial h}{\partial t} + u\frac{\partial h}{\partial x} + h\frac{\partial u}{\partial x} = 0 \tag{2}$$

From these we easily obtain

$$\frac{\partial E}{\partial t} + \frac{\partial}{\partial x}(Eu + \frac{1}{2}gh^2u) = 0 \tag{3}$$

$$\frac{\partial h}{\partial t} + \frac{\partial}{\partial x}(hu) = 0 \tag{4}$$

where $E = \frac{1}{2}u^2h + \frac{1}{2}gh^2$.

For a periodic domain $0 \le x \le L$ (3) and (4) imply that.

$$\frac{d}{dt}\int_0^L E dx = 0 \tag{5}$$

$$\frac{d}{dt}\int_0^L h dx = 0 \tag{6}$$

which express conservation of total energy and mass, respectively (when multiplied by the constant density).

In order to obtain equations suitable for Lagrangian integration we write (3) and (4) in the forms

$$\frac{dE}{dt} + E\frac{\partial u}{\partial x} + \frac{\partial}{\partial x}(\frac{1}{2}gh^2u) = 0 \tag{7}$$

$$\frac{dh}{dt} + h\frac{\partial u}{\partial x} = 0 \tag{8}$$

and substitute in these the Eulerian expression for the divergence

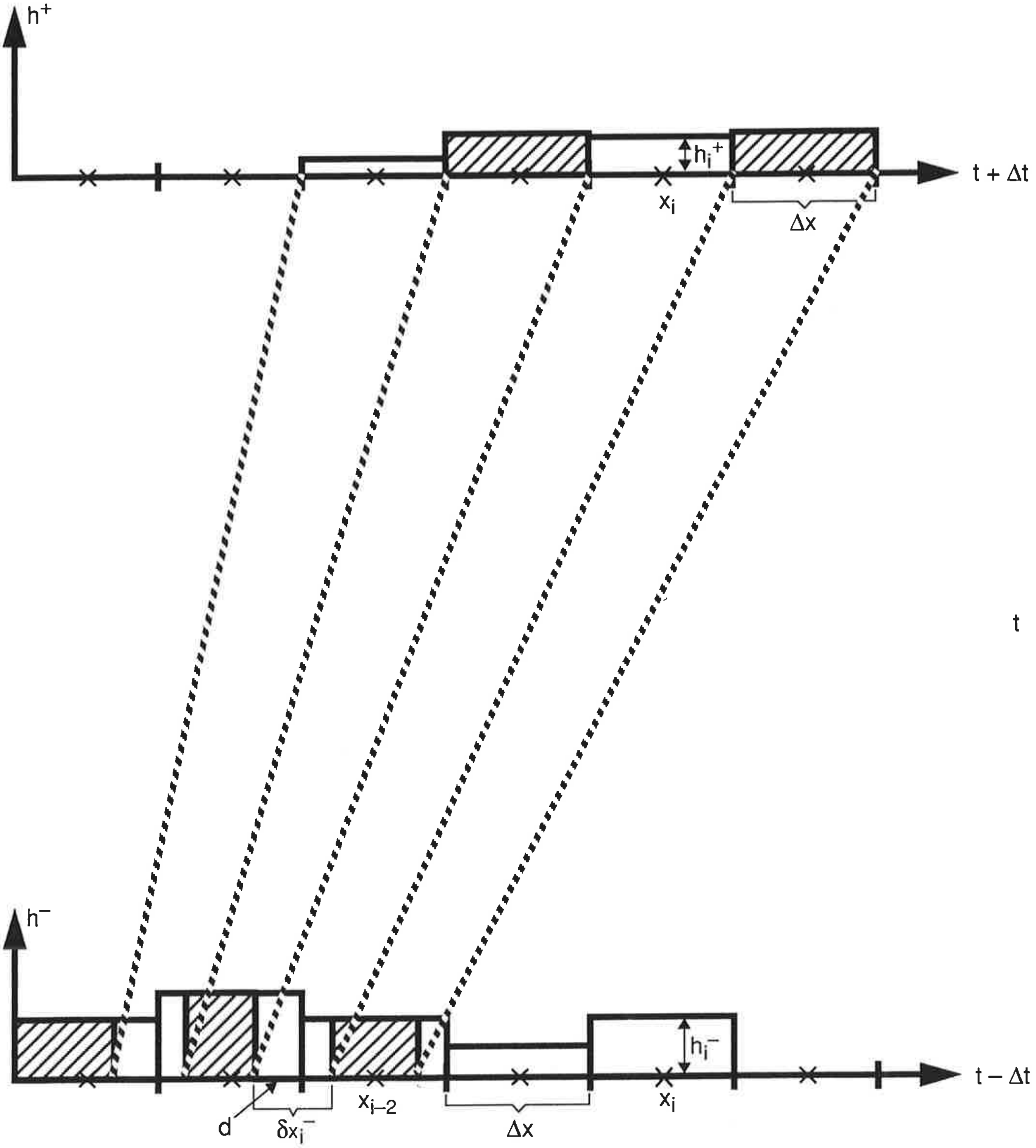

Fig. 1

$$\frac{\partial u}{\partial x} = \frac{1}{\delta x}\frac{d}{dt}(\delta x)\,, \tag{9}$$

where δx is an infinitesimal length interval.

We thereby get the equations that we shall use for Lagrangian integration:

$$\frac{d}{dt}(E\delta x) + \delta x\frac{\partial}{\partial x}(\frac{1}{2}gh^2u) = 0 \tag{10}$$

$$\frac{d}{dt}(h\delta x) = 0 \tag{11}$$

The discretization of these is based on trajectories that are ending up at time $t + \Delta t$ at the mid points between grid points and are computed from velocities at time t using the usual iterative procedure. Such trajectories are illustrated in Figure 1

We discretizise the continuity equation (11) as

$$h_i^{+}\ \Delta x = \overline{h_i^-}\ \delta x_i^- \tag{12}$$

where the index i refers to the arrival grid point and other notations are as indicated in the figure. For simplicity Δx is assumed constant. (It could be variable).

One way to obtain conservation of total mass is illustrated in the figure. The height h is assumed constant within each grid interval Δx and $\overline{h_i^-}$ is computed as a "length-weighted" mean over the interval δx_i^-. For the grid point x_i in the figure for instance

$$\delta x_i^-\ \overline{h_i^-} = (d\ h_{i-3}^- + (\delta x_i^- - d)\, h_{i-2}^-) \tag{13}$$

where d is a distance defined in the figure.

It is obvious that by this procedure we obtain that

$$\sum_i h_i^{+}\ \Delta x = \sum_i \overline{h_i^-}\ \delta x_i^- = \sum_i h_i^-\ \Delta x \tag{14}$$

which means exact conservation of total mass.

We discretizise the energy equation (10) as

$$E_i^+\,\Delta x = \overline{E_i^-}\,\delta x_i^- - g\Delta t\{(h^2u)_{i+1/2}-(h^2u)_{i-1/2}\}^o \tag{15}$$

Corresponding to the procedure used in the continuity equation we assume that u and h are constants within each grid interval Δx and we take for $\overline{E_i^-}$ the "length weighted" mean. Thus, for the case shown in the figure

$$\overline{E_i^-}\,\delta x_i = \frac{1}{2}\{d[(u_{i-3}^-)^2+gh_{i-3}^-]h_{i-3}^- + (\delta x_i^- - d)[(u_{i-2})^2+gh_{i-2}^-]h_{i-2}^-\} \tag{16}$$

The fluxes h^2u in the last term of (15) may be computed from their grid point values $(h^2u)_i = (h_i)^2u_i$ at time t by interpolations to the mid points of the trajectories.

By this procedure we obtain that

$$\sum_i E_i^+\,\Delta x = \sum_i \overline{E_i^-}\,\delta x_i^- = \sum_i E_i^-\,\Delta x \tag{17}$$

That is, exact conservation of total energy.

In each time step we compute at first h_i^+ using (12). To obtain u_i^+ we then use (15) which may be written

$$u_i^+ = \pm\sqrt{2G_i/h_i^+ - gh_i^+} \tag{18}$$

where G_i is the right hand side of (15) which depends only on values at time levels t and $t-\Delta t$.

We have to choose between the plus and minus sign in (18). Normally we choose the same sign as the "length-weighted" mean value of the momentum over the departure interval δx_i, which for the case shown in the figure is

$$\overline{(uh)_i^-}\,\delta x_i^- = d\,u_{i-3}^-h_{i-3}^- + (\delta x_i^- - d)\,u_{i-2}^-h_{i-2}^- \tag{19}$$

It may happen, however, that the radicant in (18) becomes negative which means that the kinetic energy at time $t+\Delta t$ becomes negative. This will happen in grid intervals for which $\overline{(1/2u^2h)_i^-}$ is small and the net flux at the boundaries of the grid interval of potential energy is sufficiently large.For such points the velocity of the air in the grid interval is assumed to become zero at a certain time during the time step and then it is assumed to be accelerated in the opposite direction during the rest of the time interval. This situation is illustrated in Figure 2 where we have assumed a linear variation of E_{kin}.

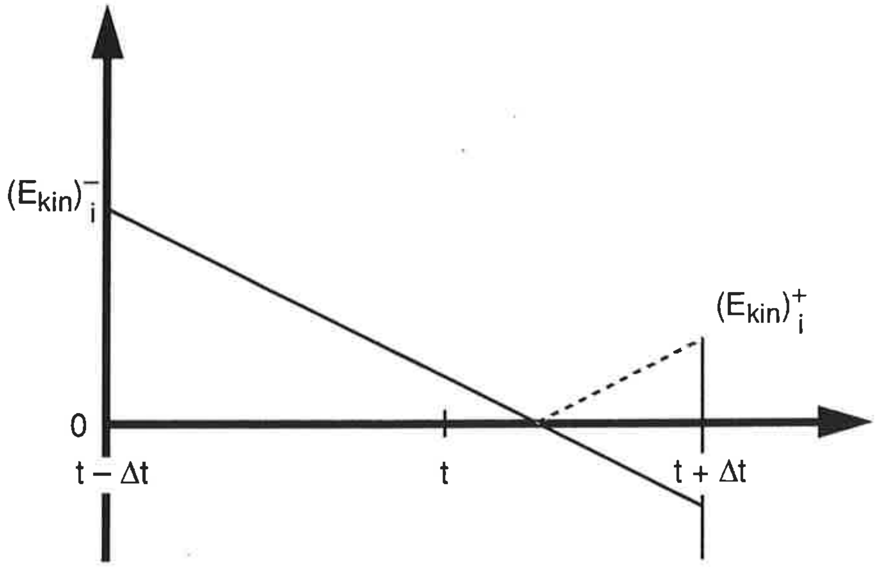

Fig. 2

As indicated in the figure it is suggested simply to change the sign of the predicted kinetic energy at points where it becomes negative. As thereby the total energy is increased by an amount of 2 $(E_{kin})_i^+$ we suggest that the kinetic energy of each of the two neighbouring grid intervals are decreased by an amount of $(E_{kin})_i^+$. (If one or two of the neighbours thereby get negative energy the same procedure is used for these points). At points where the sign of $(E_{kin})_i^+$ has been changed we choose the oppsite sign of that of $(uh)_i^-$ in (18).

By this procedure we preserve conservation of total energy and allow “particles” to change the sign of their velocities within a time step. Normally, with a realistic size of Δt and realistic atmospheric flows it should be few points if any where corrections of kinetic energy are needed.

It should be noted that as total mass and total energy are conserved exactly the above described explicit scheme must be absolutely stable. So for stability reasons at least there should be no need for introducing instead a semi-implicit scheme.

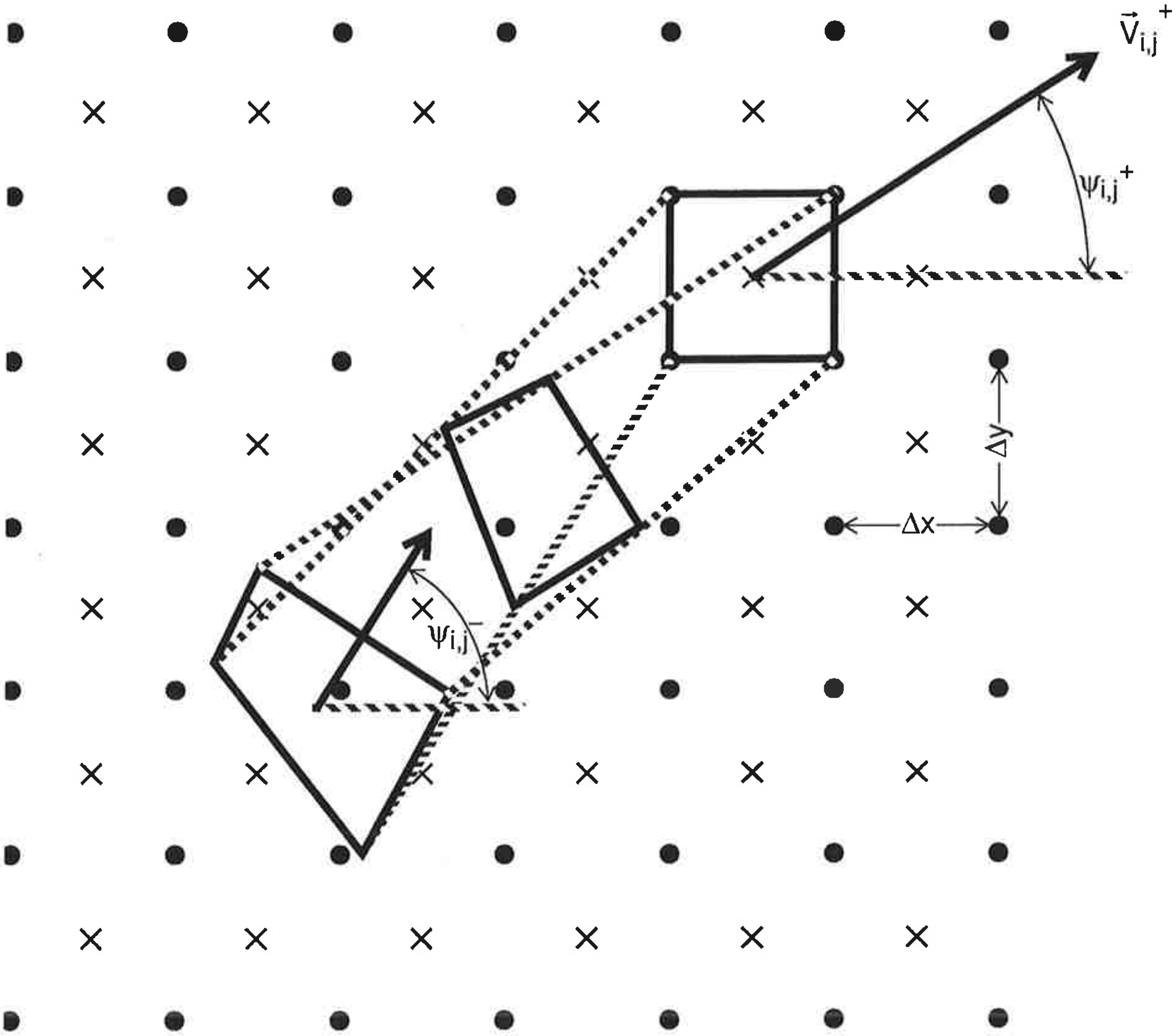

Fig. 3

When extended to 2-D and especially 3-D global models the geometric computations needed to obtain exact conservation may turn out to be too expensive. It is the computation of the "length-weighted" means especially that may become to expensive. Instead of "length-weighted" means one could use values interpolated to the mid points of δx_i^- which would be less complicated to compute in two and three dimensional generalizations. For the present 1-D case this would imply that (14) and (17) become

$$\sum_i h_i^{\ +} \ \Delta x = \sum_i \hat{h}_i^- \ \delta x_i^- \ \sim \sum_i h_i^- \ \Delta x$$

$$\sum_i E_i^{\ +} \ \Delta x = \sum_i \hat{E}_i^- \ \delta x_i^- \ \sim \sum_i E_i^- \ \Delta x \tag{20}$$

where a "hat" indicates an interpolated value. Thus, the conservation of total mass and energy become only approximately valid. The explicit time scheme should however still be absolutely stable as the interpolation will damp the smaller scales more or less.

As in all semi-Lagrangian modes there is of course an upper limit for Δt as all δx_i^- must be positive.

2.2 The 2-D case

For simplicity we assume a regular grid as shown in Figure 3. The grid points are marked by crosses and the corners of the surrounding grid areas are marked by dots. Trajectories are constructed backwards in time from the corners of the grid areas as indicated for one of those in the figure. The end points and mid points of the trajectories have been connected by straight lines. We assume that the two resulting quadrangles contain the air at time $t - \Delta t$ and t, respectively, that is ending up at time $t + \Delta t$ in the square grid area shown.

The forms of the shallow water equations that we shall use are

$$\frac{d}{dt}(h\delta A) = 0 \tag{21}$$

$$\frac{d}{dt}(E\delta A) = -\delta A \nabla \cdot (\frac{1}{2} g h^2 \vec{V}) \tag{22}$$

$$\frac{d}{dt}(\psi V h \delta A) = -h\delta A (fV + g(\frac{\partial h}{\partial n} + \psi \frac{\partial h}{\partial s})) \tag{23}$$

Here δA is the time dependent grid area and $E = 1/2V^2h + 1/2gh^2$ is (except for a factor of density) the total energy per unit area. V is the wind speed ($|\vec{V}|$) and ψ is the direction angle of the wind vector as indicated in Figure 3.

The continuity equation (21) and the energy equation (22) are derived in a similar way as in the 1-D case. The equations (23) is derived from the components of the momentum equation in a natural coordinate system. The shallow water momentum equation is

$$\frac{d\vec{V}}{dt} = -f\vec{k} \times \vec{V} - g\nabla h \tag{24}$$

In natural coordinates the acceleration can be written

$$\frac{d\vec{V}}{dt} = \frac{dV}{dt}\vec{t} + V\frac{d\psi}{dt}\vec{n} \tag{25}$$

where $\vec{t} = \frac{\vec{V}}{V}$ and $\vec{n} = \vec{k} \times \vec{t}$

(See e.g. Haltiner and Martin (1957) sections 11-12 and 11-13)

So by scalar multiplication of (24) by $\vec{n}$ and $\vec{t}$ we obtain, respectively

$$\frac{dV}{dt} = -g\frac{\partial h}{\partial s}$$

and

$$V\frac{d\psi}{dt} = -fV - g\frac{\partial h}{\partial n}$$

where s and n denote curvilinear distances in the $\vec{t}$ and $\vec{n}$ directions, respectively. From these we easily obtain

$$\frac{d}{dt}(\psi V) = -fV - g\left(\frac{\partial h}{\partial n} + \psi\frac{\partial h}{\partial s}\right) \tag{26}$$

which when combined with (21) gives (23).

We choose the following three-time-level discretization of (21)-(23).

$$h^+_{i,j}\;\Delta A = \overline{h^-_{i,j}}\delta A^-_{i,j} \tag{27}$$

$$E^+_{i,j}\;\Delta A = \overline{E}^-_{i,j}\delta A^-_{i,j} - g\Delta t\left[\sum_{k=1}^{4}(h^2\vec{V})_k\cdot\vec{n}_k\delta l_k\right]^0_{i,j} \tag{28}$$

$$\psi^+_{i,j}\;V^+_{i,j}\;h^+_{i,j}\;\Delta A = \overline{(\psi V h)}^-_{i,j}\delta A^-_{i,j} - 2\Delta t\left[h\left(fV + g\left(\frac{\partial h}{\partial n} + \psi\frac{\partial h}{\partial s}\right)\right)\right]^0_{i,j}\delta A^0_{i,j} \tag{29}$$

where $\Delta A = \Delta x\Delta y$, $\delta A^-_{i,j}$ and $\delta A^0_{i,j}$ are the areas at time $t+\Delta t$, $t-\Delta t$ and t, respectively and $\overline{h}^-_{i,j}$, $\overline{E}^-_{i,j}$, $\overline{(\psi V h)}^-_{i,j}$ are "area-weighted" means of the height, the total energy and the momentum weighted wind direction angle at time $t-\Delta t$. In (28) the last term gives the sum of the fluxes of potential energy at the four sides (with length δl_k) of $\delta A^0_{i,j}$. These fluxes should be determined from values interpolated to the mid points of the sides.

When sumed over a periodic domain (27) and (28) give

$$\sum_{i,j} h^+_{i,j}\;\Delta A = \sum_{i,j}\overline{h}^-_{i,j}\delta A^-_{i,j} = \sum_{i,j} h^-_{i,j}\Delta A \tag{30}$$

$$\sum_{i,j} E^+_{i,j}\;\Delta A = \sum_{i,j}\overline{E}^-_{i,j}\delta A^-_{i,j} = \sum_{i,j} E^-_{i,j}\Delta A \tag{31}$$

expressing conservation of total mass and total energy, respectively. If for the sake of computational economy $\overline{h}^-_{i,j}$ and $\overline{E}^-_{i,j}$ are computed as interpolated values then the conservations are only approximately valid. In either case the scheme should be numerically stabel as the interpolations will introduce damping. A logical choise of the point inside $\delta A^-_{i,j}$ to which an interpolation should be made is the "centre of gravity" of $\delta A^-_{i,j}$. In (29) the two terms on the right hand side should be determined as "area-weighted" mean values and as interpolated values at the "centre of gravity" of $\delta A^-_{i,j}$ and $\delta A^0_{i,j}$, respectively.

As in the 1-D case points in which the kinetic energy predicted from equation (28) become negative must be treated separately. A procedure which is analoguous to that described for the 1-D case is suggested. Namely the sign of $(V^+_{i,j})^2$ is changed, $\psi^+_{i,j}$ is changed by adding π and $2\,(V^+_{i,j})^2$ is taken from the neighbouring grid areas in order to maintain total energy conservation.

The order in which the computations in a time step should be made is as follows. At first the continuity equation (27) is used to determine $\overline{h}^+_{i,j}$, then the energy equation (28) is used to determine $V^+_{i,j}$ and finally (29) is used to determine $\psi^+_{i,j}$ from which the wind components can be determined:

$$u_{i,j}^{+} = V_{i,j}^{+} \cos\psi_{i,j}^{+} \tag{32}$$

$$v_{i,j}^{+} = V_{i,j}^{+} \sin\psi_{i,j}^{+} \tag{33}$$

Because the total mass and total energy are either conserved or reduced each time step the scheme can not be numerical unstable in the sense that h and/or V is increasing unlimited. There is , however, no conservation property that puts a limit on changes in ψ. So, from the conservation properties it is not possible in advance to exclude the possibility of unstable oscillations of ψ. From a physical point of view, however, it seems unlikely that such unstable oscillations should develop as oscillations in ψ would imply oscillations in h and/or V which are bounded globally. Experiments will show if (as we expect) the scheme is numerically stable. If it should turn out not to be the case a semi-implicit scheme could be used in the descretization of (23).

In order to justify the use of a semi-Lagrangian time integration scheme as proposed here it must be necessary that the flow remains smooth over the distances of the straight line trajectories used in the scheme. It is expected therefore to be necessary to include a horizontal diffusion which selectively damps the highest resolved wave numbers and thereby prevents a spectral blocking of energy at these wave numbers and furthermore to apply an Asselin time filter in order to damp high frequency oscillations and in particular to prevent a separation of odd and even time steps.

Besides grid point values of the prognostic variables u, v, h also values of $\frac{\partial h}{\partial x}$ and $\frac{\partial h}{\partial y}$ are needed in (29). These derivatives may be computed by finite difference, finite element or spectral techniques. If a spectral technique is chosen then the spectral truncation after each time step will eliminate the energy at the smallest grid resolved scales whereby only a smaller horizontal diffusion of the smallest spectrally resolved scales are needed.

If u, v and h are the variables that are represented spectrally then the conservation of mass (30) will not be affected by the spectral truncation, whereas it will lead to a slight decrease of total energy. The same is the case for linear ∇^{p}-diffusion schemes if applied to these prognostic variables.

3. A full 3-D primitive equation model.

The forms of the primitive equations we shall use are for a generalized vertical coordinate

$$\frac{d}{dt}\left(\frac{\partial p}{\partial \eta}\delta\Omega\right) = 0 \tag{34}$$

$$\frac{d}{dt}\left(q\frac{\partial p}{\partial \eta}\delta\Omega\right) = \frac{\partial p}{\partial \eta}\delta\Omega\,(P_q + K_q) \tag{35}$$

$$\frac{d}{dt}\left(c_p ln\theta\frac{\partial p}{\partial \eta}\delta\Omega\right) = \frac{\partial p}{\partial \eta}\delta\Omega\left[\frac{c_p\,(P_T + K_T)}{T} + h\,(T, p)\,(P_q + K_q)\right] \tag{36}$$

$$\frac{d}{dt}\left(\left(\frac{V^2}{2} + c_p T\right)\frac{\partial p}{\partial \eta}\delta\Omega\right) =$$

$$-\delta\Omega\left[\nabla\cdot\left(\frac{\partial p}{\partial \eta}\phi\vec{V}\right) + \frac{\partial}{\partial \eta}\left(\frac{\partial p}{\partial \eta}\phi\dot{\eta}\right) + \frac{\partial}{\partial \eta}\left(\phi\frac{\partial p}{\partial t}\right) - \frac{\partial p}{\partial \eta}\left(\vec{V}\cdot(\vec{P}_v + \vec{K}_v) + P_{c_pT} + K_{c_pT}\right)\right] \tag{37}$$

$$\frac{d}{dt}\left(\psi_H V\frac{\partial p}{\partial \eta}\delta\Omega\right) = -\frac{\partial p}{\partial \eta}\delta\Omega\left[fV + (\vec{n} + \psi_H\vec{t})\cdot(\nabla\phi + R_d T_v \nabla lnp + \vec{P}_v + \vec{K}_v)\right] \tag{38}$$

The equations are derived in the Appendix.

The notations used are mostly those defined in the ECMWF documentation manual (Research manual 2, M1.6/3).

(34) is the continuity equation, where $\delta\Omega$ is a small volume in the (x, y, η) coordinate system. Thus, $\frac{\partial p}{\partial \eta}\delta\Omega = \delta p\delta A = g\delta M$ where δM is the mass of the volume.

(35) is the moisture equation, where q is the specific humidity. Here and in the following equations P_x and K_x are a parameterized physical tendency and a tendency due to horizontal diffusion of variable X, respectively.

(36) is the thermodynamic equation, where $\theta = T(p/p_0)^{R/c_p}$ is a potential temperature and $c_p ln\theta$ is the specific entrophy. Note that here we have used R and c_p for moist air and not as usual those for dry air.

(37) is the total energy equation and(38) is the prognostic equation for the direction angle ψ_H of the (horizontal) wind vector $\vec{V}$ similar to equation (23) for the 2-D case

To complete the system of equations we need the hydrostatic equation

$$\frac{\partial\phi}{\partial\eta} = -\frac{R_d T_v}{p}\frac{\partial p}{\partial\eta} \tag{39}$$

3.1 The discrete equations

The proposed vertical representation is that used at ECMWF. To represent the vertical variation of the dependent variables $\vec{V}$, θ and q the atmosphere is devided into NLEV layers defined by the pressure at the interfaces (the "half" levels):

$$p_{k+1/2} = a_{k+1/2} + b_{k+1/2}\ p_s \tag{40}$$

where

$$a_{1/2} = b_{1/2} = a_{NLEV+1/2} = 0 \tag{41}$$

$$b_{NLEV+1/2} = 1$$

The prognostic variables are represented by their values at the intermediate levels ("full" levels) with

$$p_k = \frac{1}{2}(p_{k+1/2} + p_{k-1/2}) \tag{42}$$

We define

$$\Delta a_k = a_{k+1/2} - a_{k-1/2} \tag{43}$$

$$\Delta b_k = b_{k+1/2} - b_{k-1/2} \tag{44}$$

and

$$\Delta p_k = p_{k+1/2} - p_{k-1/2} \tag{45}$$

$$= \Delta a_k + \Delta b_k p_s.$$

The discrete analogue of (39) is

$$\phi_{k+1/2} - \phi_{k-1/2} = -R_d (T_v)_k ln (p_{k+1/2}/p_{k-1/2}) \tag{46}$$

which gives

$$\phi_{k+\frac{1}{2}} = \phi_s + \sum_{j=k+1}^{NLEV} R_d (T_v)_j ln (p_{j+1/2}/p_{j-1/2}) \tag{47}$$

Full-level values of geopotential are given by

$$\phi_k = \phi_{k+\frac{1}{2}} + \alpha_k R_d (T_v)_k \tag{48}$$

where

$$\alpha_1 = ln2$$

and

$$\alpha_k = 1 - (p_{k-1/2}/\Delta p_k) \ ln (p_{k+1/2}/p_{k-1/2}) \qquad for \ \ k > 1$$

The proposed discrete version of the continuity equation (34) is

$$\overline{(\delta p)}^{-}_{i,j,k} (\delta A)^{-}_{i,j,k} = (\Delta p)^{+}_{i,j,k} \Delta A^{+}_{i,j} \tag{49}$$

where

$$(\Delta p)^{+}_{i,j,k} = \Delta a_k + \Delta b_k (p_s)^{+}_{i,j} \tag{50}$$

we assume that a volume which at time $t + \Delta t$ ends up as a grid volume at level k has been advected with vertical walls in the horizontal wind field $\vec{V}_k (t)$. $(\delta A)^{-}_{i,j,k}$ is the area defined by the end points of the trajectories computed $2\Delta t$ backward in time from the four corners of the grid area $(\Delta A)^{+}_{i,j}$. $\overline{(\delta p)}^{-}_{i,j,k}$ is the area mean pressure difference between the top and bottom of the volume:

$$\overline{(\delta p)}^{-}_{i,j,k} = (p_B)^{-}_{i,j,k} - (p_T)^{-}_{i,j,k} = (p_B)^{-}_{i,j,k} - \frac{1}{(\delta A)^{-}_{i,j,k}} \sum_{n=1}^{N_{i,j,k}} AT_n (p_B)_{n,k-1} \tag{51}$$

Here $(p_B)^{-}_{i,j,k}$ is the pressure at the bottom which is assumed constant over the area except for the lowest layer $k = NLEV$. The last term in (51) is an area mean pressure at the top.Here

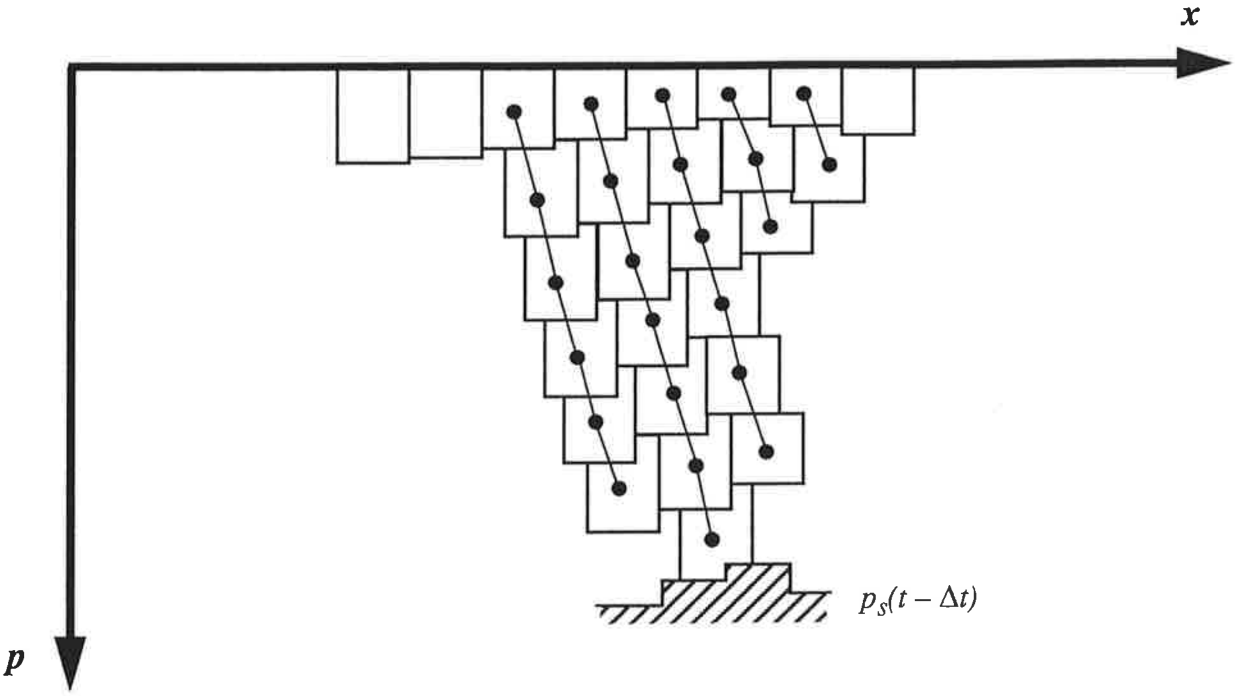

Fig. 4a

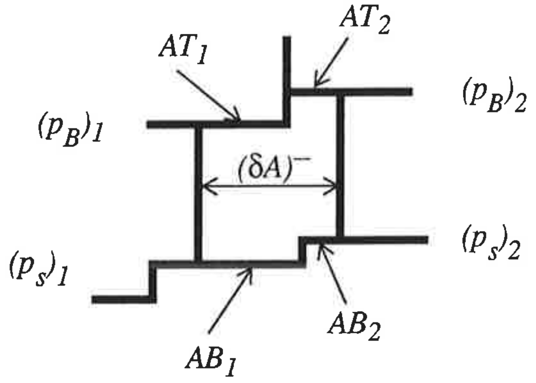

$$p_T = \frac{1}{(\delta A)^-}\left(AT_1\,(p_B)_1 + AT_2\,(p_B)_2\right)$$

$$p_B = \frac{1}{(\delta A^-)}\left(AB_1\,(p_s)_1 + AB_2\,(p_s)_2\right)$$

Fig. 4b

$N_{i,j,k}$ is the number of volumes at level $k-1$ which overlap $(\delta A)^-_{i,j,k}$. For the top layer $k = 1$ this term is zero. For the lowest layer $k = NLEV$ $(p_B)^-_{i,j,k}$ is

$$(p_B)^-_{i,j,NLEV} = \frac{1}{(\delta A)^-_{i,j,NLEV}} \sum_{n=1}^{M_{i,j,k}} AB_n (p_s(t-\Delta t))_n \tag{52}$$

where $M_{i,j,k}$ is the number of grid squeres that $(\delta A)_{i,j,NLEV}$ overlap.

As an illustration consider the simple case of an advection where $\vec{V}_k(t)$ has the same direction at all levels. For such a case Figure 4a shows some departure volumes in a (x,p)-coordiante system. Those volumes that at time $t+\Delta t$ end up as a vertical column and which therefore have the same $p_s{}^+$ in (50) are conected by thin lines. Consider the single bottom volume which is "blown up" in Figure 4b. In this case N and M are both 2 and the two areas and two pressures used to define the top and bottom pressure, respectively, are indicated in the figure.

By inserting (50) and (51) in (49) we get the following expression for the bottom pressure of a certain volume

$$(p_B)^-_{i,j,k} = \frac{1}{(\delta A)^-_{i,j,k}} \left[\sum_{n=1}^{N_{i,j,k}} AT_n (p_B)_{n,k-1} + (\Delta A)^+_{i,j} \ (\Delta a_k + \Delta b_k (p_s)^+_{i,j}) \right] \tag{53}$$

At the upper most level $k = 1$, which is always an isobaric layer, the first and last term are zero. More of the upper layers may be isobaric layers in which case the last term is zero also for these layers.

For the hybrid - and sigma-layers (for which $\Delta b_k \neq 0$), however, $(p_s)^+_{i,j}$ is included in the expression for $(p_B)^-_{i,j,k}$. Thus, we have to determine $(p_s)^+_{i,j}$ before all the bottom pressures of the volumes can be determined. A system of equations from which $(p_s)^+_{i,j}$ can be determined are obtained by setting (53) for $k = NLEV$ equal to (52):

$$\sum_{n=1}^{N_{i,j,NLEV}} AT_n (p_B)_{n,NLEV-1} + (\Delta A)^+_{i,j} \ \Delta b_{NLEV} (p_s)^+_{i,j} = \tag{54}$$

$$\sum_{n=1}^{M_{i,j}} AB_n (p_s(t-\Delta t))_n - (\Delta A)^+_{i,j} \ \Delta a_{NLEV}$$

When the $(p_B)_{i,j,NLEV-1}$ that appear in the first term (and are given by (53)) are inserted in

(54) and the $(p_B)_{i,j,NLEV-2}$ that appear in the resulting equation are inserted - and so on- we arrive at a linear equation for each gridpoint i, j of the form

$$\sum_{n=1}^{L_{i,j}} C_{i,j,n} (p_s)_n^{\ +} \ = d_{i,j} \tag{55}$$

A number of surface pressure values $(p_s(t+\Delta t))_{i,j}$ from a group of neighbour grid points appear on the left hand side of each of the equations (55). In the case considered in Figure 4a we get $p_s(t+\Delta t)$ values from four neighbour grid points. The coefficients $C_{i,j,n}$ and the right hand sides $d_{i,j}$ in (55) can be determined from known quantities.

When the surface pressure field $(p_s(t+\Delta t))_{i,j}$ has been determined from (55) we can finally determine $(p_B)^-_{i,j,k}$ from (53) for all the volumes with $k < NLEV$ whereuppon the volumes $(\delta p)^-_{i,j,k} (\delta A)^-_{i,j,k}$ are completely determined.

When (49) is summed over all grid points for a periodic domain we get

$$\sum_{i,j} (p_s(t+\Delta t))_{i,j} \Delta A_{i,j} = \sum_{i,j} (p_s(t-\Delta t))_{i,j} \Delta A_{i,j} \tag{56}$$

i.e. exact conversation of mass.

In the energy equation we will need $\frac{\partial p}{\partial \eta} \dot{\eta}$ at the bottom surface of each of the volumes at time t. $\frac{\partial p}{\partial \eta} \dot{\eta}$ is the mass flux (except for a factor g) through an η surface. We shall compute this quantity, which we shall call W_η, in a way that is consistent with the Lagrangian discretization of the continuity equation proposed above. From (49) we get

$$(\Delta p)_k^{\ +} - (\delta p)_k^- = (\Delta p)_k^{\ +} - \frac{(\Delta A)^{\ +}}{(\delta A)_k^-} (\Delta p)_k^{\ +}$$

$$= (\Delta p)_k^{\ +} \left(1 - \frac{(\Delta A)^{\ +}}{(\delta A)_k^-}\right)$$

or

$$\frac{p^+_{k+1/2} - p^-_B}{2\Delta t} - \frac{p^+_{k-1/2} - p^-_T}{2\Delta t} = \frac{(\Delta p)_k^{\ +}}{2\Delta t} \left(1 - \frac{(\Delta A)^{\ +}}{(\delta A)_k^-}\right)$$

or

$$\{(W_\eta)_B\}_k^0 = \{(W_\eta)_T\}_k^0 + \frac{(\Delta p)_k^{+}}{2\Delta t}\left(1 - \frac{(\Delta A)^{+}}{(\delta A)_k^{-}}\right) \tag{57}$$

For convenience we have omited the indicies i and j. When the continuity equation has been solved as described above the second right hand term in (57) is known and the first term can be determined as an area wighted sum of those bottom fluxes in the layer above that $(\delta A)_k^o$ overlap.

The vertical flux of geopotential needed in the discrete version of (37) is then computed as

$$\left(\frac{\partial p}{\partial \eta}\dot{\eta}\phi\right)_{B,k}^{0} = \{(W_\eta)_B\}_k^0 \{(\phi(t))_B\}_k$$

where the last factor is the geopotential interpolated to the mid point of the bottom surface of the advected grid volume at time t. The position of this surface is determined by the mid points of the trajectories and the pressure

$$(p_B)_k^0 = \frac{1}{2}(p_{k+1/2}^{+} + (p_B^{-})_k) \tag{58}$$

For the bottom layer we use $\left(\frac{\partial p}{\partial \eta}\dot{\eta}\phi\right)_{B,NLEV} = 0$.

We shall not in this Note list the discrete equations corresponding to the contious equations (35) - (38). They are to a great extend analoguous to those given previously for the 1-D and 2-D shallow water equations. We shall just make some general comments.

For all the equations we propose the leap frog scheme to be used and to evaluate the right hand sides of the equations for the advected grid volumes at time t. Exceptions are the physical parameterization terms (the P-terms) for which as usual generally a forward time scheme should be used, the horizontal diffusion terms (the K-terms) for which either a forward or preferably a backward scheme should be used and finally the term $\delta\Omega\frac{\partial}{\partial\eta}\left(\phi\frac{\partial p}{\partial t}\right)$ in the energy equation to which we shall return presently.

The advected grid volumes at time t were defined above. A certain volume is supposed to have vertical plane walls going through the mid points of the trajectories from the corners of the grid square in question and to have a bottom pressure given by (58). At the top it is bounded by the bottom pressure surfaces of the volumes it overlaps (as indicated in Figure 4a, though at time $t-\Delta t$). The horizontal fluxes in (37) must be evaluated by interpolation to the mid points of the vertical walls and the Coriolis and pressure gradiant terms in (38) should be interpolated to the centre of gravity of the volume. The discrete equations furthermore involve an evaluation of the prognostic quantities $c_p ln\theta\delta p\delta A$, $(\frac{1}{2}V^2 + c_p T)\,\delta p\delta A$ and $\psi_H V\delta p\delta A$ in the departure volumes at time $t - \Delta t$. Preferably volume weighted mean values should be used which (together with a consistent determination of the fluxes on the right hand sides of the equations) will ensure that the conservation properties are retained.

Also the term

$$\delta\Omega\frac{\partial}{\partial\eta}(\phi\frac{\partial p}{\partial t})$$

on the right hand side of (37) must be treated in a special way in order to maintain energy conservation. The following discretization of this term is suggested:

$$\begin{aligned}&\frac{\Delta A_{i,j}}{2\Delta t}\,[\phi_{k+1/2}(t)\,(p_{k+1/2}(t+\Delta t) - p_{k+1/2}(t-\Delta t))\\ &-\phi_{k-1/2}(t)\,(p_{k-1/2}(t+\Delta t) - p_{k-1/2}(t-\Delta t))\,]_{i,j}\end{aligned} \tag{59}$$

The sum over all grid volumes of this expression gives

$$\sum_{i,j}(\phi_s)_{i,j}(p_s(t+\Delta t))_{i,j}\Delta A_{i,j} - \sum_{i,j}(\phi_s)_{i,j}((p_s(t-\Delta t))_{i,j}\Delta A_{i,j})$$

So that when diabatic and dissipation terms are neclected the sum over all grid points of the full energy equation gives

$$E_{tot}(t+\Delta t) = E_{tot}(t-\Delta t)$$

where

$$E_{tot} = \sum_{i,j,k}\{(\frac{1}{2}V^2 + c_p T)\,\Delta p\}_{i,j,k}\,\Delta A_{i,j} + \sum_{i,j}\{\phi_s p_s \Delta A\}_{i,j}$$

is a proper definition of the “discrete” total energy.

The sequence of computations in a time step should be as follows:

At first horizontal trajectory computations then determination of $(p_s(t+\Delta t))$ from(55), determination of $(p_B)^-$ using (53) and $(W_\eta)_B^0$ using (57). Then using the discrete version of (34) to determine $q(t+\Delta t)$, (36) and the definition of θ to determine $T(t+\Delta t)$, (47) and (48) to determine $\phi_{k+1/2}(t+\Delta t)$ and $\phi_k(t+\Delta t)$, (37) to determine $V(t+\Delta t)$ and finally (38) to determine $\psi_H(t+\Delta t)$ from which the wind components can be computed as in (32).

Concerning numerical stability of the proposed leap frog scheme, the possibility of using a spectral representation and the use of a numerical time filter and a horizontal diffusion the remarks made at the end of the last section (after equations (32)) apply also for the 3-D case considered in the present section.

4. Concluding remarks

In the scheme presented in the preceding sections an exact conservation of mass, total energy and entrophy were obtained when the mean values over the areas $\delta A^{-}_{i,j}$ were computed as "area-weighted" mean values. In these computations the prognostic values (i.e. δp, $q\delta p$, $(V^2/2 + C_pT)\ \delta p$, $C_p ln\theta\delta p$, $\psi_H V\delta p$) at time $t - \Delta t$ were assumed constant within each grid area. This constant finite element representation is the simplest possible distribution of the variables within a grid area. When applied to pure horizontal advection in a constant wind field it is obvious that this constant finite element representation will imply a damping of the smallest scales and especially a smearing of steep gradients. As mentioned in section 2 some smoothing of the smallest resolved scales is desireable, but the numerical damping may be too severe and furthermore it is a disadvantage that it can not be controled explicitely. It may therefore be considered if a higher order finite element representation should be used.

In a recent paper, Rancic (1992) (which the author became aware of just after completion of the preceding sections of this note), a new semi-Lagrangian scheme for two-dimensional horizontal advection of a passive scalar were presented. This scheme turns out to be similar in several respects to the more general scheme presented in this note, except that a biparabolic finite element representation is used. A similar representation, or one based on linear finite elements, might be used also in the present scheme, in some or in all the prognostic equations. This would reduce the small scale damping, but of course at the expense of increased computational time.

Acknowledgements. The author would like to express his gratitude to Dr. Adrian Simmons for suggesting the use of trajectories from the corner points of grid areas, to Dr. Klaus Arpe and Prof. Lennart Bengtsson for stimulating discussions and to Claudia Schröder and Norbert Noreiks for expert typing and drawing work.
The author would like to thank also Drs. Harol Ritchie and David Williamson for comments on the original draft.

Appendix

Derivation of the continuous equations

As a starting point we take the continuous equations for a general pressure -based terrain- following vertical coordinate $\eta\,(p, p_s)$ as formulated for the ECMWF model (equations (1.2.2)-(1.2.5) in the Research Manual 2, M1.6/3) which may be written as

$$\frac{d\vec{V}}{dt} = -\nabla\phi - \alpha\nabla p - f\vec{k}\times\vec{V} + \vec{P}_v + \vec{K}_v \tag{A1}$$

$$c_p\frac{dT}{dt} = \alpha\omega + (P_T + K_T)\,c_p \tag{A2}$$

$$\frac{dq}{dt} = P_q + K_q \tag{A3}$$

$$\frac{d}{dt}\left(ln\frac{\partial p}{\partial\eta}\right) + \nabla\cdot\vec{V} + \frac{\partial\dot{\eta}}{\partial\eta} = 0 \tag{A4}$$

where $\vec{V}$ is the horizontal wind vector and

$$\begin{gathered} \alpha = \frac{R_d T_v}{p};\ T_v = T\left[1 + \left(\frac{1}{\varepsilon} - 1\right)q\right];\ \varepsilon = R_d/R_v \\ c_p = c_{pd}\left[1 + (\delta - 1)\,q\right];\ \delta = c_{pv}/c_{pd} \end{gathered} \tag{A5}$$

With a few exceptions we use the notations introduced in the ECMWF manual. Following this manual the P-terms are:

$$\vec{P}_v = -g\left(\frac{\partial p}{\partial\eta}\right)^{-1}\left(\frac{\partial}{\partial\eta}\right)\vec{J}_v \tag{A6}$$

$$c_p P_T = Q_R + Q_L + Q_D - g\left(\frac{\partial p}{\partial\eta}\right)^{-1}\left[\frac{\partial}{\partial\eta}J_s - c_{pd}T\,(\delta - 1)\,\frac{\partial}{\partial\eta}J_q\right] \tag{A7}$$

$$P_q = S_q - g\left(\frac{\partial p}{\partial\eta}\right)^{-1}\frac{\partial}{\partial\eta}J_q \tag{A8}$$

In (A1)-(A3) $\vec{J}_v$, J_s and J_q represent net parmeterized vertical fluxes of momentum, dry static energy $c_pT + \phi$, and moisture. Q_R, Q_L and Q_P represents heatings due respectively to radiation, to internal phase changes and to the internal dissipation of kinetic energy associated with the $\vec{P}_v$ term. S_q denotes the rate of change of q due to rainfall and snowfall. The terms $\vec{K}_v$, K_T and K_q in (A1)-(A3) represents the horizontal diffusion.

1.The continuity equation

Using that

$$\nabla \cdot \vec{V} + \frac{\partial \dot{\eta}}{\partial \eta} = \frac{1}{\delta\Omega} \frac{d\delta\Omega}{dt} \qquad \text{(A9)}$$

where $\delta\Omega$ is an infinitesimal small volume in the (x, y, η) space (A4) becomes

$$\delta\Omega \frac{d}{dt}\left(\frac{\partial p}{\partial \eta}\right) + \frac{\partial p}{\partial \eta} \frac{d\delta\Omega}{dt} = 0$$

or

$$\frac{d}{dt}\left(\frac{\partial p}{\partial \eta} \delta\Omega\right) = 0 \qquad \text{(A10)}$$

2. The moisture equation

Using (A10) and (A3) we get

$$q \frac{d}{dt}\left(\frac{\partial p}{\partial \eta} \delta\Omega\right) + \left(\frac{\partial p}{\partial \eta} \delta\Omega\right) \frac{dq}{dt} = \left(\frac{\partial p}{\partial \eta} \delta\Omega\right) (P_q + K_q)$$

or

$$\frac{d}{dt}\left(q \frac{\partial p}{\partial \eta} \delta\Omega\right) = \left(\frac{\partial p}{\partial \eta} \delta\Omega\right) (P_q + K_q) \qquad \text{(A11)}$$

3. The total energy equation

Scalar multiplication of (A1) with $\vec{V}$ gives

$$\frac{d}{dt}\left(\frac{V^2}{2}\right) = -\vec{V} \cdot \nabla\phi - \alpha\vec{V} \cdot \nabla p + \vec{V} \cdot (\vec{P}_v + \vec{K}_{\vec{v}}) \qquad \text{(A12)}$$

Multiplication of (A12) with $\frac{\partial p}{\partial \eta} \delta\Omega$ and (A10) with $V^2/2$ and addition of the resulting equations gives

$$\frac{d}{dt}\left(\frac{V^2}{2} \frac{\partial p}{\partial \eta} \delta\Omega\right) = -\frac{\partial p}{\partial \eta} \delta\Omega \left[\vec{V} \cdot \nabla\phi + \alpha\vec{V} \cdot \nabla p - \vec{V} \cdot (\vec{P}_v + \vec{K}_v)\right] \qquad \text{(A13)}$$

The first two terms in the square brackets multiplied by $\frac{\partial p}{\partial \eta}$ may be transformed as follows

$$\begin{aligned}
&\frac{\partial p}{\partial \eta}\vec{V}\cdot\nabla\phi+\alpha\frac{\partial p}{\partial \eta}\vec{V}\cdot\nabla p = \\
&\nabla\cdot\left(\frac{\partial p}{\partial \eta}\phi\vec{V}\right)-\phi\nabla\cdot\left(\frac{\partial p}{\partial \eta}\vec{V}\right)+\alpha\frac{\partial p}{\partial \eta}\vec{V}\cdot\nabla p = \\
&\nabla\cdot\left(\frac{\partial p}{\partial \eta}\phi\vec{V}\right)+\phi\left(\frac{\partial}{\partial t}\left(\frac{\partial p}{\partial \eta}\right)+\frac{\partial}{\partial \eta}\left(\frac{\partial p}{\partial \eta}\dot{\eta}\right)\right)+\alpha\frac{\partial p}{\partial \eta}(\vec{V}\cdot\nabla p) \\
&\nabla\cdot\left(\frac{\partial p}{\partial \eta}\phi\vec{V}\right)+\phi\frac{\partial}{\partial t}\left(\frac{\partial p}{\partial \eta}\right)+\frac{\partial}{\partial \eta}\left(\frac{\partial p}{\partial \eta}\phi\dot{\eta}\right)-\frac{\partial p}{\partial \eta}\dot{\eta}\frac{\partial \phi}{\partial \eta}+\alpha\frac{\partial p}{\partial \eta}\vec{V}\cdot\nabla p = \\
&\nabla\cdot\left(\frac{\partial p}{\partial \eta}\phi\vec{V}\right)+\frac{\partial}{\partial \eta}\left(\frac{\partial p}{\partial \eta}\phi\dot{\eta}\right)+\left(\phi\frac{\partial}{\partial \eta}\frac{\partial p}{\partial t}+\frac{\partial \phi}{\partial \eta}\frac{\partial p}{\partial t}\right)+\frac{\partial p}{\partial \eta}\alpha\left(\frac{\partial p}{\partial t}+\vec{V}\cdot\nabla p+\dot{\eta}\frac{\partial p}{\partial \eta}\right) = \\
&\qquad\nabla\cdot\left(\frac{\partial p}{\partial \eta}\phi\vec{V}\right)+\frac{\partial}{\partial \eta}\left(\frac{\partial p}{\partial \eta}\phi\dot{\eta}\right)+\frac{\partial}{\partial \eta}\left(\phi\frac{\partial p}{\partial t}\right)+\frac{\partial p}{\partial \eta}\alpha\omega
\end{aligned}\tag{A14}$$

where the hydrostatic equation

$$\frac{\partial \phi}{\partial \eta} = -\alpha\frac{\partial p}{\partial \eta}$$

and the continuity equation on the form

$$\nabla\cdot\left(\frac{\partial p}{\partial \eta}\vec{V}\right) = -\left(\frac{\partial}{\partial t}\left(\frac{\partial p}{\partial \eta}\right)+\frac{\partial}{\partial \eta}\left(\frac{\partial p}{\partial \eta}\dot{\eta}\right)\right)$$

were used.

Substituting the final expression (A14) into (A13) this equation become

$$\begin{aligned}
&\frac{d}{dt}\left(\frac{V^2}{2}\frac{\partial p}{\partial \eta}\delta\Omega\right) = \\
&-\delta\Omega\left[\nabla\cdot\left(\frac{\partial p}{\partial \eta}\phi\vec{V}\right)+\frac{\partial}{\partial \eta}\left(\frac{\partial p}{\partial \eta}\phi\dot{\eta}\right)+\frac{\partial}{\partial \eta}\left(\phi\frac{\partial p}{\partial t}\right)+\frac{\partial p}{\partial \eta}\alpha\omega-\left(\vec{V}\cdot\frac{\partial p}{\partial \eta}\right)(\vec{P}_v+\vec{K}_v)\right]
\end{aligned}\tag{A15}$$

We then derive the total potential energy equation. We have

$$\frac{d}{dt}(c_pT) = c_p\frac{dT}{dt}+T\frac{dc_p}{dt} = c_p\frac{dT}{dt}+c_{pd}T(\delta-1)\frac{dq}{dt}$$

Using (A2), (A3), (A7) and (A8) we get from this

$$\frac{d}{dt}(c_pT) = \alpha\omega+P_{c_pT}+K_{c_pT}\tag{A16}$$

where

$$P_{c_pT} = Q_R + Q_L + Q_D + c_{pd}T(\delta - 1)S_q - g\left(\frac{\partial p}{\partial \eta}\right)^{-1}\frac{\partial}{\partial \eta}J_s$$

and

$$K_{c_pT} = c_pK_T + c_{pd}T(\delta - 1)K_q$$

Multiplication of (A16) with $\frac{\partial p}{\partial \eta}\delta\Omega$ and (A10) with c_pT and addition of the resulting equations gives:

$$\frac{d}{dt}\left(c_pT\frac{\partial p}{\partial \eta}\delta\Omega\right) = \frac{\partial p}{\partial \eta}\delta\Omega\left(\alpha\omega + P_{c_pT} + K_{c_pT}\right) \tag{A17}$$

We now add this equation to (A15) and become finally

$$\frac{d}{dt}\left(\left(\frac{V^2}{2} + c_pT\right)\frac{\partial p}{\partial \eta}\delta\Omega\right) = \tag{A18}$$

$$-\delta\Omega\left[\nabla\cdot\left(\frac{\partial p}{\partial \eta}\phi\vec{V}\right) + \frac{\partial}{\partial \eta}\left(\frac{\partial p}{\partial \eta}\phi\dot{\eta}\right) + \frac{\partial}{\partial \eta}\phi\left(\frac{\partial p}{\partial t}\right) - \frac{\partial p}{\partial \eta}\left(\vec{V}\cdot\left(\vec{P}_v + \vec{K}_v\right) + P_{c_pT} + K_{c_pT}\right)\right]$$

4. The thermodynamic equation

We define the potential temperature θ as

$$\theta = T\left(\frac{p_0}{p}\right)^{R/c_p} \qquad p_0 = 1000\ hPa \tag{A19}$$

where

$$R = (1-q)R_d + qR_v$$

$$c_p = (1-q)c_{pd} + qc_{pv}$$

Logarithmic differentiation of (A19) gives

$$\frac{d}{dt}(c_p ln\theta) = \frac{1}{T}\left(c_p\frac{dT}{dt} - \alpha\omega\right) + h(T,p)\left(\frac{dq}{dt}\right) \tag{A20}$$

where

$$h(T,p) = (c_{pv} - c_{pd})\,lnT + (R_v - R_d)\,ln(p_0/p)\,.$$

Using (A2) and (A3) in (A20) we get

$$\frac{d}{dt}(c_p ln\theta) = \frac{c_p (P_T + K_T)}{T} + h(T,p)\,(P_q + K_q) \tag{A21}$$

Multiplication of (A21) with $\frac{\partial p}{\partial \eta}\delta\Omega$ and (A10) with $c_p ln\theta$ and addition of the resulting equations gives:

$$\frac{d}{dt}\left(c_p ln\theta \frac{\partial p}{\partial \eta}\delta\Omega\right) = \delta\Omega\frac{\partial p}{\partial \eta}\left[\frac{c_p (P_T + K_T)}{T} + h(T,p)\,(P_q + K_q)\right] \tag{A22}$$

5. The wind direction equation

This equation is derived from the momentum equation in natural coordinates (see e.g. Haltiner and Martin (1957), Section 11-13).

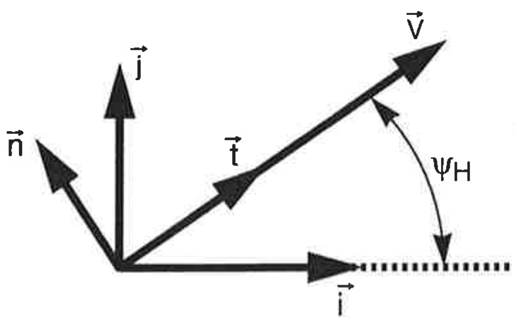

Fig. 5

The accelleration of the horizontal wind $\vec{V}$ with the approximations traditionally made in the primitive equations may be represented in a natural coordinate system as

$$\frac{d\vec{V}}{dt} = \frac{dV}{dt}\vec{t} + V\frac{d\psi_H}{dt}\vec{n} \tag{A23}$$

where $\vec{t} = \frac{\vec{V}}{V}$, $\vec{n} = \vec{k}\times\vec{t}$, $V = |\vec{V}|$ and ψ_H is *a* wind direction angle in the instantaneus tangent plane as illustrated in the figure shown above.

It follows from (A23) that

$$\frac{d}{dt}(\psi_H V) = \psi_H\frac{dV}{dt} + V\left(\frac{d\psi_H}{dt}\right)$$

$$= (\vec{n} + \psi_H \vec{t}) \cdot \frac{d\vec{V}}{dt} \tag{A24}$$

Multiplication of with $\frac{\partial p}{\partial \eta} \delta\Omega$ and (A10) with $\psi_H V$ and addition of the resulting equations give

$$\frac{d}{dt}\left(\psi_H V \frac{\partial p}{\partial \eta} \delta\Omega\right) = \frac{\partial p}{\partial \eta} \delta\Omega \, (\vec{n} + \psi_H \vec{t}) \cdot \frac{d\vec{V}}{dt}$$

which gives (38) when $d\vec{V}/dt$ is substituted from (A1).

References

Haltiner, G.J. and F.L.Martin, 1957:
Dynamical and Physical Meteorology.
McGRAW-HILL BOOK COMPANY, 470 pp.

Rancic, Miodrag, 1992:
Semi-Lagrangian Piecewise Biparabolic Scheme for
Two-Dimensional Horizontal Advection of a Passive Scalar.
Mon.Wea.Rev., 120, 1394-1406